

PREDEFINED DAMAGE PATTERNS FOR LIMIT ANALYSIS ON NON-
ENGINEERED MASONRY BUILDINGS

A THESIS SUBMITTED TO
THE GRADUATE SCHOOL OF NATURAL AND APPLIED SCIENCES
OF
MIDDLE EAST TECHNICAL UNIVERSITY

BY

CEMAL İÇEL

IN PARTIAL FULFILLMENT OF THE REQUIREMENTS
FOR
THE DEGREE OF MASTER OF SCIENCE
IN
CIVIL ENGINEERING

SEPTEMBER 2019

Approval of the thesis:

PREDEFINED DAMAGE PATTERNS FOR LIMIT ANALYSIS ON NON-ENGINEERED MASONRY BUILDINGS

submitted by **CEMAL İÇEL** in partial fulfillment of the requirements for the degree of **Master of Science in Civil Engineering Department, Middle East Technical University** by,

Prof. Dr. Halil Kalıpçılar
Dean, Graduate School of **Natural and Applied Sciences**

Prof. Dr. Ahmet Türer
Head of Department, **Civil Engineering**

Prof. Dr. Murat Altuğ Erberik
Supervisor, **Civil Engineering, METU**

Examining Committee Members:

Assoc. Prof. Dr. Mustafa Tolga Yılmaz
Engineering Science, METU

Prof. Dr. Murat Altuğ Erberik
Civil Engineering, METU

Assoc. Prof. Dr. Ozan Cem Çelik
Civil Engineering, METU

Assist. Prof. Dr. Bekir Özer Ay
Architecture, METU

Assoc. Prof. Dr. Alper Aldemir
Civil Engineering, Hacettepe University

Date: 03.09.2019

I hereby declare that all information in this document has been obtained and presented in accordance with academic rules and ethical conduct. I also declare that, as required by these rules and conduct, I have fully cited and referenced all material and results that are not original to this work.

Name, Surname: Cemal İel

Signature:

ABSTRACT

PREDEFINED DAMAGE PATTERNS FOR LIMIT ANALYSIS ON NON-ENGINEERED MASONRY BUILDINGS

İçel, Cemal
Master of Science, Civil Engineering
Supervisor: Prof. Dr. Murat Altuğ Erberik

September 2019, 178 pages

Non-engineered masonry construction still constitutes a significant percentage of building stocks, especially in earthquake-prone Mediterranean, Asian and South American countries. It is not easy to quantify the seismic performance of this building type, because the analytical and numerical methods, which have been developed so far, generally work for engineered masonry buildings with specific design and construction practices. For such buildings, it is easy to define the load transfer paths through well-defined structural members. However, non-engineered masonry buildings generally do not have well-quantified material properties, rigid floor diaphragms and adequate floor-to-wall or wall-to-wall connections in order to ensure such a load path. Hence the use of conventional analysis tools become meaningless or even misleading since the seismic behavior of non-engineered buildings contradicts with the fundamentals of structural analysis and modeling, on which these analysis tools are based on. In such cases, the use of simple theoretical analyses, which are generally based on observed performance and damage on the considered building type, may provide a practical solution. This study aims to propose prescribed in-plane damage mechanisms and crack patterns for solid and perforated masonry walls by using the available post-earthquake field data obtained from damaged masonry buildings and experimental data obtained from masonry specimens. These predefined

damage and crack patterns can be used as an input for lower-bound limit analysis solutions in order to estimate the lateral load capacity of non-engineered masonry buildings.

Keywords: Non-engineered Masonry, Limit Analysis, In-plane Wall Damage, Crack Pattern, Failure Mode

ÖZ

MÜHENDİSLİK HİZMETİ GÖRMEMİŞ YIĞMA BİNALAR ÜZERİNDE LİMİT ANALİZİ İÇİN ÖNCEDEN TANIMLANAN HASAR MODELLERİ

İçel, Cemal
Yüksek Lisans, İnşaat Mühendisliği
Tez Danışmanı: Prof. Dr. Murat Altuğ Erberik

Eylül 2019, 178 sayfa

Mühendislik hizmeti görmemiş donatısız yığma binalar, özellikle deprem tehlikesinin yüksek olduğu Akdeniz, Asya ve Güney Amerika ülkelerinde hala yapı stokunun önemli bir yüzdesini oluşturmaktadır. Bu bina tipinin sismik performansını ölçmek kolay değildir, çünkü şu ana kadar geliştirilen analitik ve sayısal yöntemler, genellikle belirli tasarım ve inşaat uygulamalarına sahip mühendislik hizmeti görmüş yapılar için geçerlidir. Bu tür binalar için, yük transfer yollarını iyi tanımlanmış yapısal elemanlar vasıtasıyla tanımlamak kolaydır. Bununla birlikte, donatısız yığma yapıları genellikle böyle bir yük yolunu sağlamak için iyi ölçülmüş malzeme özelliklerine, rijit döşeme diyaframlarına ve yeterli döşeme-duvar veya duvar-duvar bağlantılarına sahip değildir. Bu nedenle, geleneksel analiz araçlarının kullanımı, donatısız yığma binaların sismik davranışları, bu analiz araçlarının dayandığı yapısal analiz ve modellemenin temelleriyle çelişkili olduğundan, anlamsız ve hatta yanıltıcı hale gelir. Bu gibi durumlarda, çoğunlukla gözlemlenen performansa ve düşünülen bina tipindeki hasara dayanan basit teorik analizlerin kullanılması pratik bir çözüm sağlayabilir. Bu çalışma, hasarlı duvar binalarından elde edilen mevcut deprem sonrası verilerini ve duvar örneklerinden elde edilen deneysel verileri kullanarak dolu ve delikli duvar duvarları için öngörülen düzlem içi hasar mekanizmalarını ve çatlak modellerini geliştirmeyi amaçlamaktadır. Bu önceden tanımlanmış hasar ve çatlak

dağılımları, mühendislik hizmeti görmemiş yığma yapıların yanal yük kapasitesini tahmin etmek için alt-sınır limit analiz çözümlmelerine veri olarak kullanılabilir.

Anahtar Kelimeler: Donatısız Yığma Binalar, Limit Analiz, Düzlem İçi Duvar Hasarları, Çatlak Dağılımları, Göçme Türü

To my dearest wife Sade.

ACKNOWLEDGEMENTS

First and foremost, I would like to express my gratitude to Prof. Dr. Murat Altuğ Erberik. He always helped me throughout this dissertation and encouraged me for doing my best in the study. Without his support and guidance, this thesis would not have been possible.

I owe thanks to Assoc. Prof. Dr. Mustafa Tolga Yılmaz for helping me during the analysis steps of my study and sharing his valuable comments and suggestions. His comments and recommendations enhanced the level of this study.

I would like to thank to my colleague Derya Karadeniz for joining the discussion sessions and explaining her work which is like a follow-up study of mine.

I am deeply grateful to my family for always supporting me morally in this tough journey. Knowing that they are always by my side even when everything goes bad, eases and comforts my mind in this process. My father Mehmet Levent İnel, my mother Nazmiye İnel and my brother Ertuğrul İnel, I am grateful for you are my family.

I have completed this study while I have been working in a full-time project office. This study could not have been finalized unless my managers in PROMER Consultancy Engineering, namely, Hasan Başaran, Yüksel Tonguç and Altuğ Bayram supported me.

I want to thank my friends and colleagues for supporting and motivating me. Thank you very much Ceren Usalan, Yusuf Ziya Öztürk, Cemal İlhan, Ali Rıza Yücel, Bora Gümüş, Mehmet Fatih Çelik, Çiğdem Demirtürk and all my other friends whose names I might have forgotten.

Finally, and most importantly, I owe a great debt to my dearest wife Seda İnel for being patient, loving, encouraging and supportive in all stages of this study.

TABLE OF CONTENTS

ABSTRACT	v
ÖZ	vii
ACKNOWLEDGEMENTS	x
TABLE OF CONTENTS	xi
LIST OF TABLES	xv
LIST OF FIGURES	xvi
LIST OF SYMBOLS	xix
CHAPTERS	
1. INTRODUCTION	1
1.1. Background	1
1.2. Literature Survey	2
1.3. Scope and Outline of the Thesis	4
2. DAMAGE OBSERVATION FOR MASONRY WALLS	7
2.1. Introduction	7
2.2. Field Observation of Damage on Perforated Masonry Walls	9
2.3. Experimental Observation of Damage on Solid Masonry Walls	13
2.4. Experimental Observation of Damage on Perforated Masonry Walls	18
2.5. Discussion of Observations	21
3. NUMERICAL ANALYSIS OF PROTOTYPE URM WALLS	23
3.1. Introduction	23
3.2. Material Modeling of Masonry	23
3.3. Nonlinear Pushover Analysis of Prototype URM Walls	27

3.3.1. Nonlinear Modeling Strategy	28
3.3.2. Nonlinear Pushover Analysis Results	29
3.3.2.1. Nonlinear Pushover Analysis Results of Wall Model E1	29
3.3.2.2. Nonlinear Pushover Analysis Results of Wall Model E2.....	31
3.3.2.3. Nonlinear Pushover Analysis Results of Wall Model E3.....	33
3.3.2.4. Nonlinear Pushover Analysis Results of Wall Model E4.....	35
3.3.2.5. Nonlinear Pushover Analysis Results of Wall Model E5.....	37
3.3.2.6. Nonlinear Pushover Analysis Results of Wall Model E6.....	39
3.4. Ultimate Strength of URM Walls from Empirical Formulations	41
3.4.1. Collapse Mechanism of Perforated URM Walls	41
3.4.1.1. Calculation of Pier Stiffnesses.....	41
3.4.1.2. Collapse Mechanism of Different Wall Types	42
3.4.2. FEMA 273 Approach for Lateral Strength Calculation	43
3.4.3. TBSC (2018) Approach for Lateral Strength Calculation.....	47
3.4.4. Lateral Strength Calculations by Akhaveissy (2013).....	49
3.4.5. Comparison of the Calculated Limit Strengths	52
3.5. Determination of Initial Crack Locations	53
3.5.1. “Coulomb-Mohr” Failure Criterion.....	53
3.5.2. Linear Modeling Procedure and Details.....	56
3.5.3. Analysis Results of Linear Numerical Modeling.....	60
3.5.3.1. Linear Analysis Results of Wall Model E1	60
3.5.3.2. Linear Analysis Results of Wall Model E2	62
3.5.3.3. Linear Analysis Results of Wall Model E3	63
3.5.3.4. Linear Analysis Results of Wall Model E4	65

3.5.3.5. Linear Analysis Results of Wall Model E5.....	67
3.5.3.6. Linear Analysis Results of Wall Model E6.....	69
3.6. Crack Propagation Analysis	70
3.6.1. Post Processing Procedure	70
3.6.2. Results of Post Processing Approach	72
3.6.2.1. Wall Model E1	72
3.6.2.2. Wall Model E2	74
3.6.2.3. Wall Model E3	75
3.6.2.4. Wall Model E4	77
3.6.2.5. Wall Model E5	78
3.6.2.6. Wall Model E6	80
3.7. Discussions of Numerical Calculations.....	81
4. SET OF RULES TO ESTIMATE DAMAGE PATTERNS OF URM WALLS	83
4.1. Introduction	83
4.2. Classification of Field Observations	83
4.3. Rules for Damage Patterns of URM Walls	83
4.4. Verification Study	86
5. SUMMARY AND CONCLUSIONS	93
5.1. Summary and Conclusions	93
5.2. Future Research Recommendations	95
REFERENCES.....	97
APPENDICES	
A. Field Observation of Damage on Perforated Masonry Walls Photo Archive ..	105

B. Experimental Observation of Damage on Perforated Masonry Walls Photo Archive	128
C. Ultimate Limit State Calculation Details	133
D. Classification of the Field Observation Table	146

LIST OF TABLES

TABLES

Table 2.1. Damaged Perforated Wall Photographs in Real Seismic Events.....	11
Table 2.2. Summary Table for Failure Modes of Different Solid Walls	15
Table 2.3. Damaged Perforated Wall Photographs in Experimental Studies	19
Table 3.1. Material Properties of Masonry	46
Table 3.2. Ultimate Lateral Load Capacities as per FEMA 273	46
Table 3.3. Ultimate Lateral Load Capacities as per TBSC 2018.....	49
Table 3.4. Ultimate Lateral Load Capacities as per Akhaveissy Approach.....	52
Table 3.5. Comparison Table of Ultimate Lateral Loads as per Different Numerical Approaches, Experimental and Nonlinear Analysis Results (in kN).....	52
Table 3.6. Stress Conditions and Color Categorization	59
Table 4.1. Summary Table for Damage Pattern Rules of URM Walls.....	86
Table 4.2. Comparison of Expected and Real Failure Modes of URM Walls.....	89
Table A.1. Damaged Perforated Wall Photographs in Real Seismic Events.....	105
Table B.1. Damaged Perforated Wall Photographs in Experimental Studies.....	128
Table D.1. Classification Table for Site Post EQ Damage Observations	147

LIST OF FIGURES

FIGURES

Figure 1.1. Different Modeling Techniques of Masonry Walls	2
Figure 1.2. (a) Micro and (b) Macro Modelling Principles	3
Figure 1.3. Pier (on the right) and Spandrel (on the left) Failure Mechanism of URM Buildings.....	4
Figure 2.1. Panel Definition in Perforated Walls	8
Figure 2.2. In- plane Failure Modes of Masonry: (a) Diagonal Tension, (b) Sliding Shear, (c) Rocking and (d) Toe Crushing.....	9
Figure 2.3. Types of Perforated Masonry Walls: (a) Type-1, (b) Type-2, (c) Type-3, (d) Type-4, (e) Type-5 and (f) Type-6.....	10
Figure 2.4. Before and After Testing Specimen ID: S2	17
Figure 2.5. After Testing of Specimen ID: S17.....	17
Figure 2.6. After Testing of Specimen ID: S25.....	18
Figure 3.1. Compression Material Model of Masonry by Kaushik et al. (2007)	25
Figure 3.2. Tension Material Model of Masonry by Dhanasekar and Haider (2007).....	25
Figure 3.3. Masonry Wall Experimental Set-up.....	28
Figure 3.4. Wall Model E1 Geometric Properties	30
Figure 3.5. Wall Model E1 Nonlinear Analysis Results	31
Figure 3.6. Wall Model E2 Geometric Properties	32
Figure 3.7. Wall Model E2 Nonlinear Analysis Results	32
Figure 3.8. Wall Model E3 Geometric Properties	34
Figure 3.9. Wall Model E3 Nonlinear Analysis Results	34
Figure 3.10. Wall Model E4 Geometric Properties	36
Figure 3.11. Wall Model E4 Nonlinear Analysis Results	36
Figure 3.12. Wall Model E5 Geometric Properties	38
Figure 3.13. Wall Model E5 Nonlinear Analysis Results	38

Figure 3.14. Wall Model E6 Geometric Properties.....	40
Figure 3.15. Wall Model E6 Nonlinear Analysis Results	40
Figure 3.16. Determination of the Effective Height, h' (Dolce 1997).....	42
Figure 3.17. (a – c) Collapse Mechanism of Different Masonry Perforation Types .	43
Figure 3.18. Compressive Areas of Masonry Components Under Different Eccentricity Levels.....	48
Figure 3.19. Stress Element on the Failure Surface and The Principle Plane.....	50
Figure 3.20. α Coefficient Curves Proposed by Akhaveissy (2013).....	51
Figure 3.21. Coulomb-Mohr Failure Criteria.....	55
Figure 3.22. Typical Modeling Scheme and Boundary Details	58
Figure 3.23. Coulomb-Mohr Failure Criteria with Stress Conditions	59
Figure 3.24. Wall Model E1	61
Figure 3.25. Stress Distribution Diagram of Wall Model E1	61
Figure 3.26. Wall Model E2.....	62
Figure 3.27. Stress Distribution Diagram of Wall Model E2	63
Figure 3.28. Wall Model E3.....	64
Figure 3.29. Stress Distribution Diagram of Wall Model E3	65
Figure 3.30. Wall Model E4.....	66
Figure 3.31. Stress Distribution Diagram of Wall Model E4	67
Figure 3.32. Wall Model E5.....	68
Figure 3.33. Stress Distribution Diagram of Wall Model E5	68
Figure 3.34. Wall Model E6.....	69
Figure 3.35. Stress Distribution Diagram of Wall Model E6	70
Figure 3.36. Flowchart of the Post Processing Procedure	72
Figure 3.37. Post Processing Steps for Wall Model E1	73
Figure 3.38. Expected Crack Pattern of Wall Model E1.....	74
Figure 3.39. Post Processing Steps for Wall Model E2	74
Figure 3.40. Expected Crack Pattern of Wall Model E2.....	75
Figure 3.41. Post Processing Steps for Wall Model E3	76
Figure 3.42. Expected Crack Pattern of Wall Model E3.....	77

Figure 3.43. Post Processing Steps for Wall Model E4.....	77
Figure 3.44. Expected Crack Pattern of Wall Model E4	78
Figure 3.45. Post Processing Steps for Wall Model E5.....	79
Figure 3.46. Expected Crack Pattern of Wall Model E5	80
Figure 3.47. Post Processing Steps for Wall Model E6.....	80
Figure 3.48. Expected Crack Pattern of Wall Model E6	81
Figure 4.1. Window wall and out-of-plane wall of the tested structure (Costley et al. 1996).....	87
Figure 4.2. Geometric properties of Wall ID W1 and W2	87
Figure 4.3. Expected vs. Real Damage Patterns of Wall ID. W1	90
Figure 4.4. Expected vs. Real Damage Patterns of Wall ID. W2.....	90
Figure C.1. Wall Type-1 Limit Strength Calculations	135
Figure C.2. Wall Type-2 Limit Strength Calculations	137
Figure C.3. Wall Type-3 Limit Strength Calculations	139
Figure C.4. Wall Type-4 Limit Strength Calculations	141
Figure C.5. Wall Type-5 Limit Strength Calculations	143
Figure C.6. Wall Type-6 Limit Strength Calculations	145

LIST OF SYMBOLS

SYMBOLS

A_n	Area of net mortared/grouted section
C	Cohesion of the mortar joints
d	Length of pier
E_m	Elastic modulus of masonry
f_a	Gravitational compressive force on masonry wall
f_m	Compressive strength of masonry
f_t	Tensile strength of masonry
F_t	Tensile strength of mortar joints
f_{vk}	Characteristic shear capacity of masonry walls, considering the average axial stresses on the wall
f_{vko}	Characteristic shear capacity of masonry walls, without considering the axial stresses
h	Effective height of the pier
h_{eff}	Height of resultant of lateral force
f_m	Compressive strength of masonry
k	Rigidity of pier
L	Length of wall
l_c	Length of compressive part of masonry
P	Ultimate lateral force that wall safely resist

P_{CE}	Expected vertical axial compressive force
P_u	Resistant lateral force
t	Thickness of wall or pier component
V_{bjs}	Lateral strength of wall or pier based on bed-joint shear strength
V_{dt}	Lateral strength of wall or pier under diagonal tension failure mode
V_{tc}	Lateral strength of wall or pier under toe crushing failure mode
v_{me}	Expected bed-joint sliding shear strength
V_r	Lateral rocking strength of wall or pier
V_{rm}	Lateral resistance force of masonry component
x_{min}	Effective length of the wall
α	Factor due to end boundary conditions of wall
λ	Aspect ratio (height / length)
σ	Axial stress
ε_m	Strain of masonry
φ	Internal friction angle of mortar joints
ν_m	Poisson's ratio
τ_u	Ultimate shear strength of masonry
τ_{emm}	Allowable shear strength of masonry
θ	The angle of principal plane

CHAPTER 1

INTRODUCTION

1.1. Background

Masonry is still one of the most common construction types in the world due to the accessibility of materials in any environment conditions, ease of application, and low costs. Among the many types of masonry structures, the most common type is unreinforced masonry (URM) structures.

URM structures have high compressive strength under axial loads, yet have little or no tensile strength, which often leads to failure in a brittle manner. Because of their large mass and lack of ductility, they are subjected to relatively high seismic actions which lead to structural failure more often than any other types of structures. Hence, URM structures are very vulnerable in zones of high seismicity.

The seismic behavior of URM structures in rural areas cannot be accurately estimated because there is no control in their construction process, material properties are not precisely known, and they are generally constructed with previous experiences in a traditional manner. Hence, they are also considered as non-engineered structures. Using detailed modeling and analysis approaches for assessment purposes is waste of time and effort since the input structural parameters cannot be obtained with an adequate degree of accuracy. In such cases, simplified and practical approaches should be employed, but this requires a good understanding of the actual behavior under seismic action. The only way to comprehend actual behavior is to gather and examine field data from real structures or processed data from physical test models under laboratory conditions. This study focuses on collecting such data for the in-plane seismic behavior of perforated unreinforced masonry walls and develops a solid basis

for simplified modeling and analysis techniques to estimate the seismic performance of non-engineered masonry buildings.

1.2. Literature Survey

In this section, studies regarding different modelling techniques about URM walls are explained. Then, collapse mechanisms of URM structures are described.

Based on the study of Lourenco et al. (1995), there are two major techniques in modeling masonry. These are heterogeneous (micro) modeling and homogeneous (macro) modeling. Heterogeneous modeling is composed of two sub-techniques micro modeling and simplified micro modeling (Figure 1.1).

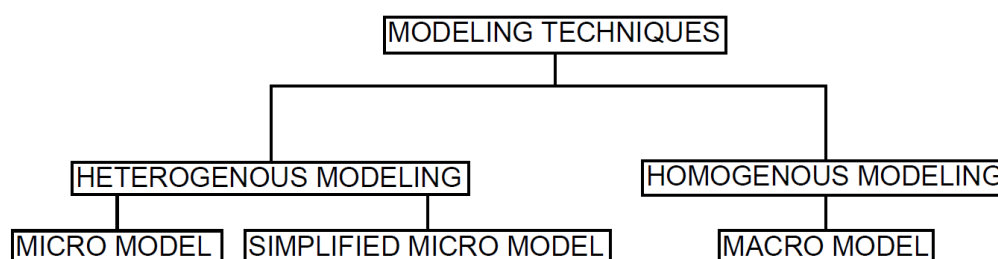


Figure 1.1. Different Modeling Techniques of Masonry Walls

URM walls consist of masonry units and mortar. In micro modeling approach masonry unit, mortar and their joint behavior at interfaces are modeled separately as shown in Figure 1.2a. On the other hand, in macro modeling, mortar and masonry units are modeled as a single element as shown in right of Figure 1.2b. These two modelling techniques of URM walls have advantages and disadvantages. With the help of micro modeling approaches, users can determine more precise results on behavior of URM walls and ultimate limits. However, this approach consumes very significant computational time compared to macro modeling approaches. Moreover, material properties of mortar and masonry units should be properly defined in the beginning of

modeling stage. Despite the definition of micro modeling, macro modeling approach is much more practical to model and obtain such results. Nevertheless, results are less precise compared to micro modeling.

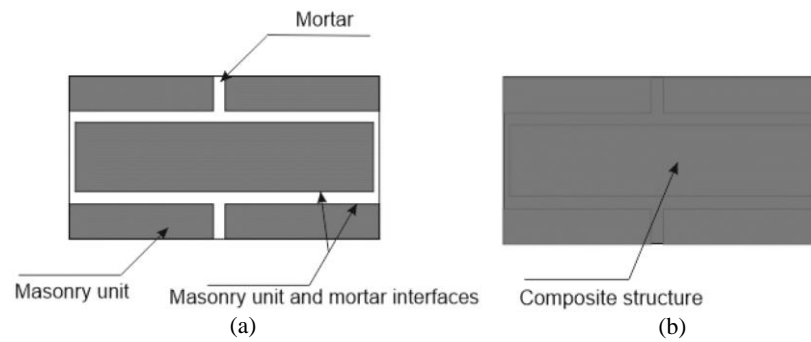


Figure 1.2. (a) Micro and (b) Macro Modelling Principles

Macro modeling technique is used in this study (Computers and Structures, 2009). The studies by Kaushik et al. (2007), Dhanasekar and Haider (2007) and Mosalam et al. (2009) have been investigated to determine the mechanical and non-linear properties of masonry developing the mathematical models.

There are two common behavior types for collapse mechanisms in URM buildings: “weak pier” and “weak spandrel” failure mechanisms (Figure 1.3). From the structural point of view, pier failure is the predominant failure type on total collapse of structure, therefore, it is more critical than failure in spandrels.

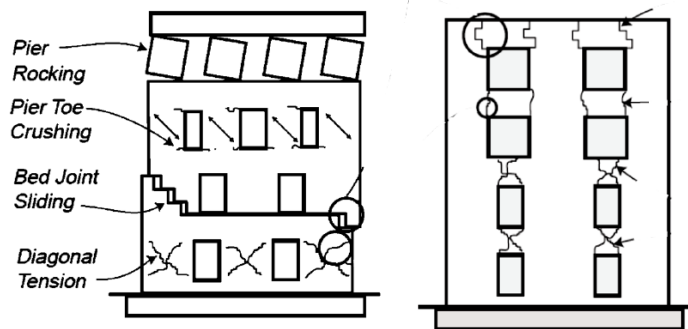


Figure 1.3. Pier (on the right) and Spandrel (on the left) Failure Mechanism of URM Buildings

It is also essential to understand the in-plane behavior of URM walls and determine their in-plane ultimate strength limits from the view of the international codes and standards. Therefore, FEMA 273 (1997), Turkish Building Seismic Code (TBSC 2018: Disaster and Emergency Management Presidency, 2019) and the state-of-the-practice study by Akhaveissy (2013) are considered. Consequently, ultimate limit approaches of different empirical equations are assessed.

1.3. Scope and Outline of the Thesis

This thesis study focuses on the development of pre-established rules regarding crack patterns and damage propagation for URM solid or perforated walls to develop a solid basis for simplified modeling and analysis techniques for the estimation of the seismic performance of unreinforced masonry buildings. In order to develop these rules, both observed data (either from field surveys or from laboratory tests) and numerical data (mathematical model analyses) are assessed.

Failure modes and crack propagations of URM buildings under seismic actions depend on both in-plane and out-of-plane behaviors. The aim of this study is to determine predefined rules for damage pattern predictions by using simplified techniques. Out-of-plane behavior is not considered in this study due to the fact that, interpreting this phenomenon requires much more complicated analysis and numerical calculations than that in-plane behavior.

In addition, ultimate capacities of the selected URM walls are investigated. Results of the experimental studies are compared with limitations given in empirical equations as well as numerical modeling analysis results. Thus, a complete set of knowledge on failure mechanism and in-plane behavior is gathered. The developed set of rules is intended to be used to predict the failure surfaces for the façades of URM structures with only the help of observational information from the observed and numerical data belonging to masonry walls.

Finally, the obtained set of rules can assist the estimation of lateral failure load through lower-bound limit analysis. Hence this approach provides a practical and reasonable tool to predict the lateral load capacity of simple URM buildings without performing any complicated analysis.

In the following pages, details of this study are presented in below order.

Chapter 1 is about the introduction, literature survey and scope of this study.

Chapter 2 focuses on damage observations of URM walls. Damage patterns from different post-earthquake field reports and experimental studies are investigated and categorized according to their perforation geometry.

Chapter 3 calculates ultimate strength values of URM walls by using linear and non-linear analyses and crosschecks these results with experimental studies. Moreover, empirical strength limits from several international codes are determined and compared.

Chapter 4 classifies the damage observations of field reports and gives a set of rules for predefined damage patterns on perforated URM walls.

Chapter 5 concludes this study by giving a summary and suggests future works in consideration of the results obtained.

CHAPTER 2

DAMAGE OBSERVATION FOR MASONRY WALLS

2.1. Introduction

In this chapter, damaged patterns of unreinforced masonry walls obtained from field and experimental observations are examined. The main objective of this chapter is to comprehend the in-plane damage and failure modes of masonry walls and to examine the effect of geometry, material properties, axial stress and perforations in the wall (i.e. the number and position of wall openings) on the considered damage and failure modes. Masonry wall damage is discussed in three different subsections which are titled as: field observation of damage on perforated masonry walls, experimental observation of damage on solid masonry walls and experimental observation of damage on perforated masonry walls. Finally, the gathered information is presented in tabular form.

URM walls are classified as three different groups according to their axial stress levels (σ). The first one is defined as “low” axial stress with values ranging from 0.05 MPa to 0.10 MPa, indicating walls located in one story buildings or at the top story of multi-story buildings. URM walls at intermediate floors of three-story buildings belong to the group of “medium” axial stress, for which the values correspond to $\sim 0.15 - 0.25$ MPa. URM walls of bottom floors of three-story buildings are assumed to be under “high” axial stress, which corresponds to values between $\sim 0.30 - 0.40$ MPa.

Moreover, geometric properties of masonry walls have a significant effect on the damage patterns. This particular feature is determined by introducing the aspect ratio of the URM walls. An important issue to be mentioned here is the fact that the damage patterns of the perforated walls are observed in different parts of the wall. Therefore, assessment of the URM walls is performed by dividing them into predefined

imaginary panels. Aspect ratios are determined with consideration of the dimensions of these panels. Definition of these panels in perforated walls is shown in Figure 2.1. According to the below figure, panels are defined into three groups regarding to their locations on the wall. These are pier (P), spandrel (S) and corner (C). Pier denotes the panel between two openings in the horizontal alignment whereas spandrel represents the panel between two openings in the vertical alignment. The remaining parts of the wall are considered as corner.

Panel based modeling is used for the walls in order to distinguish areas for piers, spandrels and in between zone which have different behavior patterns. With the help of equilibrium conditions between panels, stress states of panels can be estimated from expected damage and crack patterns.

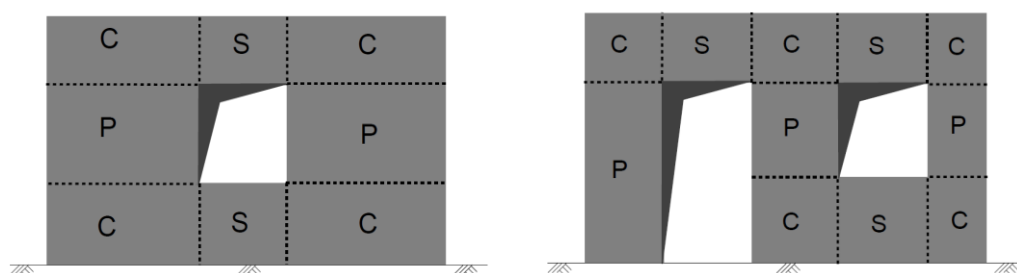


Figure 2.1. Panel Definition in Perforated Walls

Aspect ratio (λ) of the panels is defined as the ratio of the height of the panel to its length. It is classified in three groups: squat ($\lambda < 1.0$), normal ($1.0 < \lambda < 2.0$) and slender ($\lambda > 2.0$) panels.

Another important factor that affects the damage of the masonry walls is the material property. This parameter is combined with the workmanship (or observed quality) of the walls and classified into three groups as low, medium and high.

Effects of aforementioned parameters of URM walls determine the in-plane failure modes. In URM wall panels, there are four major in-plane failure modes observed under earthquake action or experimental studies. (Figure 2.2):

- Diagonal tension failure
- Sliding shear failure
- Rocking failure
- Toe crushing failure

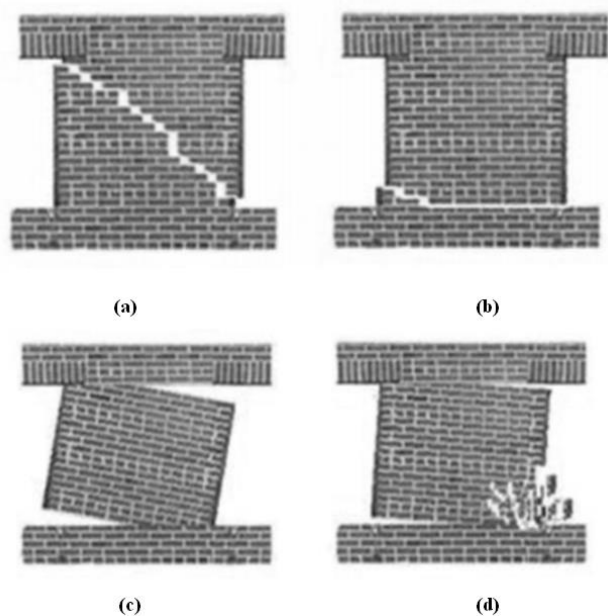


Figure 2.2. In- plane Failure Modes of Masonry: (a) Diagonal Tension, (b) Sliding Shear, (c) Rocking and (d) Toe Crushing

2.2. Field Observation of Damage on Perforated Masonry Walls

In this section, damaged perforated walls in seismic events are examined. A vast number of post-earthquake field investigation reports have been studied and photos of damaged masonry structures are collected.

For all wall types, seismic behavior and failure modes of the walls are assessed as single story wall even if they are part of a multistory structure. Since the stories of masonry structures are separated with rigid floors and tie beams, behavior of each story can be considered as an individual single-story structure with lower and upper stories as the boundary.

Masonry walls are categorized into six types according to their wall opening properties. Categorized wall type descriptions (Figure 2.3) are: Type-1 wall which consists of a single window opening, Type-2 wall which consists of a single door opening, Type-3 wall which consists of a single door and a single window opening, Type-4 wall which consists of two window openings, Type-5 wall which consists of more than two window openings and finally Type-6 wall which consists of at least single door opening and two or more window openings. Locations and orientations of the openings are not restricted in the categorization.

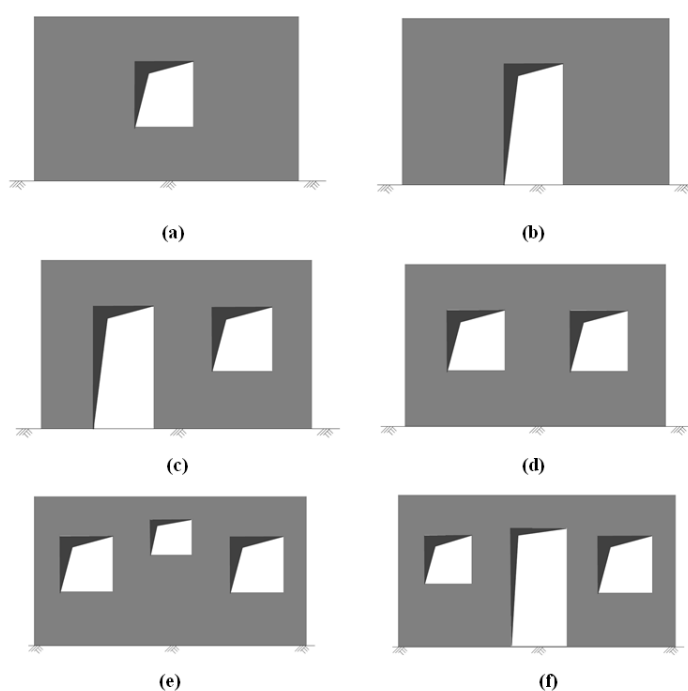


Figure 2.3. Types of Perforated Masonry Walls: (a) Type-1, (b) Type-2, (c) Type-3, (d) Type-4, (e) Type-5 and (f) Type-6.

Three major parameters are visually determined for each masonry wall: axial stress level, material type and aspect ratio together with the observed crack pattern of the considered wall. Axial stress level of the walls is determined by the number of stories above the inspected wall. For instance, if there is no story above the inspected wall as in single-story structures or top story of multi-story structures, axial stress level of the wall is defined as “low”. In Table 2.1, sample photos of each type of damaged wall are presented. Wall IDs are given as F1-F70 as shown in Appendix A for the rest of the cases together with damaged wall photos.

Table 2.1. *Damaged Perforated Wall Photographs in Real Seismic Events*

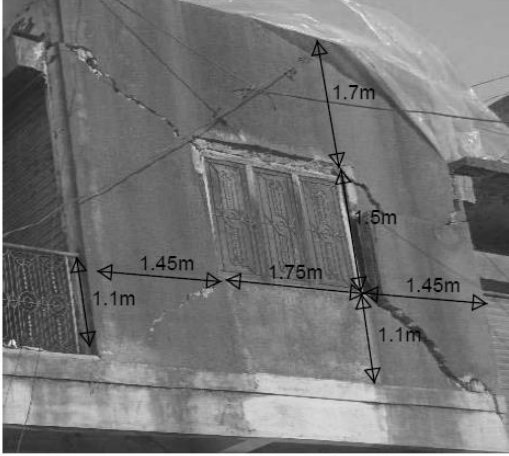
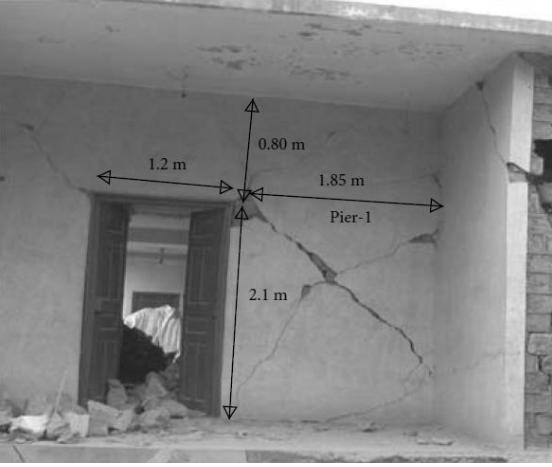
	<ul style="list-style-type: none"> - Wall type: 1 - Wall ID: F1 - Axial stress level: Low - Material type: Solid clay - Reference: Javed et al. (2006)
	<ul style="list-style-type: none"> - Wall type: 2 - Wall ID: F15 - Axial stress level: Low - Material type: Hollow clay - Reference: Javed et al. (2006)

Table 2.1 (continued)

	<ul style="list-style-type: none"> - Wall type: 3 - Wall ID: F23 - Axial stress level: Medium - Material type: Clay - Reference: Javed et al. (2006)
	<ul style="list-style-type: none"> - Wall type: 4 - Wall ID: F29 - Axial stress level: Low - Material type: Stone - Reference: Auroville Earth Insitute (2015)
	<ul style="list-style-type: none"> - Wall type: 5 - Wall ID: F49 - Axial stress level: Low - Material type: Clay - Reference: Javed et al. (2006)

Table 2.1 (continued)

	<ul style="list-style-type: none"> - Wall type: 6 - Wall ID: F68 - Axial stress level: Low - Material type: Solid clay - Reference: Auroville Earth Insitute (2015)
--	--

Damaged walls presented in Table 2.1 show that axial stress level, material property and aspect ratio have a significant effect on damage patterns of perforated URM walls. Depending on the perforation geometry, crack patterns, crack initialization and crack propagation have consistent trends. In most of the observed walls, cracks initiate from corners of openings. Furthermore, propagation of these cracks seems to be related with the axial stress level, material properties and geometry of the panels around the openings. Thus, crack patterns can be roughly predicted by considering these three parameters.

2.3. Experimental Observation of Damage on Solid Masonry Walls

It is essential to examine the in-plane behavior and the correlated damage patterns of solid masonry walls since such walls exist in almost all of the masonry buildings. Moreover, in-plane behavior of panels in perforated walls has lots of similarities with the in-plane behavior of simple solid walls.

Different failure modes of unreinforced solid masonry walls have been described in Chapter 1. As mentioned before, each failure mode occurs due to different properties of masonry walls. Major parameters which lead to failure modes are observed as aspect ratio (λ), vertical axial stress (σ) and compressive strength of masonry (f_m).

In order to interpret the failure modes and in-plane behavior of solid URM walls, 60 different experimental set-ups are examined. Most of the experimental studies belong to well recognized researchers in the field. In Table 2.2, a summary list is prepared and presented for the solid wall experimental studies. The abbreviations used in the table can be summarized as follows. For material types,

SB: Stone block

CCB: Concrete block

SCB: Solid clay brick

HCB1/2/3: (1) Hollow clay brick without filled mortared joints, (2) Hollow clay brick with fully mortared joints, (3) Hollow clay brick with fully mortared joints and fine hollows

TGM: Clay tongue and groove masonry (no mortar in between)

For failure modes,

1: Diagonal tension failure

2: Slide shear failure

3: Rocking - flexural (toe crush) failure

4: Mixed failure mode (diagonal shear and rocking)

To explain the constitution of Table 2.2, three examples are given for each failure modes.

Table 2.2. Summary Table for Failure Modes of Different Solid Walls

Specimen ID	Masonry Material	Aspect Ratio (λ)	Length (mm)	Height (mm)	Thickness (mm)	Comp. Strength (f_m) (Mpa)	Vertical Axial Stress (MPa)	Lateral Load (kN)	Failure Mode	Referred Paper
S1	SCB	1	600	600	90	8.44	0.32	84	2	Basoenondo (2008)
S2	SCB	1	600	600	90	8.44	0.42	54	1	
S3	SCB	1	600	600	90	8.44	0.17	74	2	
S4	SCB	1	600	600	90	8.44	0.24	82	2	
S5	SCB	1	600	600	110	10.03	0.14	177	1	
S6	SCB	1	600	600	110	10.03	0.20	140	1	
S7	SCB	1	600	600	110	10.03	0.27	145	1	
S8	SCB	1	600	600	110	12.37	0.14	126	1	
S9	SCB	1	600	600	110	12.37	0.20	123	1	
S10	SCB	1	600	600	110	12.37	0.27	121	1	
S11	SB	0.6	4400	2620	320	3.28	0.09	80	1	Magenes et al. (2012)
S12	CCB	0.6	3600	2000	150	7.61	0.77	234	1	Farshchi et al. (2009)
S13	CCB	0.6	3600	2000	150	7.61	0.78	187	1	
S14	HCB1	1	1600	1600	75	6.00	0.75	32	3	ElGawady et al. (2005)
S15	HCB1	1	1600	1600	75	4.80	0.37	20	2	
S16	HCB1	0.4	1600	700	75	6.00	0.32	29	4	
S17	HCB1	0.4	1600	700	75	4.80	0.29	29	2	
S18	HCB1	1.1	2010	2250	195	8.99	1.07	187	1	Petry and Beyer (2015)
S19	HCB1	1.1	2010	2250	195	9.75	1.07	178	1	
S20	HCB1	1.1	2010	2250	195	12.00	1.07	121	3	
S21	HCB1	1.1	2010	2250	195	11.70	1.58	145	4	
S22	HCB1	1.1	2010	2250	195	9.87	0.56	135	1	
S23	HCB1	1.1	2010	2250	195	9.02	1.58	132	4	
S24	SCB	1.0	990	1000	100	9.50	0.30	52	1	Lourenço et al. (1995)
S25	SCB	0.6	3600	2000	150	9.50	0.61	255	1	
S26	HCB1	0.5	3567	1625	198	6.40	0.52	425	1	Abrams and Shah (1992)
S27	HCB1	0.6	2743	1625	198	6.40	0.52	190	3	
S28	HCB1	0.9	1829	1625	198	6.40	0.52	100	3	
S29	HCB1	0.6	3600	2000	150	8.25	0.77	260	1	Ganz and Thurlimann (1985)
S30	HCB1	0.6	3600	2000	150	8.25	2.38	454	4	
S31	HCB1	0.6	3600	2000	150	8.25	0.78	187	4	
S32	HCB1	0.6	3600	2000	150	8.25	0.77	247	-	
S33	HCB1	0.6	3600	2000	150	8.25	2.39	491	4	

Table 2.2 (continued)

Specimen ID	Masonry Material	Aspect Ratio (λ)	Length (mm)	Height (mm)	Thickness (mm)	Compres. Strength (fm) (Mpa)	Vertical Axial Stress (Mpa)	Lateral Load (kN)	Failure Mode	Referred Paper
S34	SCB	0.8	1800	1500	150	9.40	-	75	3	Petry and Beyer (2014)
S35	HCB2	1.5	1028	1510	300	4.00	0.6	-	3	
S36	HCB2	1.5	1030	1510	300	4.10	1.19	-	3	
S37	HCB2	1.5	1025	1514	300	4.10	1.19	-	3	
S38	HCB2	1.5	1026	1508	300	4.00	0.6	-	3	
S39	HCB1	1.5	989	1513	300	4.25	1.19	-	3	
S40	HCB1	1.5	987	1511	300	4.25	1.19	-	3	
S41	HCB1	1.5	988	1507	300	4.25	1.19	-	3	
S42	HCB3	1.5	985	1508	300	6.26	1.19	-	3	
S43	HCB3	1.5	985	1509	300	6.26	1.19	-	3	
S44	HCB3	1.5	986	1507	300	6.26	1.19	-	3	
S45	TGM	1.5	988	1510	300	6.26	1.19	-	3	
S46	TGM	1.5	987	1512	300	6.26	1.19	-	3	
S47	TGM	1.5	986	1508	300	6.26	1.19	-	3	
S48	HCB2	0.7	2567	1750	297	4.21	0.59	-	4	
S49	HCB2	0.7	2572	1753	297	4.10	1.19	-	4	
S50	HCB2	0.7	2584	1751	297	4.05	0.89	-	4	
S51	TGM	0.7	2482	1750	296	4.32	0.95	-	1	
S52	TGM	0.7	2484	1750	296	2.41	0.53	-	3	
S53	HCB3	0.7	2359	1600	247	3.86	0.85	-	3	
S54	HCB2	0.7	2712	1820	172	9.41	2.07	-	4	
S55	TGM	1.2	992	1170	300	5.53	0.94	-	3	
S56	TGM	1.2	992	1170	300	5.64	1.24	-	1	
S57	TGM	1.2	992	1170	300	5.74	1.55	-	3	
S58	HCB3	1.2	992	1170	300	5.24	0.89	-	3	
S59	HCB3	1.2	992	1170	300	5.18	1.14	-	3	
S60	HCB3	1.2	992	1170	300	5.41	1.46	-	3	

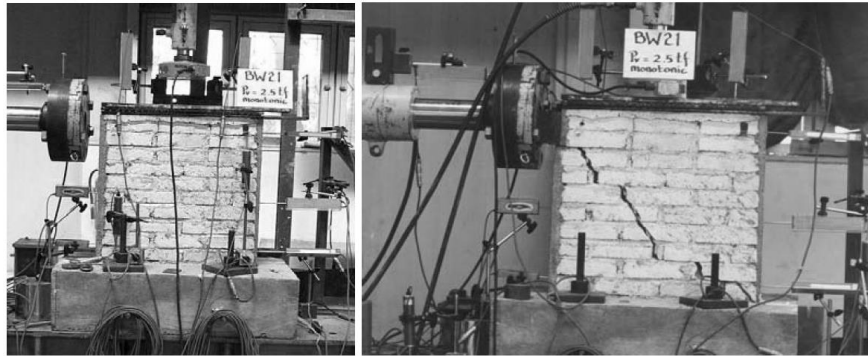


Figure 2.4. Before and After Testing Specimen ID: S2

Figure 2.4 shows a specimen that is selected from the collected experimental data for solid masonry walls Basoenondo (2008). The wall has an aspect ratio $\lambda=1$ with a thickness of 90mm. Wall material is standard solid clay brick with compressive strength $f_m=8.44$ MPa. Vertical axial stress on the specimen was 0.42 MPa. Under the given conditions, diagonal tension failure was observed at ultimate loading.

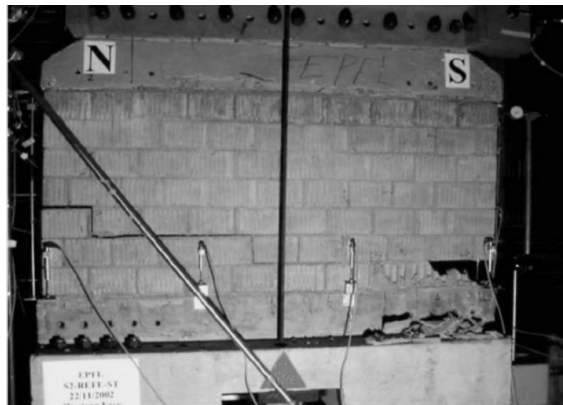


Figure 2.5. After Testing of Specimen ID: S17

Figure 2.5 shows a specimen that is selected from ElGawady et al. (2005). The wall has an aspect ratio $\lambda=0.4$ with a thickness of 75mm. Wall material is standard hollow clay brick with compressive strength $f_m=4.8$ MPa. Vertical axial stress on the

specimen was 0.29 MPa. Under the given conditions, sliding shear failure was observed at ultimate loading.

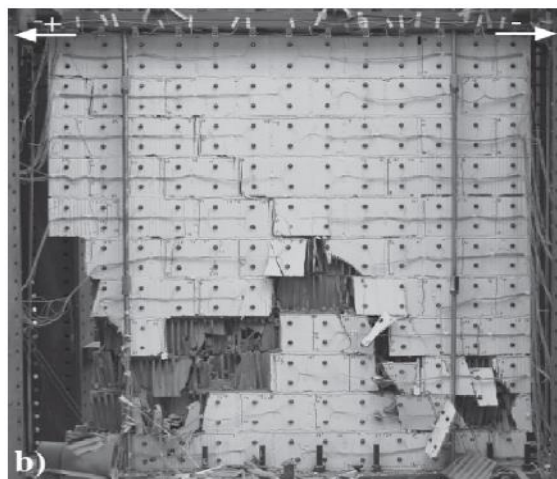


Figure 2.6. After Testing of Specimen ID: S25

Figure 2.6 shows a specimen that is selected from Petry and Beyer (2014). The wall has an aspect ratio $\lambda=1.1$ with a thickness of 195mm. Wall material is standard hollow clay brick with compressive strength $f_m=11.7$ MPa. Vertical axial stress on the specimen was 1.58MPa. Under the given conditions, mixed failure mode consisting of diagonal shear failure and rocking failure was observed at ultimate loading.

In the light of above findings, 60 different experimental studies that were examined can assist in solid conclusions for the behavior of solid walls under lateral loadings. Aspect ratio, vertical axial stress and material strength seem to have a significant effect on the determination of failure modes as expected.

2.4. Experimental Observation of Damage on Perforated Masonry Walls

Several experimental studies from literature have been reviewed to investigate the influence of major parameters (i.e. material properties, geometrical properties and loading conditions) on damage and crack propagation of perforated masonry walls.

In Table 2.3, samples for each type of damaged walls are presented. Rest of the damaged wall archive is presented in Appendix B. The wall types that are presented in Figure 2.3 have been used to categorize the experimental data.

Table 2.3. Damaged Perforated Wall Photographs in Experimental Studies

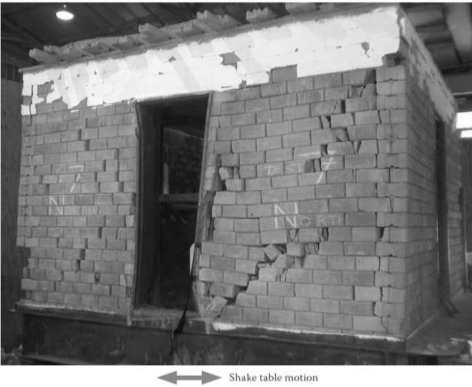
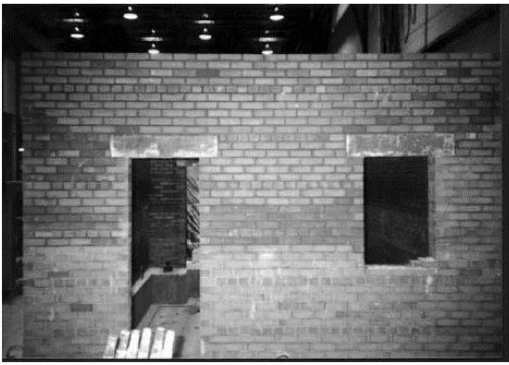
	<ul style="list-style-type: none"> - Wall type: 1 - Wall ID: E1 - Axial stress level: Low - Material type: Solid clay brick - Damage Pattern: Diagonal tension failure observed at corner panels. - Reference: Kalali and Kabir (2012)
	<ul style="list-style-type: none"> - Wall type: 2 - Wall ID: E2 - Axial stress level: Low - Material type: Adobe brick - Damage Pattern: Diagonal tension failure observed. - Reference: Formica et al. (2002)
	<ul style="list-style-type: none"> - Wall type: 3 - Wall ID: E3 - Axial stress level: Low - Material type: Clay brick - Damage Pattern: Rocking failure is the dominant failure mode at slender piers. However, diagonal tension failure also observed - Reference: Paquette and Bruneau (2006)

Table 2.3 (continued)

	<ul style="list-style-type: none"> - Wall type: 4 - Wall ID: E4 - Axial stress level: Low - Material type: Clay brick - Damage Pattern: Diagonal tension failure is the dominant failure mode at all piers. - Reference: Abrams (1988)
	<ul style="list-style-type: none"> - Wall type: 5, 6 - Wall ID: E5 - Axial stress level: Low, medium - Material type: Solid clay brick - Damage Pattern: Sliding shear failure is the predominant failure mode at the lowest part of bottom floor wall. Additionally, Rocking and diagonal tension failure is occurred at piers. - Reference: Moon et al. (2007)
	<ul style="list-style-type: none"> - Wall type: 6 - Wall ID: E6 - Axial stress level: Low - Material type: Clay brick - Damage Pattern: Predominant failure is sliding shear failure. Besides this diagonal tension failure is occurred. - Reference: Nateghi and Alemi (2008)

Experimental studies listed in Table 2.3 indicate that failure modes and crack patterns are in accordance with the post-earthquake field observations presented in Section 2.2. Cracks are mostly initialized from the corners of the openings and propagate towards the edges of walls or the corners of adjacent openings. Moreover, axial stress level, material properties and aspect ratio of piers have a significant effect on failure modes. These parameters mostly affect the orientation of crack propagation and failure modes for the unreinforced masonry walls.

The experimental studies given in Table 2.3 (E1 – E6) have been selected for more detailed investigation with numerical modeling in Chapter 3. Moreover, there exist the calculations for estimating the ultimate lateral load capacities of the selected experimental studies by using the formulations obtained from several codes and standards.

2.5. Discussion of Observations

From the viewpoint of solid walls, rocking behavior is mostly observed in the slender walls where aspect ratio (λ) is greater than 2.0. Axial stress level and brick/mortar material quality also play an important role for rocking failure mode. When the quality of mortar and unit is low, the failure mode is sliding shear rather than rocking failure because the wall moment transfer is not completed which means structure fails before stress transfer completed. For walls with low axial stress, diagonal tension failure becomes a dominant failure mode before the rocking failure.

Diagonal tension behavior is mostly observed in normal or squat walls where aspect ratio (λ) is equal or smaller than 1.0. However, similar with the slender solid walls, brick/mortar material quality also plays an important role for diagonal tension behavior. As described in the above paragraph, walls with low quality of mortar/brick material mostly fail due to sliding shear.

Sliding shear behavior is mostly observed in squat walls where aspect ratio (λ) is smaller than 1.0. As described above sliding shear behavior mainly initiates due to low quality material and in some cases due to low axial stress.

In the perforated walls, most of the failures are initiated from the corners of openings. Stress concentrations occur around the corners of the openings due to discontinuity of walls. It is also observed that the crack propagation tends to find the easiest path to the closest stress concentration location such as the corner of the wall or the adjacent opening. Pier failure generally leads to global failure and individual pier behavior is very similar to the solid wall behavior.

CHAPTER 3

NUMERICAL ANALYSIS OF PROTOTYPE URM WALLS

3.1. Introduction

Field or experimental observations provide invaluable data to develop predefined damage and failure mechanisms for URM walls. However, obtained data is never a complete set due to either limited observations in the field or economic constraints in laboratory studies. Numerical analysis always fills the gap for required missing data. Accordingly, in this part of the thesis, numerical analyses are employed together with observational data to predict the failure patterns of solid or perforated URM walls. Crack initializing locations and damage modes of masonry walls are determined by using numerical analysis for six different cases (E1–E6) that have been selected in Section 2.3. Numerical models developed for these cases are analyzed in two steps by using SAP2000 software (CSI, 2009). In the first step, non-linear pushover analysis is performed. Lateral force vs. top displacement curves are developed for URM wall models and these curves are compared with the experimental results. Hence, the first step of the analysis is a verification step for the prototype URM wall models. In the second step, simplified failure analysis is performed for the same prototype wall models. Stress distributions of the walls are obtained under ultimate lateral loading. By employing the Coulomb-Mohr failure criteria, crack initializing locations are determined. Predominant stress states in different wall regions are obtained.

3.2. Material Modeling of Masonry

Determination of the ultimate strength of masonry walls is still a critical phenomenon. The most important source of the uncertainty involved is the material properties of masonry, which cannot be completely interpreted. Interaction between mortar and bricks, heterogeneous structure of the masonry and workmanship quality are the main

causes which affect the overall strength of masonry from specimen to specimen. Hence, many researchers have focused on determining the mechanical properties of masonry and finding the best empirical equations that fit the best relation between the ultimate strength and these mechanical properties.

Nevertheless, different from discrete modeling, nonlinear properties in continuum modeling of masonry are the most difficult parameters to be determined. Since mortar and bricks have different behavior, strength and mechanical properties, average values given in literature for composite masonry element should be considered in continuum models.

From the survey of many research studies, mechanical properties that are used in nonlinear continuum modeling stage can be summarized as follows:

Stress-strain curve: Compressive and tensile behavior of masonry are quite different from each other. As similar with concrete, masonry has a relatively high compressive strength than its tensile strength. In addition, due to highly heterogeneous behavior of the material, there are different material models proposed by different researchers for each stress condition. In this thesis study, compression model of masonry proposed by Kaushik et al. (2007) is used. In that study, it was indicated that the stress strain curve for compression can be divided into two parts: the first part has a parabolic variation which is ascending up to the peak ultimate strength point as given in Equation 3.1. Then comes a linearly descending portion, which is a function of the mortar type. Stress strain curve of the compression model is given in Figure 3.1.

$$\frac{f_m}{f'_m} = 2 * \frac{\varepsilon_m}{\varepsilon'_m} - \left(\frac{\varepsilon_m}{\varepsilon'_m}\right)^2 \quad (3.1)$$

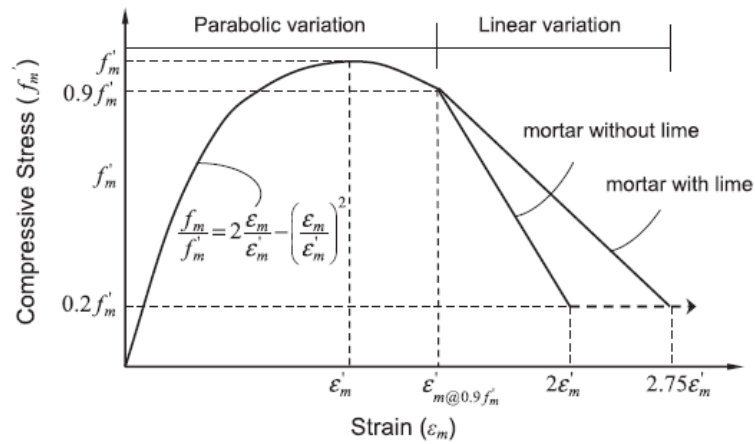


Figure 3.1. Compression Material Model of Masonry by Kaushik et al. (2007)

For the tension model of masonry, a simplified tri-linear curve as in Figure 3.2, which is based on Dhanasekar and Haider (2007) is used. The strain at peak tensile strength of masonry (f_t) is 0.0001 whereas the fracture strength is 0.02 MPa at a strain value of 0.008.

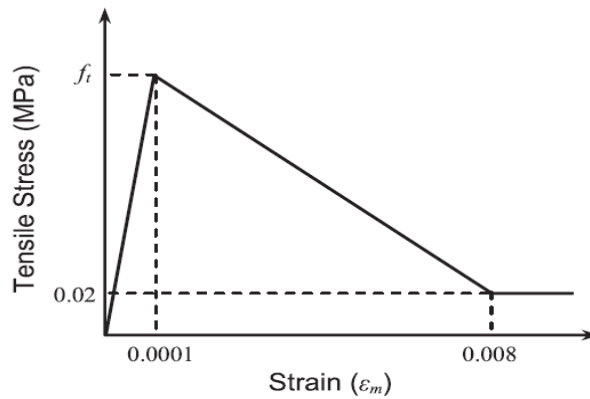


Figure 3.2. Tension Material Model of Masonry by Dhanasekar and Haider (2007)

In the selected experimental studies, which are used in numerical stage, not all of the material properties are provided. Given equations in this section are used to determine for these missing material properties. In fact, a range of a set of data is present in these equations. Therefore, for the numerical modeling stages, an iterative approach used in these equations to get the best fit analysis results compared to the experimental results.

Above-mentioned stress-strain models are used for different stress levels. At least one of the compressive or tensile strength values has already been provided in the documentation of the related experimental study given in Section 2.4. In case of lack of information in one strength value, Equation 3.2 based on ASTM C55 (2017) criterion gives the ratio between the tensile and compressive strength of any type of masonry.

$$0.03 f_m \leq f_t \leq 0.09 f_m \quad (3.2)$$

Internal friction and dilatation angle: The internal friction angle is a measure of the ability of the material to withstand the shear stress. Definition of the internal friction angle is derived from Mohr's Circle.

On the other hand, dilatation angle limits the amount of residual volumetric strain which occurs during plastic shearing and it is considered as constant during plastic yielding.

In the numerical modeling stage, internal friction angle for clay bricks is taken as 30 – 40° (Kawa et al. 2008) whereas for stone masonry units as 10 – 22.4° (Vasconcelos et al. 2009) When the internal friction angle is not given in the referred experimental study.

Furthermore, dilatation angle of masonry has not been provided in any of the considered experimental studies. It is taken as 10° (Choudhury et al. 2015).

Elasticity modulus: Elastic modulus of masonry has been provided in most of the referred experimental studies. For the ones in which elasticity modulus of masonry is not given, below equation (Kaushik et al. 2007) is used.

$$E_m = 250 \sim 1100 * f_m \quad (3.3)$$

Poisson's ratio: For the experimental studies in which Poisson's ratio of masonry (ν_m) is not given, its value is taken as 0.2 (Mosalam et al. 2009).

Relation between brick and mortar strength: In some of the studies, compressive strengths of mortar and brick are given separately. In order to obtain the compressive strength of masonry, provisions given in Eurocode 6 (2005) is used. Following equation is used:

$$f'_m = K f'_b{}^\alpha * f'_j{}^\beta \quad (3.4)$$

where β , α and K are constants based on experimental studies to determine the compressive strength of masonry. f'_b , f'_j and f'_m are the compressive strengths of brick unit, mortar and masonry respectively. Kaushik et al. (2007) recommends these constants as 0.32, 0.49, 0.32 respectively.

3.3. Nonlinear Pushover Analysis of Prototype URM Walls

In order to determine ultimate in-plane lateral load capacities of the prototype URM walls with simplified macro modeling techniques, nonlinear static pushover analysis is used in this section. Six of the selected experimental studies are modeled using SAP2000 and ultimate load capacities are obtained. Each selected experimental study belongs to one of the six prototype URM walls with different perforation geometry, which have been introduced in Section 2.2. Considering the aim of numerical analysis, important issue to determine the closest match for the ultimate lateral loads compared to experimental results.

3.3.1. Nonlinear Modeling Strategy

Six nonlinear numerical models are developed. Each model supersedes an experimental study which is categorized according to perforation geometry of masonry walls as described in Chapter 2. For each type of masonry wall, one numerical model is developed.

Geometric and material properties of walls are taken from related experimental studies. Wall models are constituted by shell elements in SAP2000. The shell element is a type of area object that is used to model shell behavior in planar and three-dimensional structures. Material models of shell elements are defined in accordance with Section 3.2 for both linear and nonlinear parts. In order to determine stiffnesses of shell elements, a four-point numerical integration formulation is used. Stresses and internal forces and moments, in the element local coordinate system, are evaluated at the Gauss integration points and extrapolated to the joints of the elements. Pin restraints are introduced to model the bottom joints of the wall.

In all single wall experimental studies, test set-ups are constructed with a tie beam at the top of the walls and this rigid tie beam is supported along the length of the beam as presented in Figure 3.3.

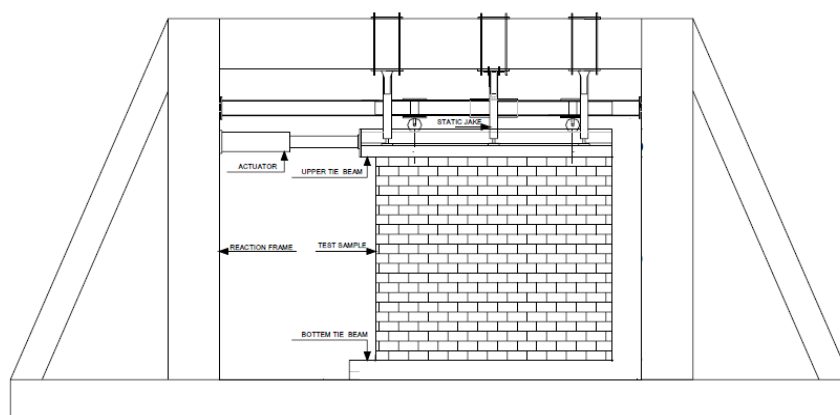


Figure 3.3. Masonry Wall Experimental Set-up

Therefore, in numerical models, top of the joints of the walls are grouped and diaphragm constrain is assigned to this group of joints. Thus, the elevation of all grouped joints will be kept as same during the horizontal drift of the wall. Furthermore, a rigid beam is introduced to the top of the walls in numerical models and if vertical load exists in the considered experimental study, assigned rigid frame also distributes the vertical load equally and prevents the stress localizations around the loaded joints. In addition to this vertical loading, self-weight of the masonry wall is automatically calculated by software.

Above diaphragm philosophy is not used for the full-scale experiments with shaking table test set-ups.

In this study, nonlinear static pushover analysis with displacement control is performed. In the pushover analysis, modeled structure is subjected to a gravity loading and a monotonic displacement-controlled lateral load pattern which continuously increases through elastic and inelastic behavior until an ultimate condition is reached. Displacements are monitored at the top right joint of masonry model in in-plane direction. Pushover analysis results are saved for multiple states in order to examine each step during the analysis.

3.3.2. Nonlinear Pushover Analysis Results

Analysis results are presented in this section. Nonlinear analysis results are presented as graphs and formed in terms of top displacement (mm) versus lateral force (kN).

In the following subsections, geometric properties related test set-up, loading information and material properties for each type of masonry walls are given based on the referred studies.

3.3.2.1. Nonlinear Pushover Analysis Results of Wall Model E1

Wall model E1 is based on Kalali and Kabir (2012). The tested wall is made with solid clay bricks. Brick dimensions are 105 x 50 x 28 mm. Compressive strength and elasticity modulus of the masonry are given as 3.89 MPa and 843 MPa, respectively.

For the rest of the unknown material properties, equations given in Section 3.2 are used. Tensile strength of masonry is taken as 0.35 MPa. Based on the workmanship quality, internal friction angle and dilatation angle are taken as 40° and 10°, respectively.

A gravity load of 41.2 kN is applied along the top of the masonry wall. 21.24 kN/m distributed load is assigned to top rigid frame of model.

Geometric dimensions and perforation properties of the wall model E1 are presented in Figure 3.4. In addition, the area IDs of the finite element mesh are presented in the same figure.

Nonlinear pushover model analysis is performed. Figure 3.5 presents the comparison of top displacement versus lateral force curve with the experimental capacity curve.

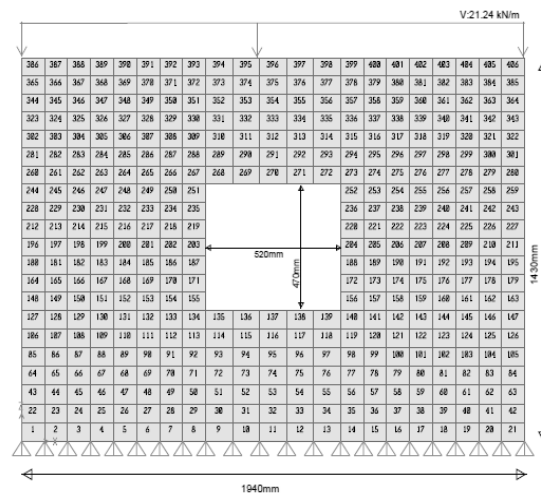


Figure 3.4. Wall Model E1 Geometric Properties

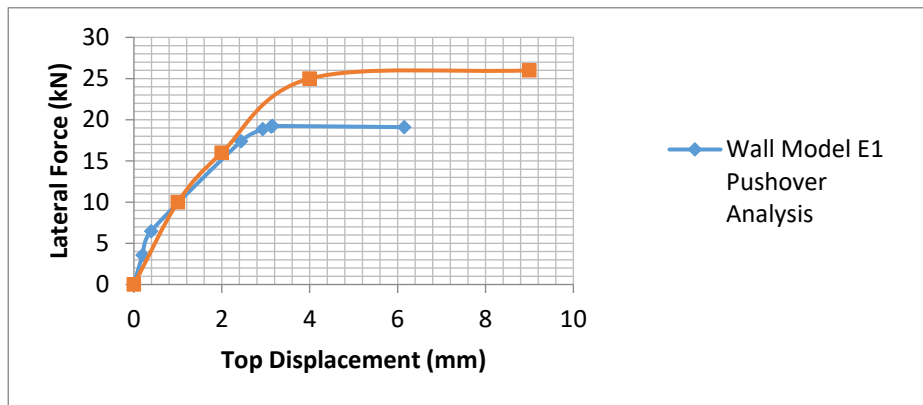


Figure 3.5. Wall Model E1 Nonlinear Analysis Results

Ultimate lateral force is determined as 19.1 kN with an ultimate roof displacement of 6mm whereas in the experimental study, ultimate force is 26.1 kN with an ultimate roof displacement of 9 mm. As a result, both experimental and nonlinear study give relatively close results on comparable grounds in terms of ultimate strength and displacement.

3.3.2.2. Nonlinear Pushover Analysis Results of Wall Model E2

Wall model E2 is based on Formica et al. (2002). The tested wall is made with clay bricks. Bricks have 120 mm thickness. Tensile strength and internal friction angle of the masonry are given as 0.4 MPa and 30°, respectively. For the rest of the unknown material properties, equations given in Section 3.2 are used. Compressive strength of masonry is taken as 3.33 MPa. Elasticity modulus is taken as 2500 MPa and dilatation angle is taken as 10°.

A gravity load of 37 kN is applied along the top of the masonry wall. 18 kN/m distributed load is assigned to the top rigid frame of model.

Geometric dimensions and perforation properties of the wall model E2 are presented in Figure 3.6. In addition, the area IDs of the finite element mesh are presented in the same figure.

Nonlinear pushover model analysis is performed. Figure 3.7 presents the comparison of top displacement versus lateral force curve.

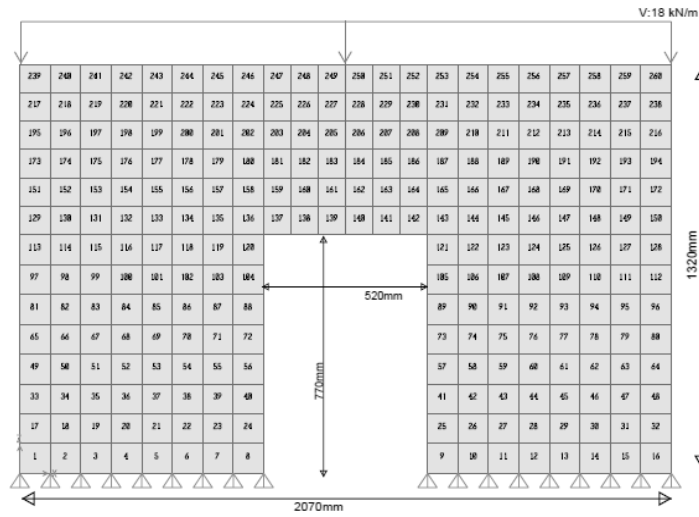


Figure 3.6. Wall Model E2 Geometric Properties

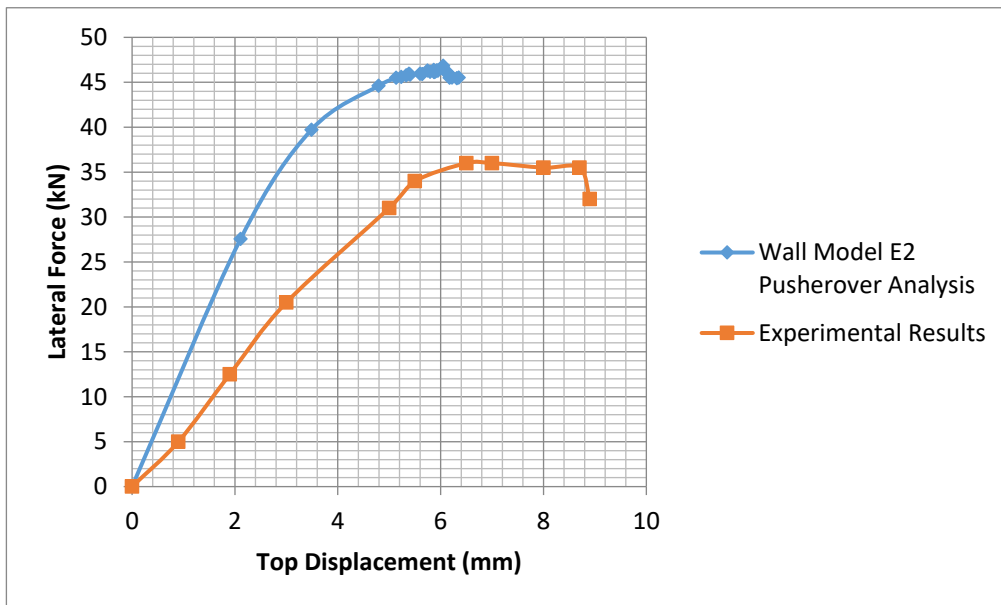


Figure 3.7. Wall Model E2 Nonlinear Analysis Results

Ultimate lateral force is determined as 36 kN with a roof displacement of 9 mm whereas in the experimental study, ultimate force is 45.5 kN with a roof displacement of 6.5 mm. Based on the equations given in Section 3.2, elasticity modulus and compressive strength of masonry are estimated by using an iterative procedure in order to obtain closer results to experimental studies. However, according to the Figure 3.7, calculated results are different from the experimental studies especially for the initial slopes of the curves due to the estimated material properties.

3.3.2.3. Nonlinear Pushover Analysis Results of Wall Model E3

Wall model E3 is based on Paquette and Bruneau (2006). The tested wall is made of stone masonry units with a low strength mortar. Thickness of the bricks is 190 mm. Compressive strength of brick and mortar are given as 109 MPa and 9.24 MPa, respectively. The tensile strength of the masonry is given as 0.18 MPa. From Equation 3.4, compressive strength of masonry is calculated as 12.78 MPa. For the rest of the unknown material properties, equations given in Section 3.2 are used. Internal friction angle, dilatation angle and modulus of elasticity are taken as 15°, 10° and 5550 MPa, respectively.

A gravity load of 26 kN is applied to the experimental set-up of the masonry wall. A distributed load of 6.37 kN/m is assigned to the top rigid frame of model.

Geometrical dimensions and perforation properties of the wall model E3 are presented in Figure 3.8. In addition, the area IDs of the finite element mesh are presented in the same figure.

Nonlinear pushover model analysis is performed. Figure 3.9 presents the comparison of top displacement versus lateral force curve.

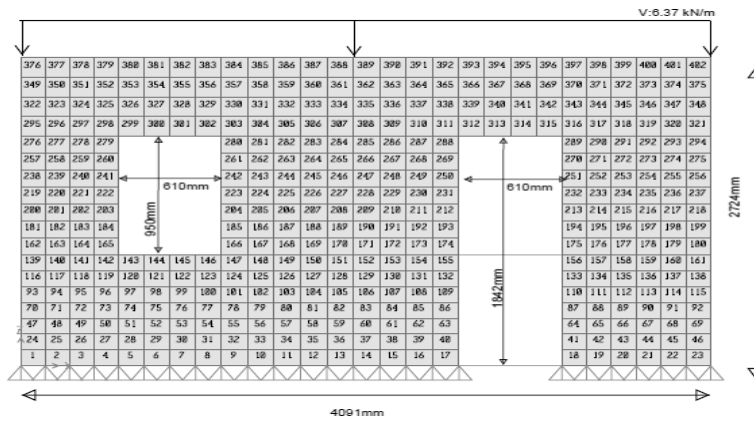


Figure 3.8. Wall Model E3 Geometric Properties

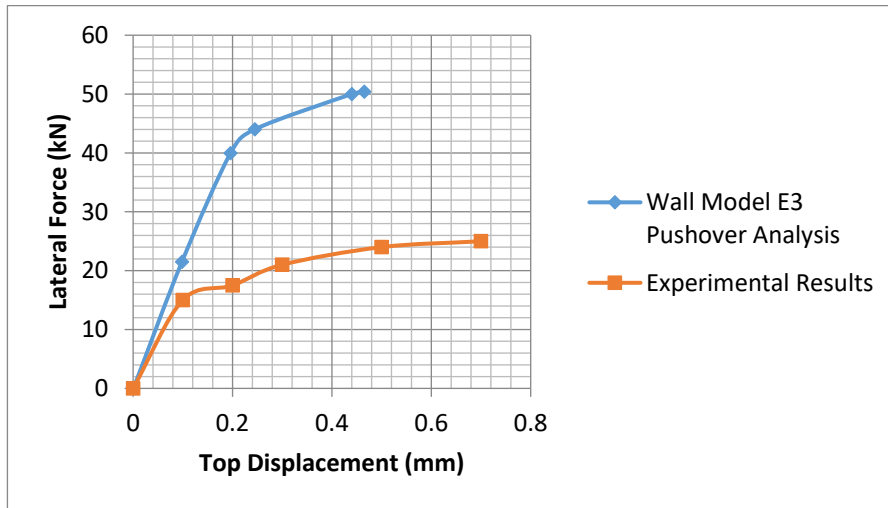


Figure 3.9. Wall Model E3 Nonlinear Analysis Results

Ultimate lateral force of the nonlinear wall model E3 is determined as 50 kN with a roof displacement of 0.5 mm whereas in the experimental study, ultimate force is 27 kN with a roof displacement of 0.7 mm. Unfortunately, experimental and nonlinear study results are not matching in this case. This difference is believed to occur from the gross assumptions about mechanical properties of the specimens as mentioned in Chapter 3.1 since it is very difficult to adopt the exact mechanical properties of masonry material.

3.3.2.4. Nonlinear Pushover Analysis Results of Wall Model E4

Wall model E4 is based on Abrams (1988). The tested wall is made of solid clay bricks. Thickness of the bricks is 245 mm. Compressive strength of bricks and mortar are given as 16 MPa and 1.5 MPa, respectively. From Equation 3.4, compressive strength of masonry is calculated as 2.79 MPa. For the rest of the unknown material properties, equations given in Chapter 3.2.1 are used. Internal friction angle, dilatation angle, tensile strength and modulus of elasticity are taken as 30°, 10°, 0.18 MPa and 1395 MPa, respectively.

A gravity load of 143 kN is applied to the experimental set-up of the masonry wall. A distributed load of 52 kN/m is assigned to the top rigid frame of model.

Geometrical dimensions and perforation properties of the wall model E4 are presented in Figure 3.10. In addition, the area IDs of the finite element mesh are presented in the same figure.

Nonlinear pushover model analysis is performed. Figure 3.11 presents the comparison of top displacement versus lateral force curve.

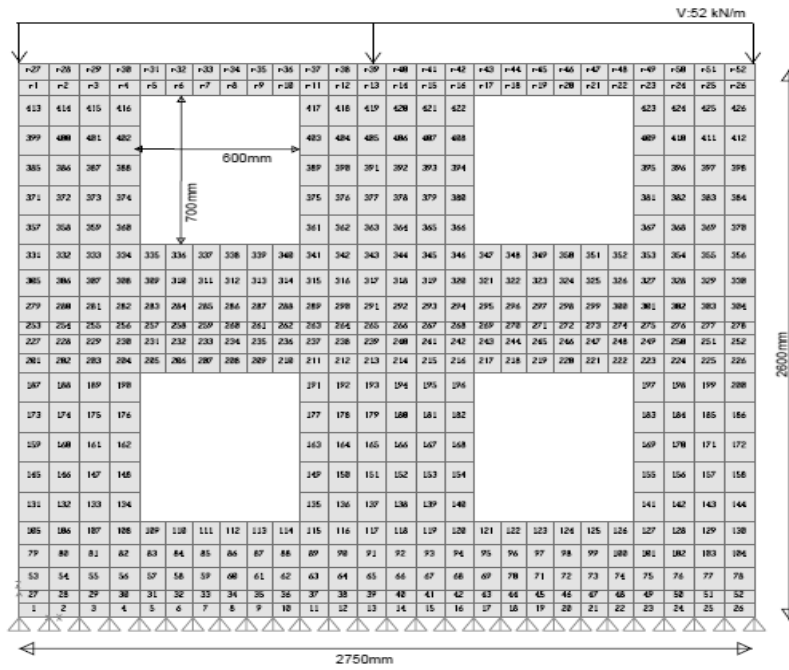


Figure 3.10. Wall Model E4 Geometric Properties

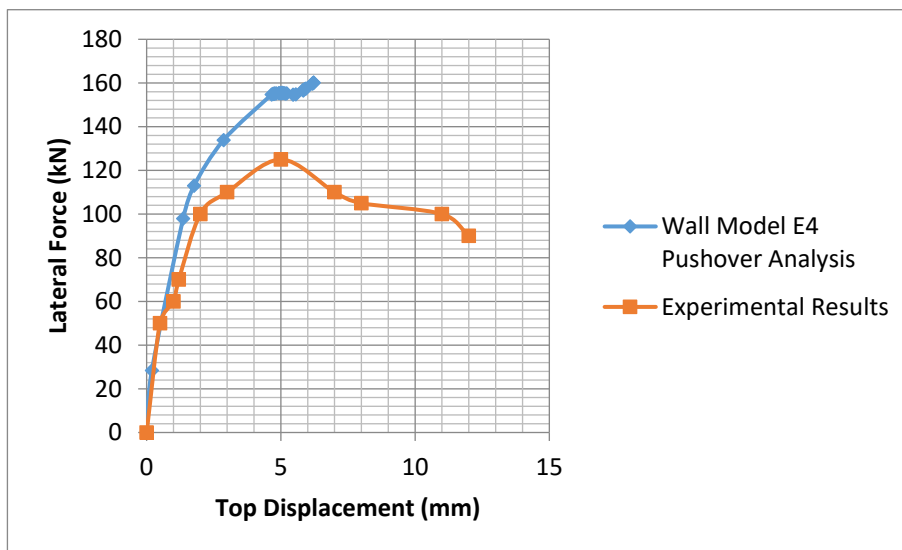


Figure 3.11. Wall Model E4 Nonlinear Analysis Results

According to Figure 3.11, nonlinear model results of wall model E4 gives an ultimate lateral force of 160 kN with a roof displacement of 7 mm whereas in the experimental study, ultimate force is determined as 125 kN with a roof displacement of 12.5 mm. As a result, numerical and experimental values do not have a good match for this case, especially for displacement capacity.

3.3.2.5. Nonlinear Pushover Analysis Results of Wall Model E5

Wall model E5 is based on Moon et al. (2007). The tested wall is made of solid clay bricks. Thickness of the bricks is 305 mm. Compressive strength of bricks and mortar are given as 42 MPa and 0.3 MPa, respectively. From Equation 3.4, compressive strength of masonry is calculated as 2.68 MPa. The modulus of elasticity for masonry is given as 8000 MPa. For the rest of the unknown material properties, equations given in Section 3.2 are used. Internal friction angle, dilatation angle and tensile strength are taken as 30°, 10° and 0.13 MPa, respectively.

There was no additional gravity load applied to experimental set-up. The wall is tested under its own self-weight.

Geometrical dimensions and perforation properties of the wall model E5 are presented in Figure 3.12. In addition, the area IDs of the finite element mesh are presented in the same figure.

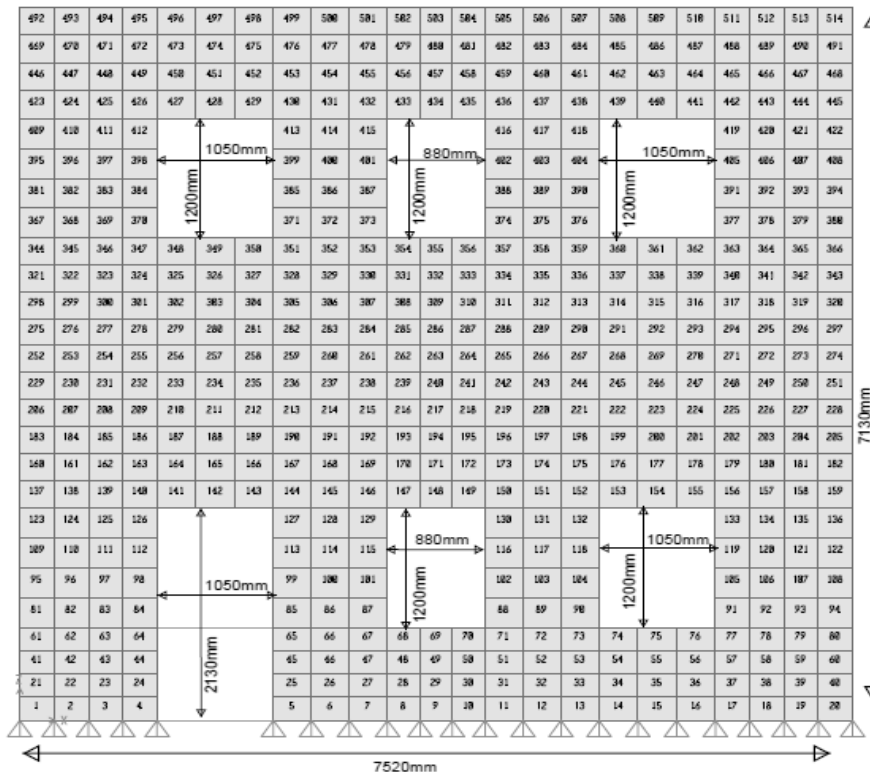


Figure 3.12. Wall Model E5 Geometric Properties

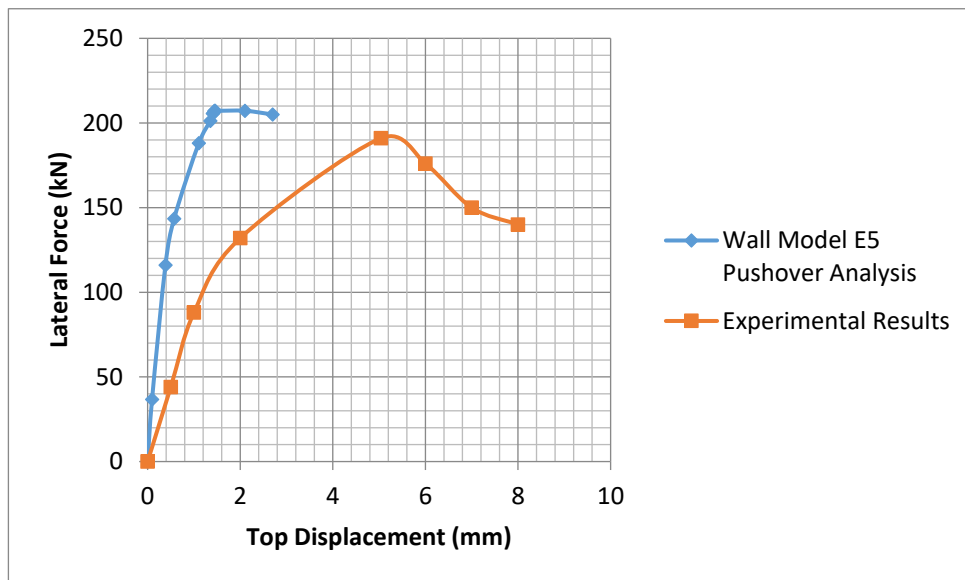


Figure 3.13. Wall Model E5 Nonlinear Analysis Results

According to Figure 3.13, nonlinear model results of wall model E5 gives an ultimate lateral force of 205 kN with a roof displacement of 3 mm whereas in the experimental study, ultimate force is determined as 191 kN with a roof displacement of 8 mm. Based on the equations given in Section 3.2, tensile strength and internal friction angle of masonry are estimated by using an iterative procedure in order to obtain closer results to experimental studies. However, according to the Figure 3.13, calculated results are different from the experimental studies for the initial slopes of the curves and top displacement values due to the estimated material properties. Although the ultimate strength values are close to each other.

3.3.2.6. Nonlinear Pushover Analysis Results of Wall Model E6

Wall model E6 is based on Nagethi and Alemi (2008). The tested wall is made of solid clay bricks. Thickness of the bricks is 205 mm. Compressive and tensile strength of masonry are given as 7.68 MPa and 0.183 MPa, respectively. For the rest of the unknown material properties, equations given in Section 3.2 are used. Internal friction angle, dilatation angle, and modulus of elasticity are taken as 40°, 10° and 1920 MPa, respectively.

Gravity load from the top of the wall was applied to experimental set-up. Therefore, 7 kN/m gravity load is distributed along to the rigid beam at the model.

Geometrical dimensions and perforation properties of the wall model E6 are presented in Figure 3.14. In addition, the area IDs of the finite element mesh are presented in the same figure.

Nonlinear pushover model analysis is performed. Figure 3.15 presents the comparison of top displacement versus lateral force curve.

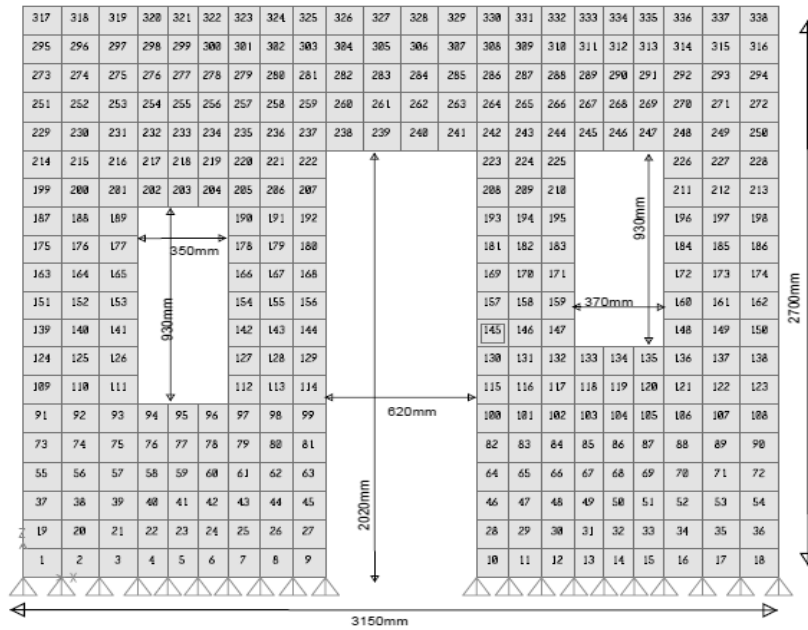


Figure 3.14. Wall Model E6 Geometric Properties

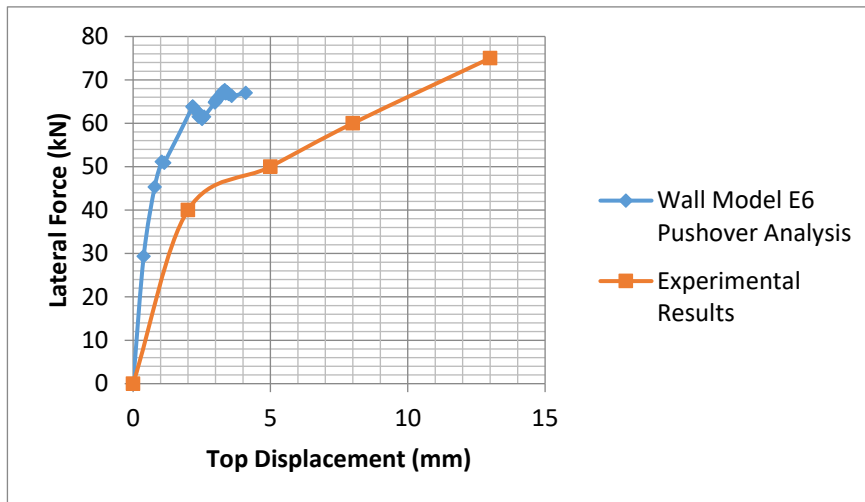


Figure 3.15. Wall Model E6 Nonlinear Analysis Results

According to the Figure 3.15, nonlinear model results of wall model E5 gives an ultimate lateral force of 67 kN with a roof displacement of 4.5 mm whereas in the experimental study, ultimate force is determined as 75 kN with a roof displacement of

13 mm. Based on the equations given in Section 3.2, elasticity modulus is estimated by using an iterative procedure in order to obtain closer results to experimental studies. However, according to the Figure 3.15, calculated results are different from the experimental studies especially for the initial slopes of the curves and top displacement due to the estimated material properties. Just like the previous case, the ultimate strength seems to be close, but the initial stiffness and ultimate capacity do not match well.

3.4. Ultimate Strength of URM Walls from Empirical Formulations

Lateral strength of URM walls is calculated in accordance with FEMA 273 (1997) and TBSC (2018). In addition to code formulae, empirical equation proposed by Akhaveissy (2013) is also employed for the determination of lateral strength of URM walls in this section. First the lateral strength capacity is calculated by using different approaches and then the obtained results are compared with each other and actual capacity values from real experimental studies that were presented in Section 2.4.

3.4.1. Collapse Mechanism of Perforated URM Walls

Strength capacity of perforated URM walls are performed by applying lateral load from the top of masonry walls. Then the shear force is distributed into each pier regarding to the relative rigidity. Moreover, capacities of walls are calculated with the consideration that they all have single story masonry walls which means that collapse of the system induced by the failure of all piers.

3.4.1.1. Calculation of Pier Stiffnesses

In order to calculate the in-plane stiffness of a perforated wall consisting of several connected piers, the most important parameter is the pier height. In this study, Dolce (1997) method is used to determine the effective height (h') as shown in Figure 3.16.

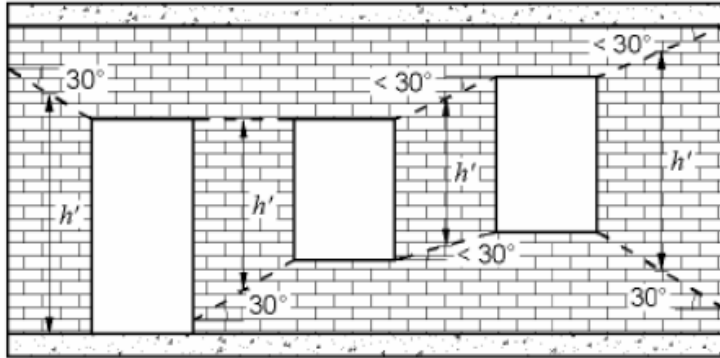


Figure 3.16. Determination of the Effective Height, h' (Dolce 1997)

After determination of effective height, in-plane stiffness of each pier (k) can be calculated with the Equation 3.5.

$$k = \frac{1}{\left[4 * \left(\frac{h'}{d} \right)^3 + 3 * \left(\frac{h'}{d} \right) \right]} \quad (3.5)$$

where:

h' = Effective height of the pier (m)

d = Length of the pier (m)

3.4.1.2. Collapse Mechanism of Different Wall Types

As mentioned before, six different experiments on masonry walls have been selected for detailed calculations. Each selected type of wall consists of different perforation patterns. Detailed expressions of perforation types are described in Figure 2.3.

Collapse mechanism of each wall type is presented in Figure 3.17. According to the number of piers of perforated URM walls, three different collapse mechanisms can be occurred as shown in Figure 3.17.

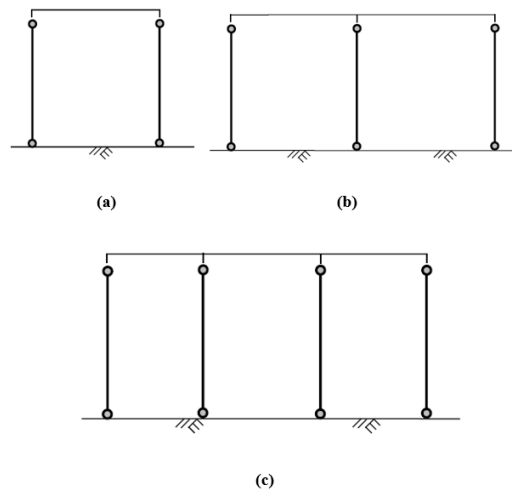


Figure 3.17. (a – c) Collapse Mechanism of Different Masonry Perforation Types

As a result, it is a safe assumption that the shear load on masonry walls is distributed into piers in accordance with their in-plane stiffness and resisted by these piers. Thus, when all piers have reached to their capacities, wall collapse can be expected. In this study, spandrel contributions in collapse mechanism or ultimate capacities are ignored and lateral strength of the wall is determined by the summation of the lateral strength of piers.

3.4.2. FEMA 273 Approach for Lateral Strength Calculation

NEHRP Guidelines for the Seismic Rehabilitation of Buildings FEMA 273, was released in 1997. The major aim of this standard is to develop a technical guideline for the seismic rehabilitation of the existing building or new elements that are added to existing structures. In Chapter 7 of FEMA 273, systematic rehabilitation of the masonry structures is introduced. In this section, lower bound lateral strength of perforated unreinforced masonry walls is calculated per Chapter 7 of FEMA 273.

In FEMA 273, lateral strength of the wall is determined in two steps as follows:

First step is titled as “Expected Lateral Strength”. This step is based on expected bed-joint sliding shear strength or expected rocking strength of walls. Equations 3.6 and 3.7 are given for two failure modes, respectively.

$$V_{bjs} = v_{me} * A_n \quad (3.6)$$

$$V_r = 0.9 * \alpha * P_{CE} * \left(\frac{L}{h_{eff}} \right) \quad (3.7)$$

where:

A_n = Area of net mortared/grouted section (mm^2),

h_{eff} = Height of resultant for lateral force (mm),

L = Length of wall or pier (mm),

P_{CE} = Expected vertical axial compressive force per Equation 3.8 (kN),

v_{me} = Expected bed-joint sliding shear strength per Equation 3.9 (MPa),

V_{bjs} = Lateral strength of wall or pier based on bed-joint shear strength (kN),

V_r = Lateral rocking strength of wall or pier (kN),

α = Factor due to end boundary conditions of wall. It can be taken as 0.5 for fixed-free cantilever wall and 1.0 for fixed-fixed pier condition.

$$P_{CE} = f_a * A_n \quad (3.8)$$

$$v_{me} = \frac{0.75 * \left(C + \frac{P_{CE}}{A_n} * \tan \varphi \right)}{1.5} \quad (3.9)$$

where:

f_a = Gravitational compressive force on masonry wall (MPa),

φ = Internal friction angle of mortar joints (in degrees).

Second step of the lateral strength determination method is called as “Lower Bound Lateral Strength”. With the help of this step, diagonal tension stress and flexural (toe

crushing) are calculated. Equations 3.10 and 3.11 are given for the mentioned two stresses respectively.

$$V_{dt} = v_{me} * A_n * \left(\frac{L}{h_{eff}} \right) * \sqrt{1 + \frac{f_a}{v_{me}}} \quad (3.10)$$

$$V_{tc} = \alpha * P_{CE} * \left(\frac{L}{h_{eff}} \right) * \left(1 - \frac{f_a}{0.7 * v_{me}} \right) \quad (3.11)$$

where, V_{dt} and V_{tc} defines the lateral strength of URM walls under diagonal tension and toe crushing failure modes, respectively.

If the lateral strength value calculated with the first step is less than the value calculated with second step, then the unreinforced masonry wall or pier can be considered as “*deformation controlled*” components. Otherwise, wall or pier can be considered as “*force controlled*” components.

Considering the above discussions, lateral strength capacities for the perforated URM walls used in the selected experimental studies are calculated by using Equations 3.6 – 3.11. Material properties of masonry brick and mortar joints are presented in Table 3.1 for all six types of masonry walls.

Based on material properties presented in Table 3.1, capacity calculations are performed and presented in Table 3.2. Detailed explanations and intermediate steps of calculations are presented in Figure C.1 in Appendix C.

Table 3.1. *Material Properties of Masonry*

Wall Type	Wall ID	Cohesion (C) (MPa)	Internal friction (θ)	Compressive strength (f_m) (MPa)	Tensile strength (f_t) (MPa)
1	E1	0.12	40	3.89	0.35
2	E2	0.12	30	3.33	0.40
3	E3	0.12	15	12.78	0.18
4	E4	0.25	30	2.79	0.18
5	E5	0.25	30	2.68	0.13
6	E6	0.25	40	7.68	0.18

Table 3.2. *Ultimate Lateral Load Capacities as per FEMA 273*

Wall Type	Wall ID	V_{bjs} (kN)	V_r (kN)	V_{dt} (kN)	V_{tc} (kN)
1	E1	17	12	24	10
2	E2	20	20	24	22
3	E3	35	6	33	7
4	E4	71	27	76	26
5	E5	179	8	139	8
6	E6	50	2	21	2

Results of ultimate load calculations presented in Table 3.2, following predominant lateral behavior of wall types can be listed as:

- Wall ID E1 – force controlled
- Wall ID E2 – deformation controlled
- Wall ID E3 – deformation controlled
- Wall ID E4 – force controlled
- Wall ID E5 – deformation controlled
- Wall ID E6 – deformation controlled

Since, experimental results for each wall specimens are determined in Chapter 2, failure modes are taken from these experimental results. Thus, ultimate strength

equations regarding to failure modes can be chosen by using these experimental results. Obtained failure modes from experimental results are listed as:

- Wall ID E1 – diagonal tension failure
- Wall ID E2 – diagonal tension failure
- Wall ID E3 – rocking failure
- Wall ID E4 – diagonal tension failure
- Wall ID E5 – sliding shear failure
- Wall ID E6 – sliding shear failure

3.4.3. TBSC (2018) Approach for Lateral Strength Calculation

New version of Turkish Building Seismic Code (TBSC 2018) was released on February 2018. Chapter 11 of TBSC 2018 is related with the seismic behavior of masonry structures.

TBSC 2018 also focuses on the shear capacity of the masonry walls and ultimate diagonal shear strength (f_{vk}) of wall or pier component of the URM walls as per Chapter 11.2.9 of TBSC 2018 (Equation 3.12).

$$f_{vk} = f_{vko} * 0.4\sigma \quad (3.12)$$

where:

f_{vk} = Characteristic shear capacity of masonry walls, considering the average axial stresses on the wall (MPa),

f_{vko} = Characteristic shear capacity of masonry walls, without considering the axial stresses (MPa),

σ = Vertical stress on wall or pier component (MPa).

To calculate the lateral strength of masonry component (V_{rm}), ultimate shear stress values should be multiplied with cross-sectional wall area which is under compressive stress as given in Equation 3.13.

$$V_{rm} = \tau_{em} * l_c \quad (3.13)$$

Length of the compressive part of masonry or pier component (l_c) is simply calculated as follows:

$$e_{cc} = M/N \quad (3.14)$$

where:

e_{cc} = Eccentricity of the masonry component (m).

M = Design moment induced by shear loading on masonry component (kNm).

N = Axial load perpendicular to shear loading on masonry component (kN).

In case of a small eccentricity ($e_{cc} \leq L/6$), length of compressive part of masonry component can be considered as total length of masonry component (Equation 3.15).

$$l_c = L \quad (3.15)$$

On the other hand, if there is a large eccentricity ($e_{cc} > L/6$), length of compressive part of masonry component can be calculated by Equation 3.16.

$$l_c = 3 * (L/2 - e_{cc}) \quad (3.16)$$

Small and large eccentricity cases are explained in Figures 3.18.

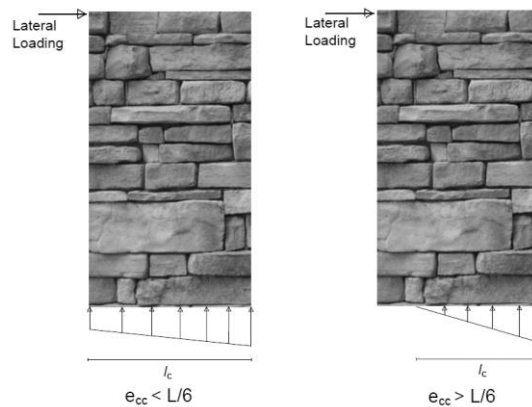


Figure 3.18. Compressive Areas of Masonry Components Under Different Eccentricity Levels

Considering the above discussions, lateral strength capacities for the perforated URM walls used in the selected experimental studies are calculated by using Equations 3.12 – 3.16. Material properties of masonry units and mortar joints are presented in Table 3.1 for each type of masonry walls. Calculated lateral strength calculations by using these material properties are presented in Table 3.3 per TBSC 2018.

Table 3.3. *Ultimate Lateral Load Capacities as per TBSC 2018*

Wall Type	1	2	3	4	5	6
Wall ID	E1	E2	E3	E4	E5	E6
V_{cr} (kN)	10.5	11.5	9	22.5	15	3

3.4.4. Lateral Strength Calculations by Akhaveissy (2013)

A distinguishing study has been proposed by Akhaveissy (2013) for the determination of in-plane limit state strength of masonry walls. Akhaveissy suggested a ratio regarding to masonry wall or pier component's height and its weight to predict the ultimate lateral load strength.

Study of the Akhaveissy is based on Mohr's circle theory. With the help of aspect ratio of the masonry component and the principal plane of Mohr's circle properties, shear resisting section of masonry component can be determined. By this means the height (x_{min}) related to contribution of the vertical mortar joints to the tensile strength can be obtained. Based on the upper-bound theorem, contribution due to the horizontal mortar joints to the shear strength can be determined assuming that the principal plane of Mohr's circle starts from load application point of masonry component (in our case, principal plane always from the top of the wall or pier component). Figure 3.19 presents an illustration of Akhaveissy's approach.

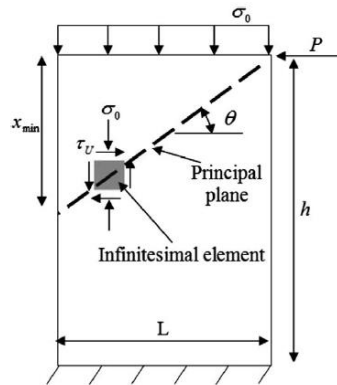


Figure 3.19. Stress Element on the Failure Surface and The Principle Plane

Equations for the ultimate strength of masonry components are presented as follows:

$$P = 0.88 * \alpha * P_u \quad (3.17)$$

$$P_u = \tau_u * L * t + F_t * t * x_{min} \quad (3.18)$$

where:

P = Ultimate lateral force that wall safely resist (kN),

α = Akhaveissy coefficient to consider different wall aspect ratios, failure pattern, staggered disposition of bricks, limited compressive strength of masonry unit (see Figure 3.19),

P_u = Resistant lateral force (kN),

x_{min} = Effective length of the wall (see Equation 3.19) (mm),

L = Length of wall or pier component (mm),

t = Thickness of wall or pier component (mm),

τ_u = Ultimate shear strength (MPa) (it can be calculated with the help of Mohr-Coulomb criterion – See Equation 3.20),

F_t = Tensile strength of mortar joints (MPa).

$$x_{min} = \min \left\{ \begin{array}{l} L * \tan \theta \\ (1 - \tan \theta) * h \end{array} \right. \quad (3.19)$$

where:

θ = The angle of principal plane (see Equation 3.20) (in degrees),

h = Height of wall or pier component (mm).

$$\theta = 0.5 * \tan^{-1} \left(2 * \tau_u / \sigma_n \right) \quad (3.20)$$

where:

σ_0 = Vertical stress on wall or pier component (MPa).

$$\tau_u = C + \sigma_0 * \tan \varphi \quad (3.21)$$

where:

C = Cohesion of the mortar joints (MPa),

φ = Friction angle of mortar joints (in degrees).

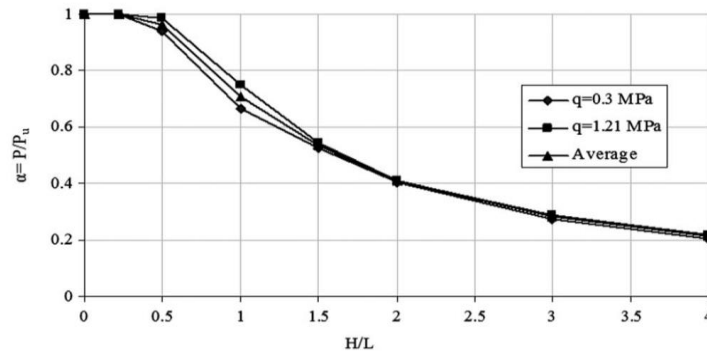


Figure 3.20. a Coefficient Curves Proposed by Akhaveissy (2013)

Considering the above discussions, lateral strength capacities for the perforated URM walls used in the selected experimental studies are calculated by using Equations 3.17 – 3.21. Material properties of masonry units and mortar joints are presented in Table 3.1 for all six types of masonry walls and lateral strength calculations as per Akhaveissy approach are presented in Table 3.4.

Table 3.4. *Ultimate Lateral Load Capacities as per Akhaveissy Approach*

Wall Type	Wall ID	τ_u (MPa)	X_{min} (mm)	P_u (kN)	P (kN)
1	E1	0.477	579	44	20
2	E2	0.207	577	66	29
3	E3	0.129	559	89	20
4	E4	0.372	542	165	84
5	E5	0.259	184	366	163
6	E6	0.279	260	109	35

Detailed explanations and intermediate steps of calculations for Akhaveissy equations are presented in Figure C.1 in Appendix C of the thesis.

3.4.5. Comparison of the Calculated Limit Strengths

In this section, the ultimate lateral strength values obtained by using the limit state approaches described in Sections 3.4.1–3.4.4, results from nonlinear analysis described in Section 3.3 and the ones from experimental studies are compared as presented in Table 3.5.

Table 3.5. *Comparison Table of Ultimate Lateral Loads as per Different Numerical Approaches, Experimental and Nonlinear Analysis Results (in kN)*

Wall Type	Wall ID	FEMA 273 (1997)	TBSC (2018)	Akhaveissy (2013)	Nonlinear Model Results	Experimental Study Results
1	E1	24	10.5	20	19	26
2	E2	24	11.5	29	36	46
3	E3	6	9	20	50	27
4	E4	76	22.5	84	160	125
5	E5	179	15	163	205	191
6	E6	50	3	35	67	75

The comparison of all the given values in Table 3.5 reveal that, ultimate lateral load capacities calculated with TBSC (2018) gives the most conservative results. On the other hand, ultimate lateral load capacities calculated with FEMA 273 and Akhaveissy give almost similar results for all wall types. Since TBSC limits the lateral strength by considering only the diagonal shear failure behavior, there is significant difference observed when other failure modes govern the wall.

3.5. Determination of Initial Crack Locations

The aim of this step is to estimate the initial crack locations of URM walls under in-plane lateral loads in terms of their perforation properties. For this purpose, six experimental studies are selected. Each selected experimental study belongs to one of the six perforation geometries that have been categorized in Chapter 2.

Since, this part of the study is not related with design of masonry walls, behavior of the walls is examined under ultimate loading conditions.

Linear elastic analysis is used in FE modeling of masonry walls. With the help of linear elastic modeling, the initial locations of cracks can be obtained by using failure criteria.

Selected experimental studies which are given in Chapter 2 are modeled with fine meshed shell elements considering their geometric and material properties. Ultimate lateral load acting on the specimen is applied to the numerical model with the addition of gravitational loads and its self-weight.

3.5.1. “Coulomb-Mohr” Failure Criterion

Among many well accepted failure criteria in literature, “Coulomb-Mohr or internal friction theory” is employed in this study with consideration of the masonry behavior. As described in Section 3.2, compression and tension strength of masonry are quite different from each other. Hence, “Coulomb-Mohr” theory can satisfy the requirements of actual masonry behavior.

According to Mohr-Coulomb theory, the ultimate shearing stresses are directly related with internal friction of material. If forces due to internal friction are considered as a function of nominal stresses on shear plane, the following equation between ultimate shear stress and nominal stress can be written.

$$\tau = \alpha\sigma + b \quad (3.22)$$

Constants “ a ” and “ b ” of the equation represent the material properties of masonry. Since masonry wall elements do not have any confinement, they can be considered in plane stress condition ($\sigma_3=0$) in out of plane direction. If the stress in direction-1 (σ_1) is under tensile stress and the stress in direction-2 (σ_2) is under compressive stress, then the maximum shear stress (τ) and the nominal stress (σ) can be obtain as:

$$\tau = \frac{\sigma_1 - \sigma_2}{2} \quad (3.23)$$

$$\sigma = \frac{\sigma_1 + \sigma_2}{2} \quad (3.24)$$

By substituting these equations into Equation (3.22), following equation can be constituted:

$$2b = \sigma_1(1 - a) + 2b = \sigma_2(1 + a) \quad (3.25)$$

Material constants can be evaluated by using the conditions below.

$$\sigma_1 = \sigma_u \text{ when } \sigma_2 = 0 \quad (3.26)$$

$$\sigma_2 = -\sigma_u' \text{ when } \sigma_1 = 0$$

In these conditions, tensile and compressive ultimate strength values of material are given as σ_u and σ_u' respectively. Then the conditions given in Equation (3.26) are substituted into Equation (3.25) to obtain:

$$\sigma_u(1 - a) = 2b \text{ and} \quad (3.27)$$

$$\sigma_u'(1 + a) = 2b$$

which leads to:

$$a = \frac{\sigma_u - \sigma_u'}{\sigma_u + \sigma_u'} \text{ and } b = \frac{\sigma_u \sigma_u'}{\sigma_u + \sigma_u'} \quad (3.28)$$

When above constants are substituted into Equation 3.28, the following expression which is valid for $\sigma_1 > 0$ and $\sigma_2 < 0$ can be obtained.

$$\frac{\sigma_1}{\sigma_u} - \frac{\sigma_2}{\sigma_u'} = 1 \quad (3.29)$$

where σ_1 and σ_2 have the same sign. Maximum of these stresses is the fracture stress and it is compared with the ultimate stress (σ_u or σ_u') of the material as follows:

$$\text{if } \sigma_1, \sigma_2 > 0, \max(\sigma_1; \sigma_2) = \sigma_u \text{ or } \frac{\max(\sigma_1; \sigma_2)}{\sigma_u} = 1 \quad (3.30)$$

$$\text{If } \sigma_1, \sigma_2 < 0, \min(\sigma_1; \sigma_2) = \sigma_u' \text{ or } \frac{\min(\sigma_1; \sigma_2)}{\sigma_u'} = 1 \quad (3.31)$$

As a result of above derivations, Coulomb-Mohr Failure Criteria can be expressed as in Figure 3.21:

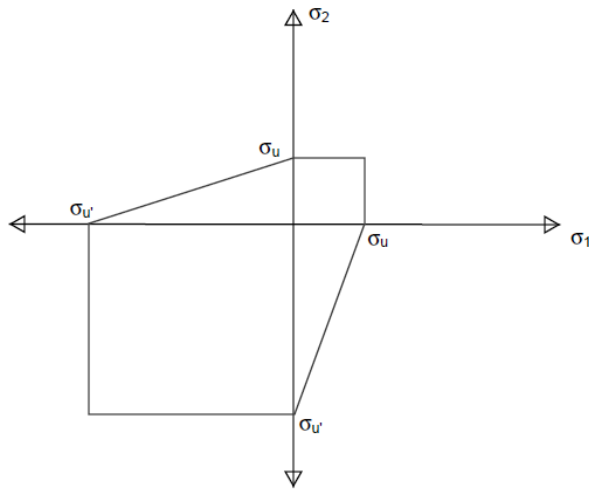


Figure 3.21. Coulomb-Mohr Failure Criteria

3.5.2. Linear Modeling Procedure and Details

Numerical models of the masonry walls are constituted by using of the SAP2000 software.

In the numerical modeling stage, following properties are taken from related experimental studies unless otherwise specified:

Geometric properties such as:

- Wall dimensions
- Wall perforation type and dimensions of openings
- Thickness of the walls

For loading properties:

- Self-weight of wall: it is automatically calculated by the software according to material unit weight and thickness of the walls.
- Gravity loading on wall (if any)
- Ultimate lateral load: Lateral load that causes the collapse of the walls are taken from the experimental studies. In some studies, cyclic lateral loading was applied. In such cases, irrespective of cyclic loading protocol used, lateral loads are applied to numerical models in a monolithical manner.

For material properties:

- Modulus of elasticity: In case of missing information, assumptions given in Section 3.2 are taken into account for modulus of elasticity of masonry.
- Unit weight of masonry: It is taken as 16–20 kN/m³ (Wijanto, 2007).
- Compressive and tensile strength of the wall: In cases where these values are not introduced, assumptions given in Section 3.2 are used.

Numerical models for each wall type are constituted with above properties in 2D Cartesian system (X-Z plane). Out of plane behavior is not considered in the scope of this thesis study.

In the single wall tests, a rigid beam (mostly constructed as reinforced concrete) is placed to the top of the wall in order to distribute the lateral load along the wall length and prevent local failures at the load application points. Therefore, in the numerical models, rigid frames are introduced at the top the wall. Thus, all external loads are applied to these numerical models as distributed line loads, which are assigned to rigid frames presented in Figure 3.22.

Moreover, in the experimental set-ups of single walls, rigid beams are supported vertically so that there will not be any differential vertical displacement along the wall during lateral loading. Therefore, a diaphragm constraint is assigned to the top joints of the wall in order to simulate this condition.

Determining the mesh size in modeling stage is an important procedure since it affects computational time and accuracy of the structural behavior. Using coarser meshes in the model can produce misleading results. Therefore, mesh refinement is necessary in order to obtain the results close to the real behavior. However, it should be optimized with consideration of the computational time. In this study, a very fine mesh size is used by taking into consideration the post processing procedure in Section 3.6. Therefore, even after two or three steps of mesh removal procedure, remaining model can still preserve stress distribution.

In addition to above conditions, in modeling of boundary conditions at the base, pin supports are assigned to models as shown in Figure 3.22 because out-of-plane behavior is not considered in this study and using fix or pin supports will not change the in-plane behavior of wall models.

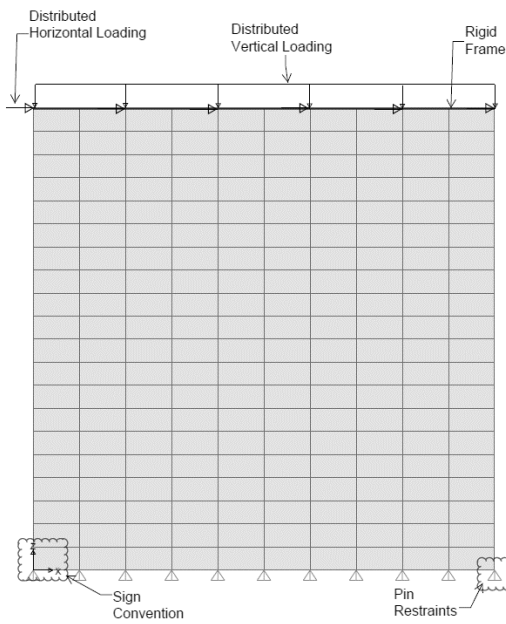


Figure 3.22. Typical Modeling Scheme and Boundary Details

Principal stress outputs of shell elements are exported from the model and Coulomb-Mohr stresses are calculated for each shell element based on the equations given in Section 3.5.1. The calculations are carried out by using Microsoft Excel spread sheets.

In these spread sheets, masonry wall views are constituted with using cells. Each cell in the Excel sheets represents the shell element in the related numerical model. Then, calculated Coulomb-Mohr stresses are normalized by ultimate material capacities for individual shells and printed into cells with related color categorization as shown in Table 3.6. This gives the stress distribution which reaches or exceeds the failure limits under certain lateral loading. In this study, the lateral loadings are equal to the ultimate load capacity of the wall.

Table 3.6. Stress Conditions and Color Categorization

Color Categorization	
PT, 0.54	Pure Tension. Failure is not expected
PT, 1.63	Pure Tension. Failure is expected
PC, 0.13	Pure Compression. Failure is not expected
PC, 0.13	Pure Compression. Failure is expected
CT, 0.12	Tension and Compression. Failure is not expected
CT, 1.11	Tension and Compression. Failure is expected

As seen in the Table 3.6, colored cells are categorized in six parts. Three of these parts represent the stress condition of related cell such as, “Pure Tension, Pure Compression and Tension/Compression”. The other three represent whether the shell element reaches its failure limit capacity, or it is still safe under its own stress condition. Moreover, stress ratio of each shell is written into the related cell.

In order to describe the stress conditions in Table 3.6 in a more direct manner, Figure 3.23 is given. In Figure 3.23, stress conditions are marked in the Coulomb- Mohr failure criterion graph referring to Figure 3.21.

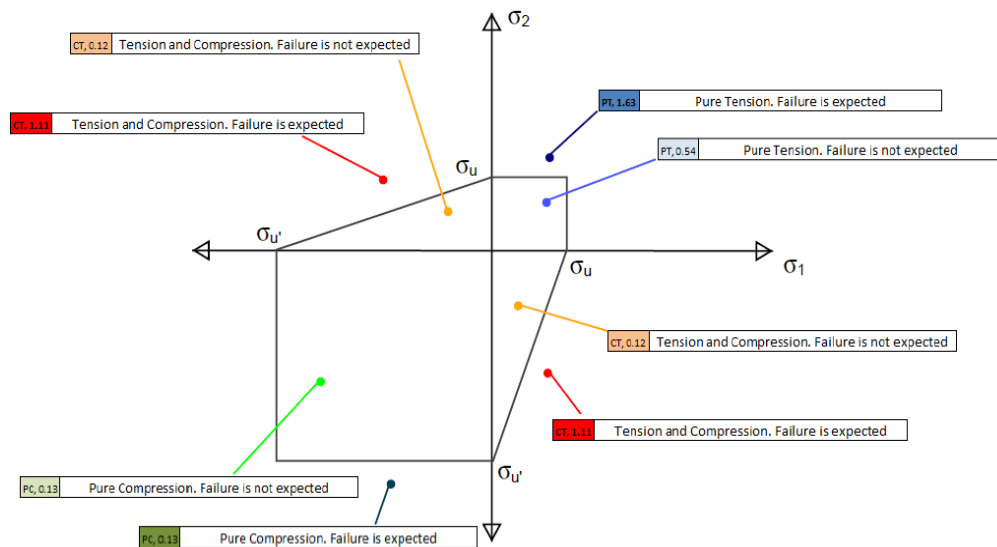


Figure 3.23. Coulomb-Mohr Failure Criteria with Stress Conditions

After determination of the stress distribution of the masonry wall, overstressed (failed) shell elements can be obtained, which gives the crack initializing points of the masonry wall.

3.5.3. Analysis Results of Linear Numerical Modeling

Numerical models created in SAP2000 have been constituted for six different masonry wall types. In this section static analysis results are presented for each type of wall.

3.5.3.1. Linear Analysis Results of Wall Model E1

Perforation geometry of wall model E1 consists of one window opening only. Material and geometric properties of the wall model that is used in the analysis are given in Section 3.3.2.1 of this study.

Loading protocol (Figure 3.24) of the experiment is given as follows:

Gravity load is given as 41.2 kN in the referred experimental study. This load is assigned to the numerical model as linearly distributed load along the top rigid beam as 21.24 kN/m.

After application of the gravity load, cyclic lateral loading is applied to the numerical model. At the load value 26.1 kN, collapse of the wall initiates. In the numerical modeling stage, ultimate load obtained from the experimental study is assigned to the model as linearly distributed load along the top rigid beam as 13.45 kN/m.

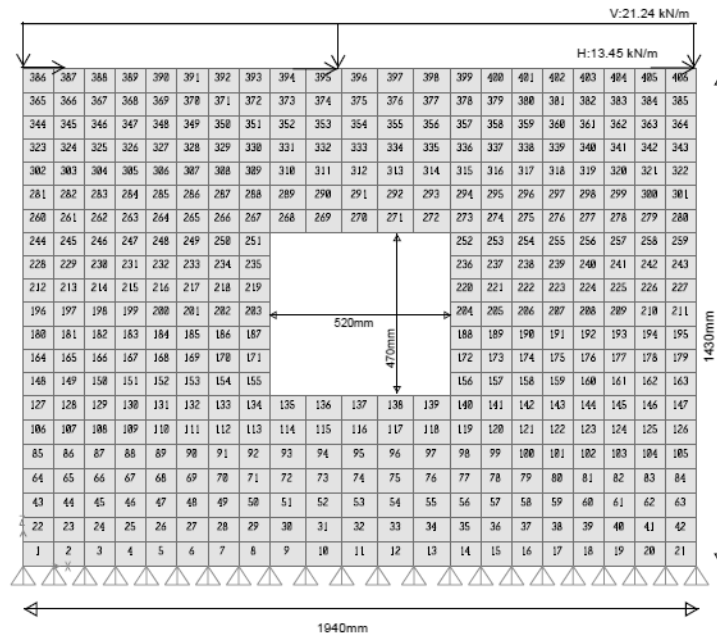


Figure 3.24. Wall Model E1

According to the analysis results, stress condition and distribution of the wall model E1 is calculated. Stress distribution diagram of the wall is presented in Figure 3.25. As it can be seen from the diagram, the strength limits have been exceeded at the cross corners of the opening which means, cracks of the wall have initiated from these corners under the given loading condition.

PC.046	PC.032	PC.025	PC.02	PC.016	CT.026	CT.046	CT.062	CT.076	CT.079	CT.076	CT.067	CT.057	CT.047	CT.038	CT.032	CT.028	CT.031	CT.041	CT.034	PC.14
PC.041	PC.033	PC.026	PC.02	PC.016	CT.028	CT.046	CT.065	CT.079	CT.084	CT.081	CT.074	CT.066	CT.058	CT.051	CT.044	CT.041	CT.041	CT.045	CT.037	CT.12
PC.037	PC.032	PC.023	CT.021	CT.023	CT.028	CT.047	CT.068	CT.083	CT.086	CT.082	CT.076	CT.067	CT.063	CT.055	CT.048	CT.043	CT.044	CT.045	CT.045	CT.10
PC.034	CT.033	CT.033	CT.037	CT.034	CT.034	CT.049	CT.077	CT.093	CT.093	CT.084	CT.077	CT.072	CT.064	CT.054	CT.043	CT.039	CT.04	CT.045	CT.054	CT.081
CT.032	CT.038	CT.047	CT.035	CT.057	CT.043	CT.054	CT.088	CT.100	CT.096	CT.084	CT.075	CT.069	CT.059	CT.049	CT.031	CT.027	CT.036	CT.041	CT.045	CT.062
CT.032	CT.042	CT.038	CT.074	CT.086	CT.086	CT.054	CT.117	CT.116	CT.095	CT.083	CT.072	CT.061	CT.046	CT.024	PC.018	CT.02	CT.033	CT.04	CT.039	CT.044
CT.03	CT.045	CT.067	CT.092	CT.111	CT.142	CT.136	CT.144	CT.1	CT.085	CT.074	CT.063	CT.049	PC.024	PC.024	PC.02	CT.021	CT.037	CT.042	CT.036	CT.028
CT.028	CT.047	CT.075	CT.102	CT.131	CT.157	CT.149	CT.140						PC.058	PC.032	PC.022	CT.035	CT.047	CT.047	CT.036	CT.017
CT.025	CT.049	CT.078	CT.109	CT.135	CT.157	CT.142							PC.041	CT.039	CT.045	CT.057	CT.061	CT.055	CT.038	CT.014
CT.023	CT.048	CT.079	CT.106	CT.128	CT.141	CT.124	CT.046						PC.03	CT.06	CT.077	CT.08	CT.076	CT.062	CT.041	CT.015
CT.019	CT.048	CT.073	CT.098	CT.111	CT.116	CT.086	CT.032						CT.03	CT.072	CT.1	CT.102	CT.089	CT.07	CT.044	CT.017
CT.017	CT.045	CT.069	CT.085	CT.092	CT.087	CT.067	CT.028						CT.033	CT.092	CT.122	CT.106	CT.099	CT.074	CT.040	CT.02
CT.015	CT.042	CT.061	CT.069	CT.067	CT.052	CT.036	CT.038						CT.049	CT.14	CT.137	CT.124	CT.102	CT.076	CT.047	CT.024
CT.015	CT.039	CT.052	CT.033	CT.042	PC.024	PC.028	PC.056						CT.209	CT.141	CT.142	CT.124	CT.141	CT.075	CT.047	CT.027
CT.024	CT.037	CT.045	CT.039	CT.022	PC.021	PC.026	PC.037	PC.039	CT.05	CT.062	CT.130	PC.273	CT.188	CT.141	CT.132	CT.143	CT.084	CT.07	CT.046	CT.029
CT.04	CT.038	CT.039	CT.031	PC.017	PC.02	PC.024	PC.03	CT.072	CT.075	CT.077	CT.134	CT.134	CT.142	CT.142	CT.140	CT.098	CT.083	CT.064	CT.044	CT.032
CT.057	CT.042	CT.038	CT.028	PC.016	PC.019	PC.023	CT.046	CT.08	CT.098	CT.184	CT.114	CT.100	CT.076	CT.074	CT.08	CT.077	CT.068	CT.055	CT.042	CT.034
CT.077	CT.048	CT.039	CT.032	CT.024	CT.026	CT.04	CT.062	CT.085	CT.1	CT.146	CT.140	CT.089	CT.065	CT.054	CT.056	CT.056	CT.051	CT.044	CT.057	CT.036
CT.097	CT.058	CT.042	CT.034	CT.032	CT.037	CT.05	CT.066	CT.083	CT.095	CT.180	CT.089	CT.083	CT.06	CT.045	CT.041	CT.038	CT.034	CT.03	PC.033	PC.038
CT.12	CT.068	CT.04	CT.032	CT.031	CT.037	CT.048	CT.061	CT.076	CT.088	CT.096	CT.094	CT.08	CT.059	CT.042	CT.031	CT.024	PC.022	PC.028	PC.035	PC.042
PC.131	CT.065	CT.033	CT.022	CT.021	CT.025	CT.035	CT.039	CT.067	CT.085	CT.090	CT.095	CT.081	CT.061	CT.041	CT.028	PC.017	PC.022	PC.027	PC.035	PC.040

Figure 3.25. Stress Distribution Diagram of Wall Model E1

3.5.3.2. Linear Analysis Results of Wall Model E2

Perforation geometry of wall model E2 consists of one door opening only. Material and geometric properties of the wall model E2 that is used in the analysis are given in Section 3.3.2.2 of this study.

Loading protocol (Figure 3.26) of the experiment is given as follows:

Gravity load is given as 37.25 kN in the referred experimental study. This load is assigned to the numerical model as linearly distributed load along the top rigid beam as 18 kN/m.

After application of gravity load, monolithic lateral loading is applied to the numerical model. At the load value 36.2 kN, collapse of the wall initiates. In the numerical modeling stage, ultimate load obtained from the experimental study is assigned to the model as linearly distributed load along the top rigid beam as 17.4 kN/m.

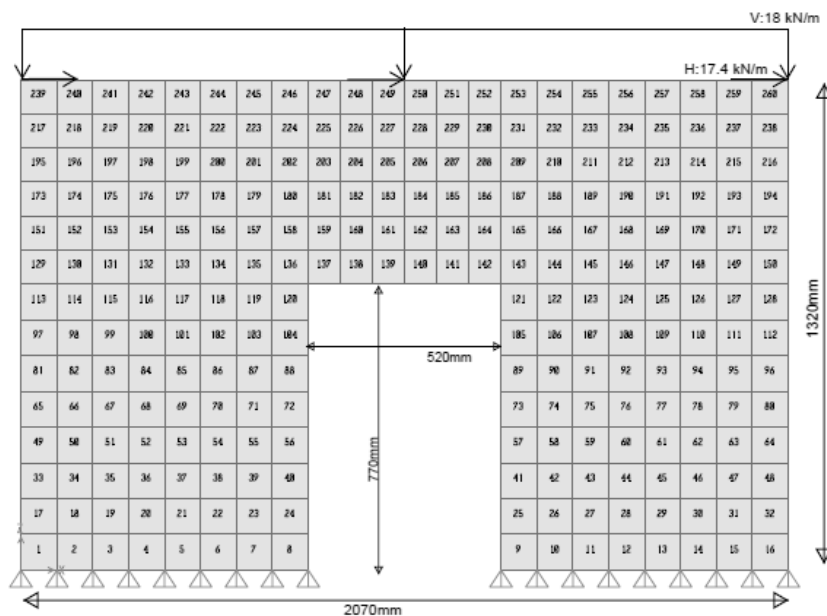


Figure 3.26. Wall Model E2

According to the analysis results, stress condition and distribution of the wall model E2 is calculated. Stress distribution diagram of the wall is presented in Figure 3.27. As it can be seen from the diagram, in top left corner of the wall and lowest left corners of the wall piers strength limits have been exceeded which means, cracks of the wall have initiated from these corners under given loading condition.

PC, 0.23	PC, 0.16	PC, 0.12	PC, 0.09	CT, 0.15	CT, 0.24	CT, 0.32	CT, 0.4	CT, 0.44	CT, 0.46	CT, 0.45	CT, 0.43	CT, 0.39	CT, 0.35	CT, 0.3	CT, 0.26	CT, 0.23	CT, 0.21	CT, 0.22	CT, 0.28	CT, 0.44	PT, 0.83	
PC, 0.19	PC, 0.16	PC, 0.12	CT, 0.11	CT, 0.17	CT, 0.24	CT, 0.34	CT, 0.42	CT, 0.47	CT, 0.49	CT, 0.48	CT, 0.46	CT, 0.43	CT, 0.4	CT, 0.36	CT, 0.32	CT, 0.29	CT, 0.26	CT, 0.27	CT, 0.3	CT, 0.43	CT, 0.64	
PC, 0.17	CT, 0.15	CT, 0.14	CT, 0.16	CT, 0.18	CT, 0.25	CT, 0.35	CT, 0.45	CT, 0.5	CT, 0.51	CT, 0.5	CT, 0.47	CT, 0.45	CT, 0.42	CT, 0.38	CT, 0.33	CT, 0.28	CT, 0.26	CT, 0.26	CT, 0.29	CT, 0.35	CT, 0.49	
CT, 0.16	CT, 0.16	CT, 0.2	CT, 0.22	CT, 0.24	CT, 0.25	CT, 0.38	CT, 0.5	CT, 0.57	CT, 0.56	CT, 0.52	CT, 0.48	CT, 0.45	CT, 0.42	CT, 0.37	CT, 0.29	CT, 0.24	CT, 0.2	CT, 0.23	CT, 0.25	CT, 0.27	CT, 0.37	
CT, 0.15	CT, 0.19	CT, 0.25	CT, 0.32	CT, 0.36	CT, 0.35	CT, 0.37	CT, 0.62	CT, 0.64	CT, 0.57	CT, 0.52	CT, 0.47	CT, 0.43	CT, 0.38	CT, 0.31	CT, 0.2	PC, 0.1	CT, 0.15	CT, 0.21	CT, 0.23	CT, 0.22	CT, 0.25	
CT, 0.14	CT, 0.21	CT, 0.32	CT, 0.43	CT, 0.51	CT, 0.59	PT, 0.75	CT, 0.76	CT, 0.59	CT, 0.52	CT, 0.46	CT, 0.42	CT, 0.37	CT, 0.31	CT, 0.19	PC, 0.14	PC, 0.11	CT, 0.17	CT, 0.24	CT, 0.25	CT, 0.2	CT, 0.15	
CT, 0.12	CT, 0.24	CT, 0.39	CT, 0.51	CT, 0.63	CT, 0.74	CT, 1.02	CT, 1.59								PC, 0.32	PC, 0.18	CT, 0.18	CT, 0.27	CT, 0.31	CT, 0.28	CT, 0.2	CT, 0.08
CT, 0.11	CT, 0.27	CT, 0.45	CT, 0.59	CT, 0.68	CT, 0.74	CT, 0.78	CT, 0.47								PC, 0.18	CT, 0.33	CT, 0.38	CT, 0.41	CT, 0.39	CT, 0.33	CT, 0.22	CT, 0.08
CT, 0.11	CT, 0.32	CT, 0.5	CT, 0.62	CT, 0.68	CT, 0.67	CT, 0.49	CT, 0.15								CT, 0.15	CT, 0.37	CT, 0.5	CT, 0.52	CT, 0.47	CT, 0.38	CT, 0.25	CT, 0.1
CT, 0.15	CT, 0.39	CT, 0.55	CT, 0.63	CT, 0.64	CT, 0.54	CT, 0.35	CT, 0.14								CT, 0.13	CT, 0.39	CT, 0.55	CT, 0.58	CT, 0.53	CT, 0.42	CT, 0.27	CT, 0.14
CT, 0.32	CT, 0.49	CT, 0.6	CT, 0.63	CT, 0.58	CT, 0.47	CT, 0.29	CT, 0.16								CT, 0.19	CT, 0.44	CT, 0.58	CT, 0.6	CT, 0.54	CT, 0.43	CT, 0.29	CT, 0.17
CT, 0.59	CT, 0.62	CT, 0.64	CT, 0.6	CT, 0.52	CT, 0.4	CT, 0.28	CT, 0.18								CT, 0.4	CT, 0.53	CT, 0.61	CT, 0.58	CT, 0.51	CT, 0.43	CT, 0.3	CT, 0.2
CT, 0.92	CT, 0.78	CT, 0.64	CT, 0.54	CT, 0.43	CT, 0.32	CT, 0.23	CT, 0.23								CT, 0.74	CT, 0.67	CT, 0.59	CT, 0.52	CT, 0.43	CT, 0.34	CT, 0.26	CT, 0.25
PT, 1.38	CT, 0.79	CT, 0.58	CT, 0.45	CT, 0.34	CT, 0.23	PC, 0.19	PC, 0.29								PT, 1.21	CT, 0.67	CT, 0.51	CT, 0.42	CT, 0.34	CT, 0.24	PC, 0.22	PC, 0.32

Figure 3.27. Stress Distribution Diagram of Wall Model E2

3.5.3.3. Linear Analysis Results of Wall Model E3

Perforation geometry of wall model E3 consists of one door and one window opening. Material and geometric properties of the wall model E3 that is used in the analysis are given in Section 3.3.2.3 of this study.

Loading protocol (Figure 3.28) of the experiment is given as follows:

Gravity load is given as 26 kN in the referred experimental study. This load is assigned to the numerical model as linearly distributed load along the top rigid beam as 6.37 kN/m.

After application of gravity load, cyclic lateral loading is applied to the numerical model. At the load value 27 kN, collapse of the wall initiates. In the numerical

modeling stage, ultimate load obtained from the experimental study is assigned to the model as linearly distributed load along the top rigid beam as 6.6 kN/m.

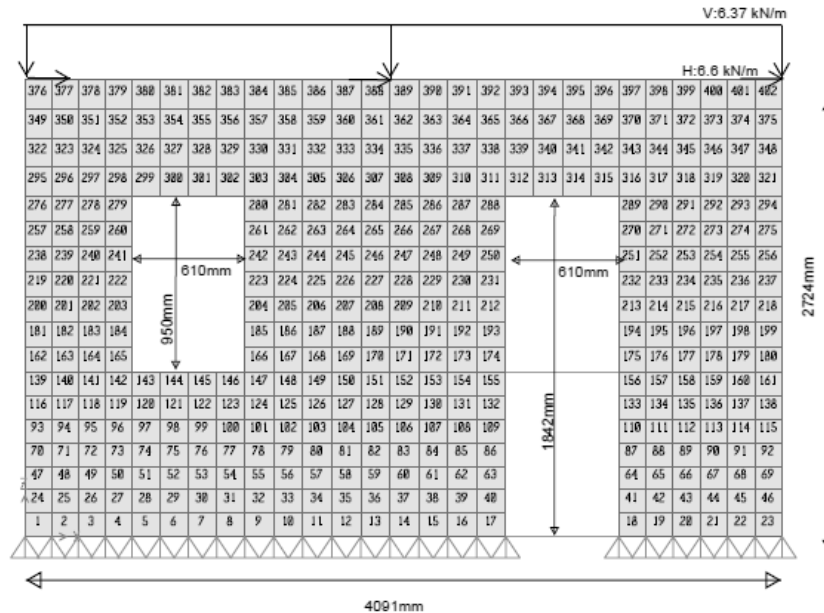


Figure 3.28. Wall Model E3

According to the analysis results, stress condition and distribution of the wall model E3 is calculated. Stress distribution diagram of the wall is presented in Figure 3.29. As it can be seen from the diagram, in cross corners of the window opening and rigid beam connection at right corner of the wall strength limits have been exceeded. In addition, middle pier of the wall has almost reached its strength limit in diagonal direction. Since the linear analysis method is employed, stresses propagate without considering the nonlinear behavior of the nodes of the shell elements. That means, after failing of the first shell element, stress propagation can be fully changed. Because of this reason, it is not completely correct to state that “all shells that have exceeded their strength limits are cracked.” Instead, it will be more accurate to state that “cracks initiate from the shell elements with maximum stress”.

PC,0.02	PC,0.01	PC,0.01	CT,0.06	CT,0.19	CT,0.27	CT,0.25	CT,0.2	CT,0.11	CT,0.06	CT,0.03	CT,0.05	CT,0.11	CT,0.19	CT,0.31	CT,0.44	CT,0.53	CT,0.54	CT,0.48	CT,0.36	CT,0.24	CT,0.19	CT,0.07	CT,0.04	CT,0.07	PT,0.24	PT,0.55
PC,0.02	PC,0.01	PC,0.01	CT,0.06	CT,0.24	CT,0.32	CT,0.32	CT,0.23	CT,0.15	CT,0.07	CT,0.03	CT,0.07	CT,0.15	CT,0.23	CT,0.32	CT,0.45	CT,0.57	CT,0.59	CT,0.52	CT,0.42	CT,0.28	CT,0.19	CT,0.31	CT,0.06	CT,0.06	CT,0.22	CT,0.49
CT,0.02	CT,0.04	CT,0.04	CT,0.34	CT,0.35	CT,0.43	CT,0.31	CT,0.24	CT,0.05	PC,0.01	PC,0.01	CT,0.09	CT,0.19	CT,0.28	CT,0.35	PT,0.47	CT,0.62	CT,0.69	CT,0.59	CT,0.36	CT,0.27	CT,0.11	PC,0.01	PC,0.01	CT,0.03	CT,0.18	CT,0.44
CT,0.04	CT,0.11	CT,0.23	PT,0.48	PT,0.85	CT,0.24	CT,0.18	CT,0.05	PC,0.02	PC,0.01	PC,0.01	CT,0.14	CT,0.27	CT,0.36	CT,0.45	PT,0.55	PT,0.86	PT,1.13	CT,0.26	CT,0.16	CT,0.06	PC,0.02	PC,0.01	PC,0.01	CT,0.01	CT,0.15	CT,0.28
CT,0.05	CT,0.17	CT,0.35	CT,0.78					PC,0.03	PC,0.01	CT,0.09	CT,0.25	CT,0.36	CT,0.46	CT,0.55	CT,0.67	PT,1.27					PC,0.02	PC,0.01	PC,0.01	CT,0.04	CT,0.13	CT,0.31
CT,0.05	CT,0.19	CT,0.32	CT,0.16					CT,0.05	CT,0.1	CT,0.24	CT,0.36	CT,0.45	CT,0.52	CT,0.58	CT,0.69	CT,0.59					CT,0.02	PC,0.01	CT,0.03	CT,0.08	CT,0.13	CT,0.22
CT,0.05	CT,0.19	CT,0.19	CT,0.07					CT,0.03	CT,0.21	CT,0.36	CT,0.46	CT,0.52	CT,0.55	CT,0.56	CT,0.47	CT,0.27					PC,0.01	CT,0.06	CT,0.09	CT,0.12	CT,0.13	CT,0.12
CT,0.06	CT,0.17	CT,0.15	CT,0.04					CT,0.06	CT,0.28	CT,0.47	CT,0.55	CT,0.56	CT,0.55	CT,0.48	CT,0.33	CT,0.11					CT,0.02	CT,0.07	CT,0.13	CT,0.15	CT,0.12	CT,0.03
CT,0.08	CT,0.15	CT,0.13	CT,0.03					CT,0.11	CT,0.4	CT,0.58	CT,0.6	CT,0.58	CT,0.51	CT,0.41	CT,0.24	CT,0.03					CT,0.02	CT,0.09	CT,0.15	CT,0.16	CT,0.12	CT,0.03
CT,0.13	CT,0.1	CT,0.05	CT,0.04					CT,0.29	CT,0.88	CT,0.66	CT,0.63	CT,0.56	CT,0.47	CT,0.34	CT,0.19	CT,0.04					CT,0.03	CT,0.1	CT,0.15	CT,0.16	CT,0.11	CT,0.03
CT,0.18	PC,0	PC,0.01	PC,0.02					CT,1.18	CT,0.78	CT,0.68	CT,0.6	CT,0.52	CT,0.42	CT,0.29	CT,0.15	CT,0.03					CT,0.04	CT,0.13	CT,0.17	CT,0.15	CT,0.1	CT,0.02
CT,0.2	PC,0	PC,0.01	PC,0.02	CT,0.07	CT,0.26	CT,0.58	PT,1.42	PT,0.97	CT,0.71	CT,0.61	CT,0.54	CT,0.46	CT,0.36	CT,0.24	CT,0.12	CT,0.03					CT,0.08	CT,0.15	CT,0.17	CT,0.14	CT,0.08	CT,0.02
CT,0.18	PC,0	PC,0.01	CT,0.11	CT,0.36	CT,0.47	CT,0.74	CT,0.77	PT,0.62	CT,0.53	CT,0.5	CT,0.45	CT,0.38	CT,0.3	CT,0.2	CT,0.1	CT,0.03					CT,0.08	CT,0.15	CT,0.17	CT,0.14	CT,0.08	CT,0.02
CT,0.15	CT,0.05	CT,0.13	CT,0.27	CT,0.42	CT,0.58	CT,0.64	CT,0.63	CT,0.5	CT,0.4	CT,0.38	CT,0.35	CT,0.3	CT,0.23	CT,0.15	CT,0.07	CT,0.03					CT,0.17	CT,0.18	CT,0.17	CT,0.13	CT,0.07	CT,0.03
PT,0.12	CT,0.09	CT,0.19	CT,0.31	CT,0.43	CT,0.52	CT,0.56	CT,0.53	CT,0.44	CT,0.34	CT,0.29	CT,0.26	CT,0.22	CT,0.17	CT,0.1	CT,0.05	CT,0.02					CT,0.28	CT,0.21	CT,0.17	CT,0.12	CT,0.06	CT,0.03
PT,0.16	CT,0.15	CT,0.23	CT,0.31	CT,0.39	CT,0.45	CT,0.48	CT,0.46	CT,0.39	CT,0.31	CT,0.24	CT,0.2	CT,0.15	CT,0.1	CT,0.05	CT,0.03	PC,0.02					CT,0.4	CT,0.24	CT,0.16	CT,0.09	CT,0.05	PC,0.02
CT,0.25	CT,0.22	CT,0.24	CT,0.29	CT,0.34	CT,0.39	CT,0.41	CT,0.4	CT,0.35	CT,0.28	CT,0.21	CT,0.15	CT,0.09	CT,0.04	PC,0.02	PC,0.02	PC,0.02					CT,0.54	CT,0.28	CT,0.13	CT,0.04	PC,0.02	PC,0.02
CT,0.4	CT,0.22	CT,0.21	CT,0.24	CT,0.29	CT,0.34	CT,0.38	CT,0.37	CT,0.33	CT,0.27	CT,0.19	CT,0.12	CT,0.05	PC,0.01	PC,0.02	PC,0.02	PC,0.02					PT,0.72	CT,0.25	CT,0.06	PC,0.01	PC,0.02	PC,0.02

Figure 3.29. Stress Distribution Diagram of Wall Model E3

3.5.3.4. Linear Analysis Results of Wall Model E4

Perforation geometry of wall model E4 consists of two window openings. Material and geometric properties of the wall model E4 that is used in the analysis are given in Section 3.3.2.4 of this study.

Loading protocol (Figure 3.30) of the experiment is given as follows:

Gravity load is given as 143 kN in the referred experimental study. This load is assigned to the numerical model as linearly distributed load along the top rigid beam as 52 kN/m.

After application of gravity load, cyclic lateral loading is applied to the numerical model. At the load value 120 kN, collapse of the wall initiates. In the numerical modeling stage, ultimate load obtained from experimental study is assigned to the model as linearly distributed load along the top rigid beam as 43.64 kN/m.

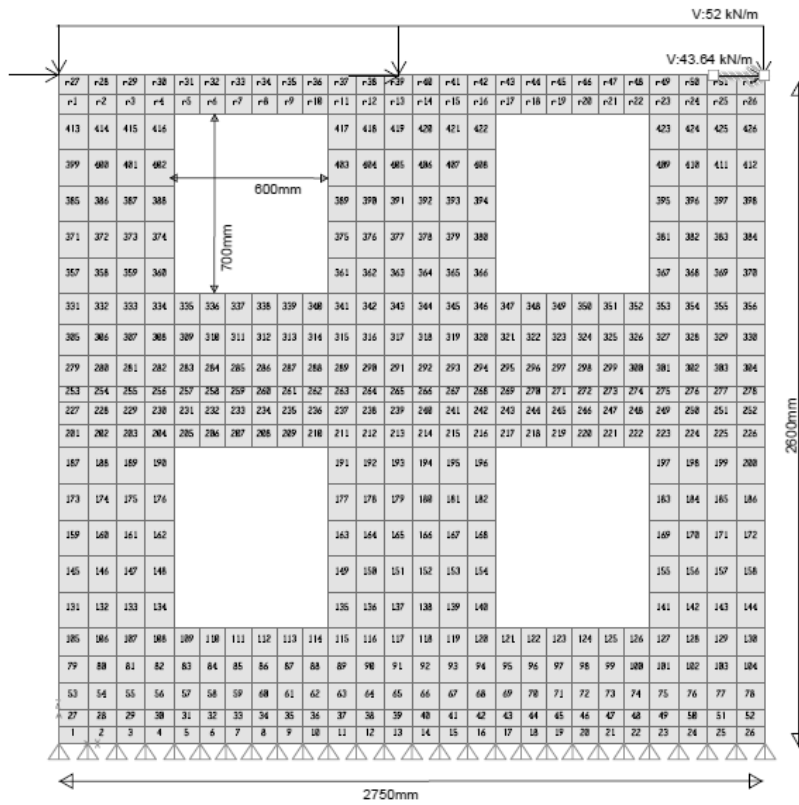


Figure 3.30. Wall Model E4

According to the analysis results, stress condition and distribution of the wall model E4 is calculated. Stress distribution diagram of the wall is presented in Figure 3.31. As it can be seen from the diagram, in cross corners of the opening's strength limits have been exceeded which means, cracks of the wall have initiated from these corners under given loading condition.

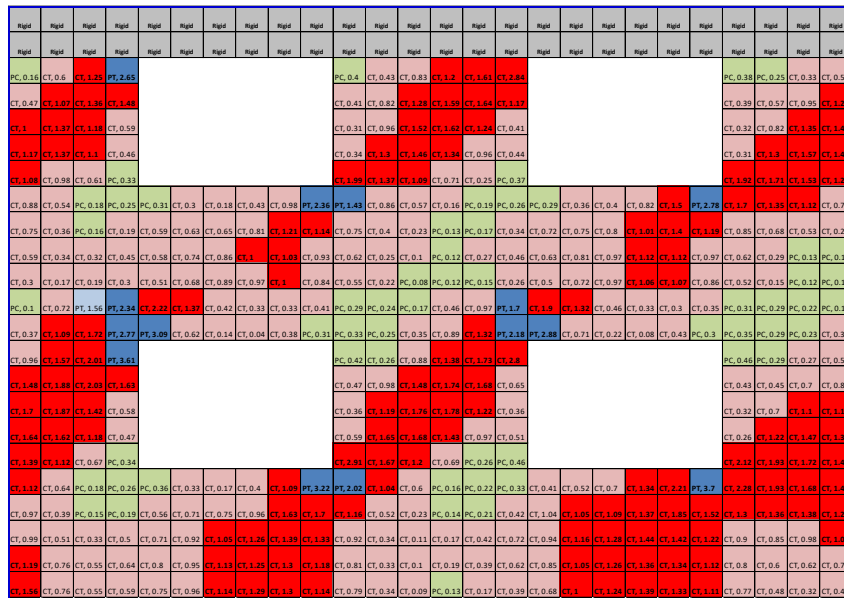


Figure 3.31. Stress Distribution Diagram of Wall Model E4

3.5.3.5. Linear Analysis Results of Wall Model E5

Perforation geometry of wall model E5 consists of three window openings. Material and geometric properties of the wall model E5 that is used in the analysis are given in Section 3.3.2.5 of this study.

Loading protocol (Figure 3.32) of the experiment is given as follows:

According to the experimental setup, there is no external gravitational load applied to the wall specimen.

In this considered study, experimental set-up is located on shake table. Cyclic lateral loading is applied to the test specimen. At the load value 191 kN, collapse of the wall initiates. In the numerical modeling stage, ultimate load obtained from the experimental study is distributed into two of the floor's rigid beams based on the assumption of equivalent earthquake load method.

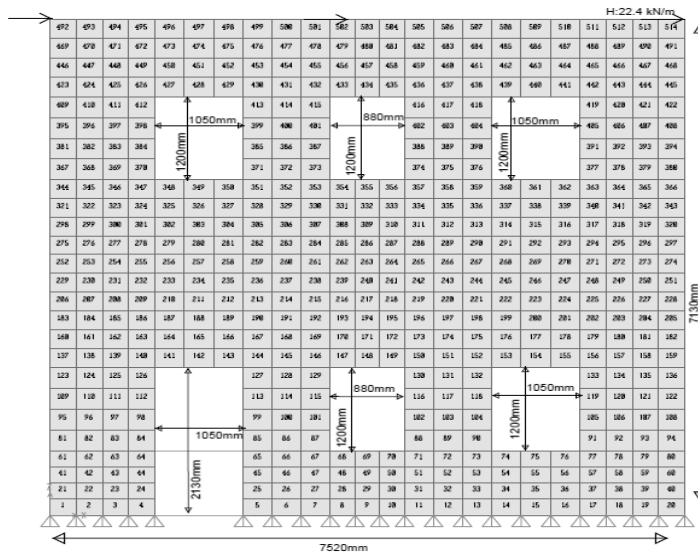


Figure 3.32. Wall Model E5

According to the analysis results, stress condition and distribution of the wall model E5 is calculated. Stress distribution diagram of the wall is presented in Figure 3.33. As it can be seen from the diagram, in cross corners of the openings and rigid beam connection at right corner of the wall strength limits have been exceeded which means, cracks of the wall have initiated from these corners under given loading condition.

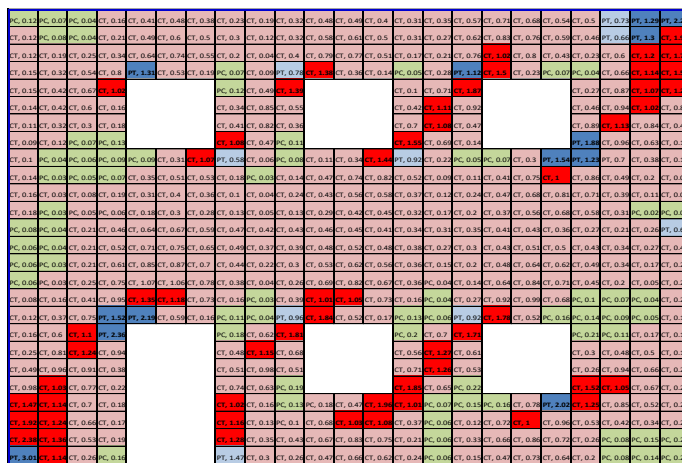


Figure 3.33. Stress Distribution Diagram of Wall Model E5

3.5.3.6. Linear Analysis Results of Wall Model E6

Perforation geometry of wall model E6 consists of one door and 2 window openings. Material and geometric properties of the wall model E6 that used in analysis are given in Section 3.3.2.6 of this study.

Loading protocol (Figure 3.34) of the experiment is given as follows:

Gravity load is given as 22 kN in the referred experimental study. This load is assigned to the numerical model as linearly distributed load along the top rigid beam as 7 kN/m.

Cyclic lateral loading is applied to the numerical model. At the load value 85 kN, collapse of the wall initiates. In the numerical modeling stage, ultimate load obtained from the experimental study is assigned to model as linearly distributed load along the top rigid beam as 24.4 kN/m.

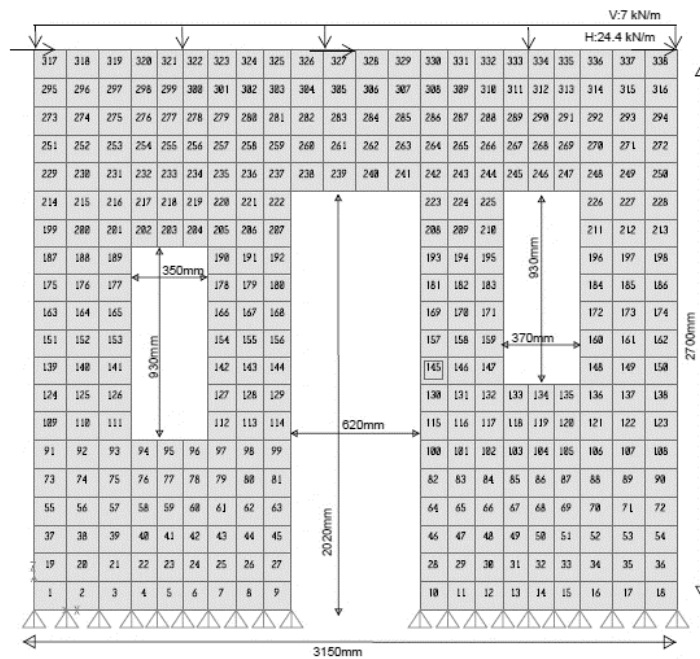


Figure 3.34. Wall Model E6

According to the analysis results, stress condition and distribution of the wall model E6 is calculated (Figure 3.35). Based on the stress distribution diagram, in cross corners of window openings and lowest left corners of the first and third piers strength limits have been exceeded. In addition, strength limits have also been exceeded at the rigid beam connection at right corner of the wall. Therefore, cracks are expected to initiate from those overstressed locations.

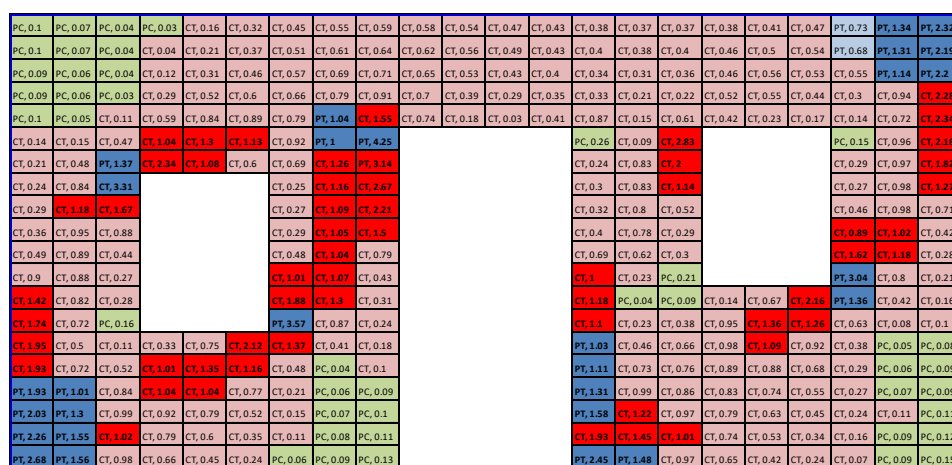


Figure 3.35. Stress Distribution Diagram of Wall Model E6

3.6. Crack Propagation Analysis

In this section, crack propagation of walls is utilized by using a post processing procedure. For this purpose, stress distributions and overstressed shell elements of the walls determined in Section 3.5 are used.

3.6.1. Post Processing Procedure

Before describing the post processing procedure, it would be best to remind that, since the linear analysis method is performed, stresses propagate without considering the nonlinear behavior at the nodes of the shell elements. This means that, after failure of the first shell element, stress propagation can be fully changed. Furthermore, the most

overstressed shell among its adjacent shell elements will be the first cracked one and after the cracking of the first shell element. Hence stress propagation can be again changed and the stress condition for the rest of the adjacent shells can be changed either. Because of these reasons, the closest crack propagation approach to the actual physical behavior of the specimen is removing of the most overstressed shell element and controlling the rest of the adjacent shells whether if they have exceeded their limits or not.

In accordance with Section 3.5, shell elements which have reached their strength limits are removed from the numerical wall model. This will give a new crack pattern for the masonry wall with the remaining shells. Then, under the same ultimate lateral loading, new wall model is analyzed which is different from classical pushover analysis.

By repeating the same procedure for at least two or three times successively, the crack propagation will be monitored in relation to the perforation pattern of masonry wall.

Proposed procedure resembles to the post-processing procedure given in most of the past research by Saloustros et al. (2017). However, in contrast to the general post-processing procedures, defined method is only used to specify the propagation of the cracks, not to determine the ultimate shear capacity of masonry wall. Thus, lateral loading on the numerical model remains constant in all the steps. Moreover, the level of the lateral load is also irrelevant in terms of the purpose of this analysis procedure. It is only a generic loading condition on the wall. The flow chart that represents the procedure is given in Figure 3.36.

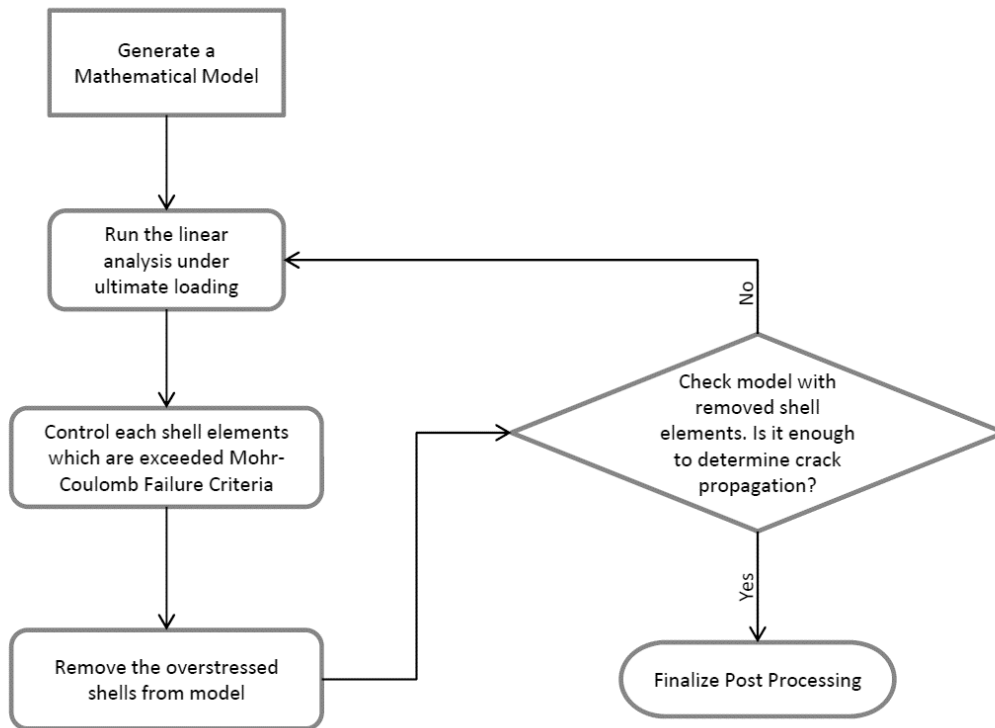


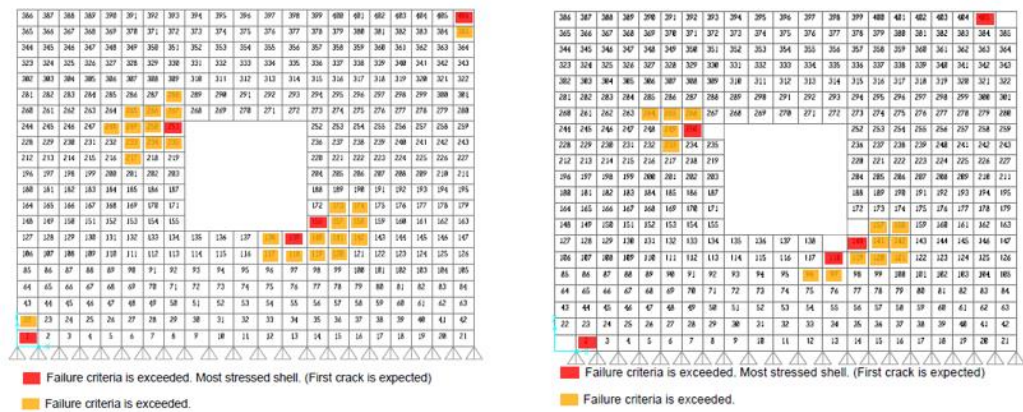
Figure 3.36. Flowchart of the Post Processing Procedure

3.6.2. Results of Post Processing Approach

Post processing approach consists of 6 different masonry wall types. As described in previous sections, same selected experimental studies are used in this part of the study.

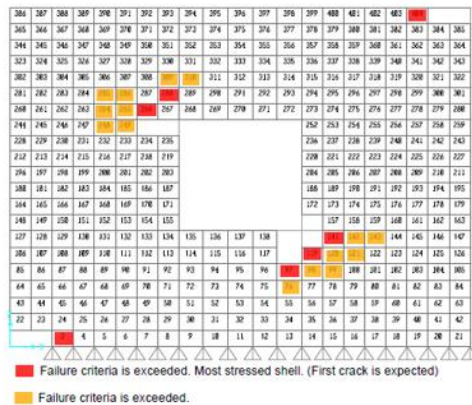
3.6.2.1. Wall Model E1

Crack pattern of the wall model E1 is determined in three steps of the post processing procedure. Stress distributions of each step are presented in Figures 3.37.a, 3.37b and 3.37c, respectively.



(a)

(b)



(c)

Figure 3.37. Post Processing Steps for Wall Model E1

After finalization of the three steps of post processing approach, crack pattern of the wall model E1 is determined. First cracks initiate at the cross corners of the window opening due to diagonal tension failure. Moreover, cracks also initiate at the top and bottom corners of the wall due to sliding shear failure. When further steps are utilized, cracks at the corners of the openings propagate diagonally towards the corners and the cracks at the edges of the wall propagate horizontally. Illustration of the crack pattern of the wall is presented in Figure 3.38. Expected crack pattern of the wall, matches with the pattern of the considered experimental study of Kalali and Kabir (2012).

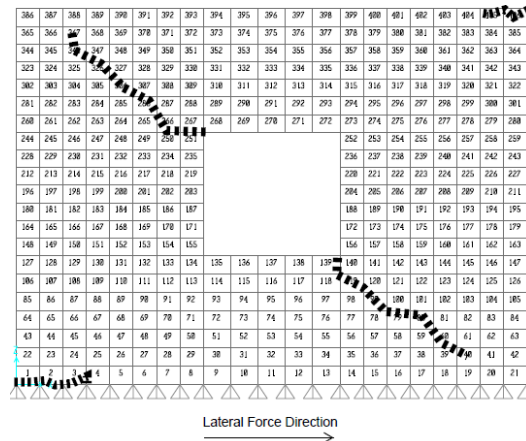


Figure 3.38. Expected Crack Pattern of Wall Model E1

3.6.2.2. Wall Model E2

Crack pattern of the wall model E2 is determined in three steps of post processing approach. Stress distributions of each step are presented in Figures 3.39a, 3.39b and 3.39c respectively.

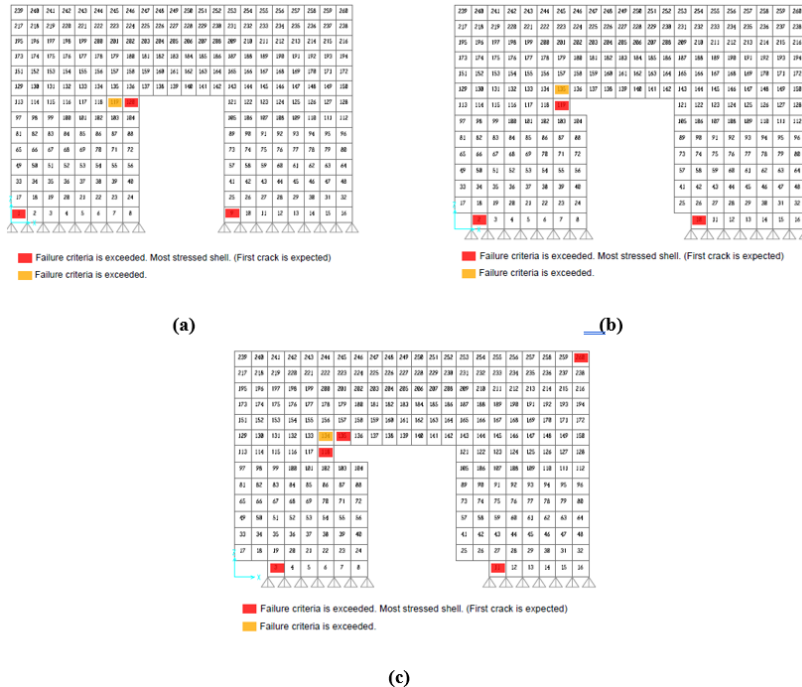


Figure 3.39. Post Processing Steps for Wall Model E2

First crack initiates at the corner of the door opening due to diagonal tension failure. Moreover, some additional cracks occur at the bottom of the piers due to sliding shear failure. When further steps are utilized, cracks at the corner of the door propagate diagonally towards the corners and the cracks at the bottom of the piers propagate horizontally. Illustration of the crack pattern of the wall is presented in Figure 3.40. Expected crack pattern of the wall matches with the pattern of the considered experimental study of Formica et al. (2002).

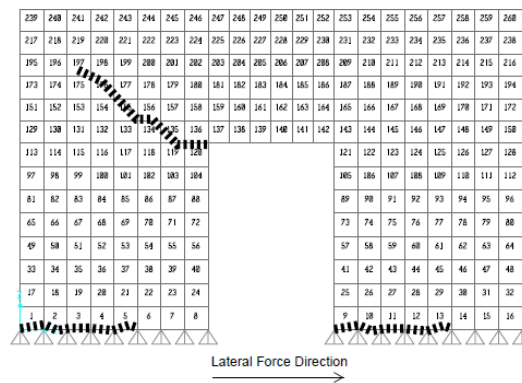


Figure 3.40. Expected Crack Pattern of Wall Model E2

3.6.2.3. Wall Model E3

Crack pattern of the wall model E3 is determined in three steps of post processing approach. Stress distributions of each step are presented in Figures 3.41a, 3.41b and 3.41c respectively.

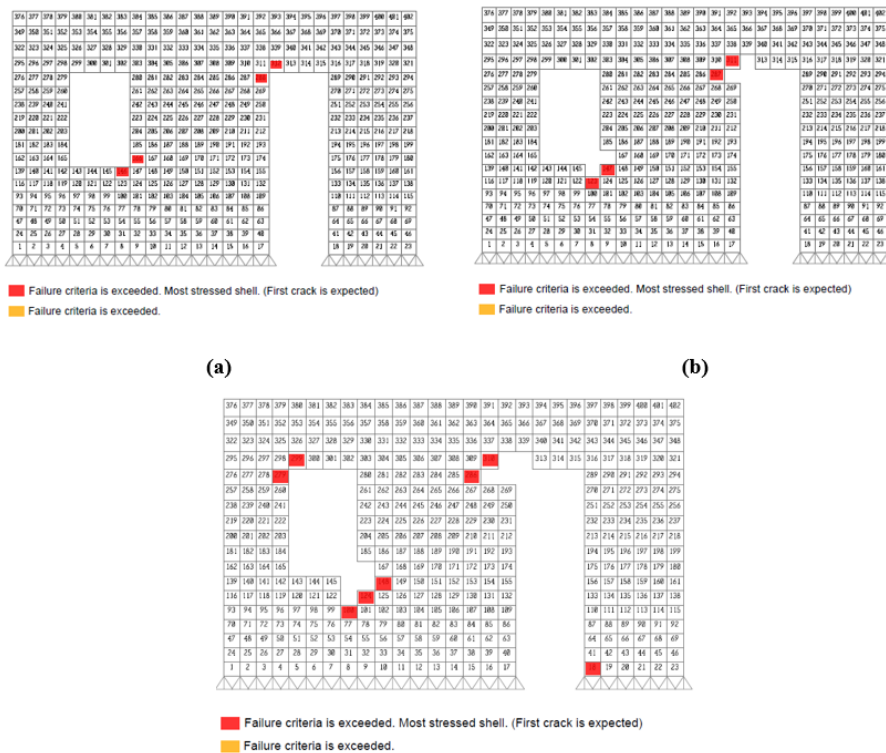


Figure 3.41. Post Processing Steps for Wall Model E3

First cracks initiate at the bottom corner of the window opening and the top corner of the door opening. Both cracks occur due to diagonal tension failure. When further steps are utilized, additional cracks are initiated. At the top corner of the window, new crack pattern occurs due to diagonal tension failure and in addition to that, right pier starts cracking from the bottom section due to sliding shear failure. Propagation of the cracks is utilized in Figure 3.42. Expected crack pattern of the wall matches with the pattern of the considered experimental study of Paquette and Bruneau (2006).



Figure 3.42. Expected Crack Pattern of Wall Model E3

3.6.2.4. Wall Model E4

Crack pattern of the wall model E4 is determined in two steps of post processing approach. Stress distributions of each step are presented in Figures 3.43a and 3.43b respectively.



(a)

(b)

Figure 3.43. Post Processing Steps for Wall Model E4

Cracks initiate from the cross corners of the openings. In addition to that, middle piers start to crack from their mid heights. Mostly diagonal tension failure dominates the collapse of the wall. When further step is utilized, cracks propagate diagonally. Pattern of the final crack propagation is presented in Figure 3.44. Expected crack pattern of the wall matches with the pattern of the considered experimental study of Abrams (1988).

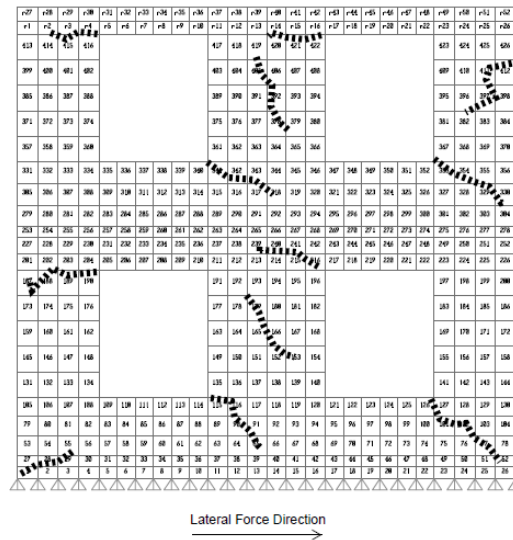
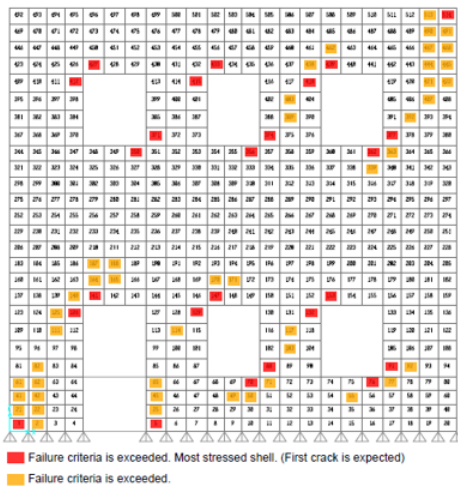


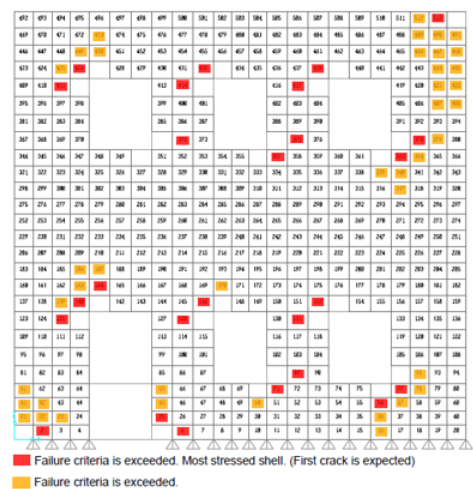
Figure 3.44. Expected Crack Pattern of Wall Model E4

3.6.2.5. Wall Model E5

Crack pattern of the wall model E5 is determined in two steps of post processing approach. Stress distributions of each step are presented in Figures 3.45a and 3.45b respectively.



(a)



(b)

Figure 3.45. Post Processing Steps for Wall Model E5

Cracks initiate from the cross corners of the openings and top and bottom of wall panel. Mostly diagonal tension failure dominates the collapse of the wall. However, sliding shear failure is observed at the left bottom and top right corners of the pier. When next step is utilized, cracks at the middle of the wall propagate diagonally and top and bottom corner pier cracks propagate horizontally. Pattern of the final crack propagation is presented in Figure 3.46. Expected crack pattern of the wall matches with the pattern of the considered experimental study of Moon et al. (2007).

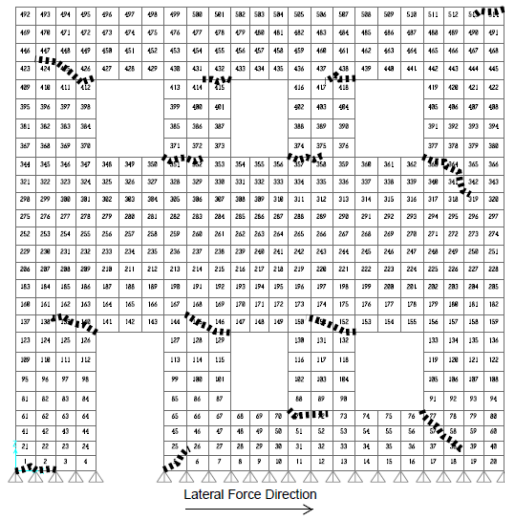


Figure 3.46. Expected Crack Pattern of Wall Model E5

3.6.2.6. Wall Model E6

Crack pattern of the wall model E6 is determined in two steps of post processing approach. Stress distributions of each step are presented in Figures 3.47a and 3.47b respectively.

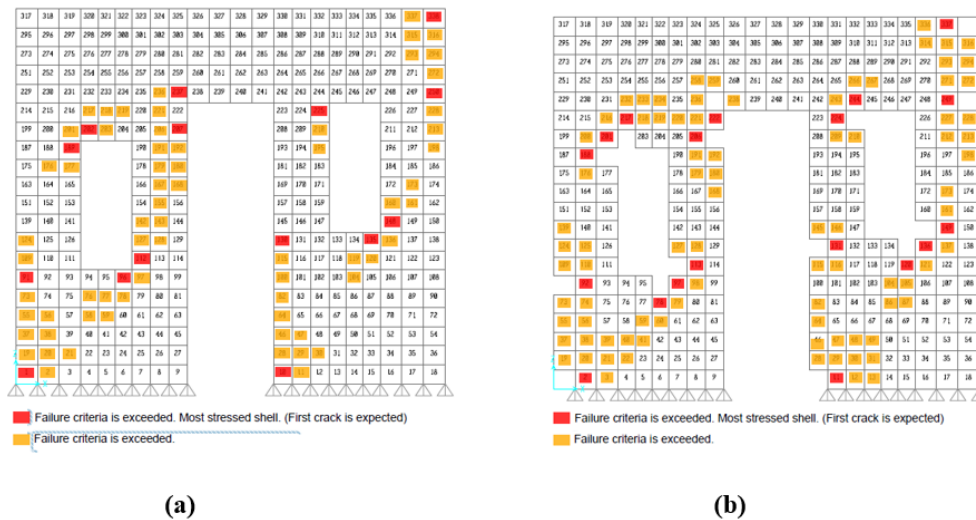


Figure 3.47. Post Processing Steps for Wall Model E6

Cracks initiate from the cross corners of the openings and top and bottom of wall panel. Mostly, diagonal tension failure dominates the collapse of the wall. However, sliding shear failure is observed at the left bottom and top right corners of the pier. When the next step is utilized, cracks at the middle of the wall propagate diagonally and top and bottom corner pier cracks propagate horizontally. Pattern of the final crack propagation is presented in Figure 3.48. Expected crack pattern of the wall matches with the pattern of the considered experimental study of Nateghi and Alemi (2008).

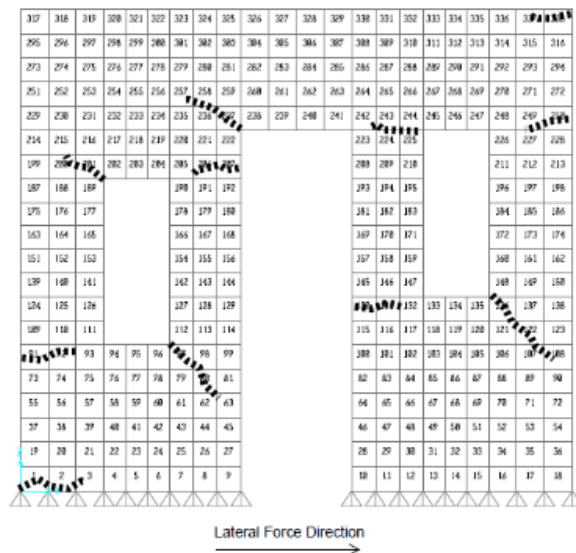


Figure 3.48. Expected Crack Pattern of Wall Model E6

3.7. Discussions of Numerical Calculations

First of all, it can be concluded that determination of the material properties in nonlinear modeling analysis is highly important. Moreover, using macro modeling approach instead of micro modeling approach have a significant impact on calculated analysis results. During the nonlinear analysis stage of this study, some of the material properties are not provided in the related experimental studies. For the missing ones,

equations given in Section 3.2 are used. That is why, the initial stiffnesses and top displacement limits are significantly different than experimental results. However, calculated ultimate lateral loads which are used in the second stage of modeling are generally in reasonable limits compared to experimental studies.

Besides that, ultimate strength of each wall is calculated with the help of different empirical approaches. Calculated ultimate strength limits are compared with the experimental and nonlinear analysis results. Thus, it is concluded that the empirical formulations of FEMA 273 and Akhaveissy (2013) give the best results for estimation of the ultimate strength of URM walls.

Initial crack locations and their propagations can be determined with simple linear modeling approach. As a result of the linear modeling approach, following conclusions can be made:

- Cracks initialize from corners of the openings in perforated URM walls with medium or slender piers. For solid walls with lower aspect ratios or perforated walls with squat piers, cracks initialize from the corners of edges or center of the walls.
- Based on the calculated stress conditions and crack propagations of wall models E4 and E5, severe damages are observed in the bottom story. For the upper stories, less damage is observed at the panels that are close to load application points and damage increases towards load application direction.

In the following chapter, a set of rules are proposed for estimation of damage patterns in URM walls. Above findings are used in Chapter 4 for completing the observational studies and fill the gaps to have a complete parametric set.

CHAPTER 4

SET OF RULES TO ESTIMATE DAMAGE PATTERNS OF URM WALLS

4.1. Introduction

In this chapter, a set of rules are proposed to estimate the initial crack locations as well as their propagations. With the help of the knowledge up to this point, in-plane damage patterns of the perforated URM walls under lateral loading can be established. Major parameters that govern the damage modes and crack patterns of the walls are employed in order to propose these rules.

4.2. Classification of Field Observations

Damaged wall photos from a vast number of post-earthquake reports (presented in Chapter 2.2 and Appendix A) are classified in this chapter with regards to their material property, material quality, axial load level, panel aspect ratio, description of cracks and idealized wall damage sketches. Numerical data obtained in Chapter 3 is also used to complement field data and to determine failure modes for different combinations of the aforementioned structural parameters.

Classification basis and procedure are explained in the following section. Material quality classification is based on observational study. Number of stories above the damaged walls is used to decide axial load level on damaged wall. Classification is presented in a tabular form as given in Appendix D.

4.3. Rules for Damage Patterns of URM Walls

Following set of rules are proposed to estimate in-plane damage and crack patterns of URM walls:

- Material property and quality are the most substantial parameters on sliding shear failure of URM walls. This parameter also defines the diagonal tension failure type rather it is stepped type cracks where cracks follow the path of the bed and head joints or nominal type cracks where cracks go through the brick. In an overview on Table D.1, it can be generally concluded that low material quality leads to sliding shear failure in URM walls. However, this is not the only parameter for sliding shear failure. Aspect ratio and axial load level are also important parameters for the development of sliding shear failure as well. In detail, material quality consists of two variables, which are mortar and unit strength. When mortar has less strength than unit, with low aspect ratio and axial load level, sliding shear failure is the most common failure type on URM walls. Besides that, lower mortar strength with low aspect ratio but higher axial load level develops stepped type diagonal tension failure. When mortar strength increases for the same aspect ratio and axial load level, cracks propagation changes from stepped type diagonal tension failure to nominal type of diagonal tension failure.
- Perforation geometry has a great impact on initializing and propagation of cracks. Cracks are initiated from the stress concentration locations at corners of the openings and tend to follow the shortest path towards other stress concentration points or free edges of piers (Çetinkaya, 2011, Javed et al., 2006).
- On the other hand, aspect ratio is highly dominant to determine in-plane failure modes of URM walls. As mentioned in Section 2.1, aspect ratio of walls should be investigated for each wall panel. As shown in Table D.1 in Appendix D, aspect ratios are evaluated in three categories which are slender ($\lambda > 2$), normal ($2 > \lambda > 1$) and squat ($1 > \lambda$). Slender URM wall panels cause URM walls to fail under flexural / toe crushing failure. Whereas, diagonal shear failure and sliding shear failure are the predominant failure modes for normal and squat URM walls, respectively.

- Axial load level is also a very important parameter for assessing the damage pattern of URM walls. As concluded in Penna et al. (2014), more severe in-plane wall damages are observed at the ground floors of buildings due to increase of the axial load. In addition, ELGawady (2004) states following interactions in URM walls. Walls with low aspect ratio and high axial load levels, nominal type of diagonal tension failure is more expected rather than stepped type diagonal tension failure. Furthermore, in case of low vertical load with low material quality, sliding shear failure is the predominant failure type in URM walls.

As mentioned above, none of the above parameters can define damage and crack patterns of URM walls individually. There should be at least two or three parameters for predetermining crack modes. Therefore, above proposed rules are combined in Table 4.1 as the “rules of predefined crack patterns”. Since damage on perforated URM walls occurs on the different panels as shown in Figure 2.1, Table 4.1 is valid for all types of perforated URM walls described in Section 2.1.

In Table 4.1, abbreviations for the failure modes can be described as follows:

- 1: Diagonal tension failure
- 2: Slide shear failure
- 3: Rocking - Flexural (Toe crush) failure

Table 4.1. Summary Table for Damage Pattern Rules of URM Walls

FAILURE MODES (*)		Axial Load Level		Material Quality		Aspect Ratio		
		High	Low	Good	Poor	Slender	Normal	Squat
Axial Load Level	High	-		1/3*	1/3*	3	1	1
	Low			1/3*	2	2/3**	1/2**	1/2**
Material Quality	Good	1/3*	1/3*			3	1	1
	Poor	1/3*	2			2/3***	1/2***	1/2***
Aspect Ratio	Slender	3	2/3**	3	2/3***	-		
	Normal	1	1/2**	1	1/2***			
	Squat	1	1/2**	1	1/2***			

(*) For crack formation in panels, refer to the conclusions on page 78 of Chapter 3.
 (1/2**) Failure mode 1 for "Good" material quality. Failure mode 2 for "Poor" material quality.
 (1/2***) Failure mode 1 for "High" axial load. Failure mode 2 for "Low" axial load.
 (1/3*) Failure mode 1 for "Normal" and "Squat" walls. Failure mode 3 for "Slender" walls.
 (2/3**) Failure mode 2 for "Poor" material quality. Failure mode 3 for "Good" material quality.
 (2/3***) Failure mode 2 for "Low" axial load. Failure mode 3 for "High" axial load.

4.4. Verification Study

At the end of this chapter, a case study based on the experimental campaign by Costley and Abrams (1996) is evaluated to verify the proposed rules for damage patterns of URM buildings. The test structure is a two-story brick masonry building with door and window openings. In the verification study, the observed damage and crack patterns are compared with the ones estimated by using the proposed rules in Table 4.1.

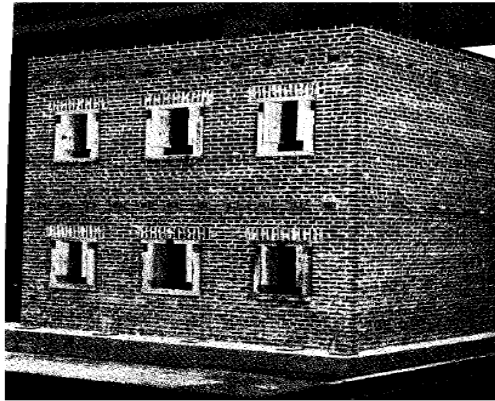


Figure 4.1. Window wall and out-of-plane wall of the tested structure (Costley et al. 1996)

There are two perforated walls on the tested URM building in direction of lateral loading setup. Geometric properties of the perforated walls of tested specimen are presented in Figure 4.2 together with the assigned wall panels labelled as shown. The walls at each story are treated individually since they are separated by rigid diaphragm floors.

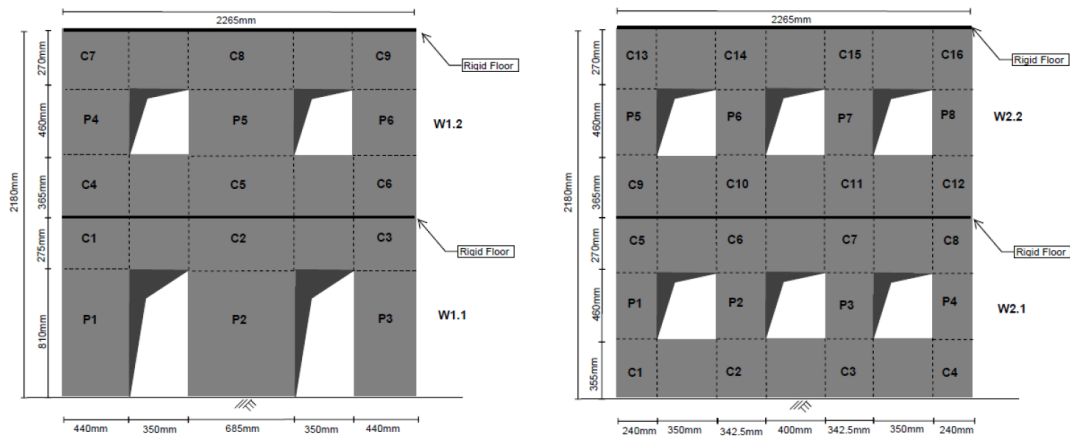


Figure 4.2. Geometric properties of Wall ID W1 and W2

In Table 4.2, axial stress level, material quality, panel aspect ratio, expected failure modes and observed failure modes of URM panels are given. Similar abbreviations for failure modes that used in Table 4.1 are again used in Table 4.2.

Table 4.2. Comparison of Expected and Real Failure Modes of URM Walls

Wall ID	Wall Type	Material Type	Material Quality	Axial stress grade	Panel ID	Panel Aspect Ratio	Expected Failure Mode based on Table 4.1	Observed Failure Mode on Specimen
W1.1	4	Clay Brick	Moderate	Medium	C1, C3	0.6	1	1
					C2	0.4	1	1
					P1, P3	1.8	1	1+3
					P2	1.2	1	1
W1.2				Low	C4	0.8	NDE	1+2
					C5	0.5	2	ND
					C6	0.8	2	1+2
					C7	0.6	NDE	2
					C8	0.4	2	ND
					C9	0.6	2	2
					P4	1.0	NDE	ND
					P5	0.7	2	ND
P6	1.0	1	ND					
W2.1	5	Clay Brick	Moderate	Medium	C1, C4	1.5	1	1
					C2, C3	1.0	1	ND
					C5, C8	1.1	1	1
					C6, C7	0.8	2	ND
					P1, P4	1.9	3	3
					P2, P3	1.3	1	1
					C9	1.5	1	1
W2.2				Low	C10, C11	1.1	1	ND
					C12	1.5	NDE	1
					C13	1.1	1	1
					C14	0.8	2	2
					C15	0.8	2	ND
					C16	1.1	NDE	ND
					P5	1.9	3	ND
					P6, P7	1.3	1	ND
P8	1.9	NDE	ND					
NDE: No damage expected based on the conclusions in Chapter 3. ND: No damage observed. Strength limit has not been exceeded.								

A sketch for comparison of expected damage patterns and real damage patterns of URM Walls 1 and 2 are presented in Figure 4.3 and Figure 4.4, respectively.

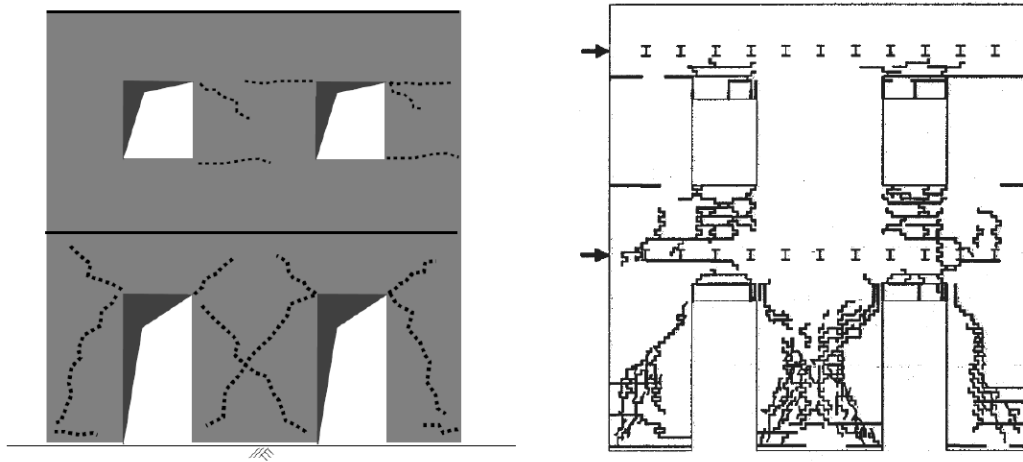


Figure 4.3. Expected vs. Real Damage Patterns of Wall ID. W1

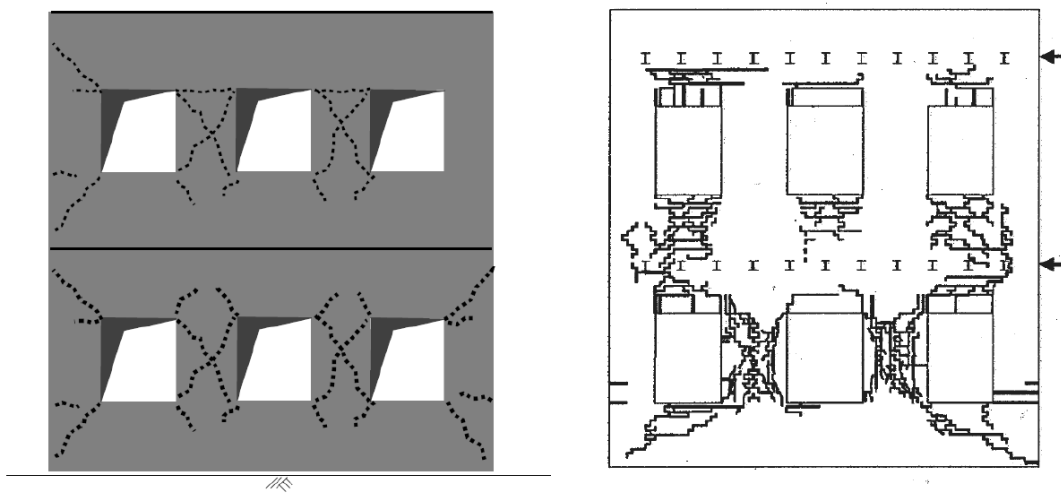


Figure 4.4. Expected vs. Real Damage Patterns of Wall ID. W2

Based on the results in Table 4.2 and in Figures 4.3 and 4.4, it can be stated that there is a reasonable match between the observed and expected damage and crack patterns for the considered case study. This means material quality, axial stress level and aspect ratio of the URM walls have great impact on predicting their damage patterns. These parameters can be determined by simple observations and without conducting any

complicated numerical models or calculations. As a final remark, this study proves that it is possible to make reasonable predictions of damage patterns for URM walls without complex modeling and calculations.

CHAPTER 5

SUMMARY AND CONCLUSIONS

5.1. Summary and Conclusions

This study is based on the predefined assessment of the in-plane behavior of URM walls under lateral loading and the main goal of this thesis study is to predict the damage and crack formations with their propagations by using observational data and without any complicated analysis. Study is conducted in three steps. In the first step, previous studies and post-earthquake reports of URM walls are investigated. Thus, in-plane behavior of URM walls is determined. In the next step, empirical approaches based on international and national documents research studies on URM walls are studied. By this means, ultimate lateral strength limits based on empirical formulations are determined, which is used in the next step of the study. Finally, mathematical modeling of URM walls is constituted. Walls with different perforation geometries are modeled. With the help of both linear and non-linear modeling, ultimate lateral strength limits and crack formations are determined. Then these three steps of the study are combined together to propose a set of rules to predict the damage and crack patterns of perforated URM walls. The study is completed by comparing the expected damage and crack patterns with the ones observed in an experimental campaign that has been selected as a verification case study.

According to the conducted work in this research, the following conclusions can be stated regarding the development of predefined damage patterns for non-engineered URM buildings:

- According to the observational studies, failure of URM walls starts from the stress concentration locations such as corners of the openings. Then, propagation of these cracks or in other words, failure mode is based on three

major structural parameters which are material type and quality, panel aspect ratio and axial load level.

- Three different empirical approaches are studied for URM walls. Among three approaches considered (FEMA 273, TBSC 2018 and Akhaveissy 2013), TBSC 2018 gives the most conservative limits. For normal and squat piers, FEMA 273 and Akhaveissy (2013) give almost the same limits. However, for slender piers, FEMA 273 gives highly conservative limits. As a result, empirical formulations introduced in Akhaveissy (2013) study gives the most reasonable limits compared to numerical modeling and experimental study results for URM walls.
- In this study, macro modeling approach is used to predict the in-plane behavior of URM walls. Expecting perfectly matched results compared to experimental studies are highly unlikely for such modeling type. However, as shown in Chapter 3, promising results are obtained in many wall models on ultimate lateral load capacities with the help of non-linear macro modeling. However, initial stiffnesses and ultimate top displacement results obtained from modeling are not matching with experimental results. This might be caused because of the following reasons. Firstly, some of the material properties such as internal friction angle, modulus of elasticity of masonry are not provided in the related experimental studies. Therefore, these properties are determined by using some empirical approaches. In addition, macro modeling approach is used in this study. It is necessary to accept the differences in top displacements and initial stiffness results since, the obtained ultimate lateral load capacities are almost matching which is important from the aim of this study.

Determination of the crack initial locations and their propagations, linear macro modeling is used. Consequently, it is a fact that cracks are initializing from corners of the openings in perforated URM walls with medium or slender piers. Solid walls with lower aspect ratios or perforated walls with squat piers, cracks are initializing from the corners of edges or center of the walls.

- The fact remains that, propagations of cracks define the failure mode of the walls. By using macro modeling diagonal tension failure and flexural failure can be determined while sliding shear failure cannot be determined. Sliding shear is comprised in the mortar of masonry. Without constitution of micro modeling, failure in mortar between units cannot be determined.
- As a final remark, this study supports that it is possible to make reasonable predictions of damage patterns for URM walls without complex modeling and calculations.

5.2. Future Research Recommendations

Future research topics regarding this study can be suggested as follows:

- More field data can be employed due to the fact that as the used data is enlarged, it becomes easier to draw conclusions out of it.
- New numerical wall models can be constructed to enlarge the limits of the parametric study for better understanding of the effects of the structural parameters on crack and damage patterns.
- This study can be used as an input to predict the in-plane lateral load capacity of perforated URM buildings by using theoretical failure analyses such as limit theorems. Stress states of panels can be estimated from the expected damage and crack patterns. Then by using the equilibrium conditions between panels, the lateral load capacity of the wall can be predicted.
- The results can be used in order to develop simple and practical performance assessment methods for a population of non-engineered URM buildings.

REFERENCES

- Abrams, D. (1988) Dynamic and static testing of reinforced concrete masonry Structures. 9th World Conference on Earthquake Engineering, Tokyo, vol. VI, pp. 169-174.
- Abrams, D. Shah N. (1992) A Cyclic load testing of unreinforced masonry walls. Report No. 92-26-10, Adv Constr. Technol Cent, Newmark Civil Eng. Lab, Dep Civil Eng., Univ Illinois Urbana-Champaign, USA
- Akhaveissy, A. H. (2013), Limit state strength of unreinforced masonry structures. Earthquake Spectra, Volume 29, No.1, Earthquake Engineering Research Institute.
- Ali, Q. Naeem, A. (2007), Seismic resistance evaluation of unreinforced masonry buildings. Journal of Earthquake Engineering 11:133-146, 2007.
- ASTM C55-17, Standard specification for concrete building brick, ASTM International, West Conshohocken, PA, 2017.
- Auroville Earth Institute, disaster resistance, earthquake and structures department http://www.earth-auroville.com/gujarat_rehabilitation_after_the_earthquake_en.php (2017)
- Basoenondo, E.A. (2008), Lateral load response of Cikarang brick wall structures – An experimental study. Phd. Thesis of Queensland University of Technology.
- Bayülke, N. (2011), Yığma yapıların deprem davranışı ve güvenliği. 1. Türkiye Deprem Mühendisliği ve Sismoloji Konferansı 11-14 Ekim 2011 – ODTÜ – ANKARA

- Beatie, G. Bonowitz, D. Breiholz, D. Coil, J. Dyce, D. Ficcadenti, S. Filiatrault, A. Gaul, R. Gillespie, A. Hall, J. (2007), General guidelines for the assessment and repair of earthquake damage in residential wood frame buildings. CUREE Publication No.EDA-02
- Benedetti, D. Pezzoli, P. (1996), Shaking table tests on masonry buildings results and comments. ISMES Seriate Bergamo Italy, 1996.
- Benedetti, D. Carydis, P. Pezzoli, P. (1998), Shaking table tests on 214 simple masonry buildings. Earthquake Engineering and Structural Dynamics Vol: 24, 67-90.
- Binda, L. Cardani, G. Saisi, A. Modena, C. Valluzzi, M. R. Marchetti, L. (2005), Guidelines for restoration and improvement of historical centers in seismic regions: the Umbria experience. Structural Analysis of Historical Constructions - Modena, Lourenço & Roca (eds) 2005 Taylor & Francis Group, London, ISBN 04 1536 379 9
- British Standards Institution. Eurocode 6 (2005): Rules for reinforced and unreinforced masonry (together with United Kingdom national application document). London: British Standards Institution.
- Bothara, J. K. Dhakal, R. P. Mander J. B. (2010), Seismic performance of an unreinforced masonry building: An experimental investigation. Earthquake Engineering Structural Dynamics 2010; 39:45–68
- Bothara, J. K. Brzev, S. (2011), Improving the seismic performance of stone masonry Buildings. Earthquake Engineering Research Institute 499 14th Street, Suite 320 Oakland, CA 94612-1934 USA, WHE-2011-01.
- Building Change (2015), Build Change Post-Disaster Reconnaissance Report on April 25, 2015 Gorkha Earthquake, Nepal.

- Celep, Z. Erken, A. Taskin, B. Ilki, A. (2011), Failures of masonry and concrete buildings during the March 8, 2010 Kovancilar and Palu (Elazığ) Earthquakes in Turkey. *Engineering Failure Analysis* 18 (2011) 868-889.
- Ceran, B. (2010), Seismic vulnerability of masonry structures in Turkey. A Thesis Submitted to the Graduate School of Natural and Applied Sciences of Middle East Technical University
- Çetinkaya, N. (2011), 2010 Karakocan-Elazığ earthquake and masonry structures. *Nat. Hazards Earth Syst. Sci.*, 11, 11–16, 2011.
- Choudhury, T. Milani, G. Kaushik, H. B. (2015) Comprehensive numerical approaches for the design and safety assessment of masonry buildings retrofitted with steel bands in developing countries. The case of India. *Construction and Building Materials Journal*.
- Costley, A.C. Abrams, D.P. (1996), Dynamic response of unreinforced masonry buildings with flexible diaphragms. NCEER-96-0001, University of Buffalo, Buffalo, N.Y.
- CSI (Computers and Structures Inc.) (2009), SAP2000 v14.1.0 Integrated Finite Element Analysis and Design of Structures. CSI, Berkeley.
- Dizhur, D. Ingham, J. Moon, L. Griffith, M. Schultz, A. Senaldi, I, Magenes, G. Dickie, J. Lissel, S. Centeno, J. Ventura, C. Leite, J. Lourenco, P. (2011), Performance of masonry buildings and churches in the 22 February 2011 Christchurch Earthquake. *Bulletin of the New Zealand Society for Earthquake Engineering*, Vol. 44, No. 4.
- EERC (1995), Dinar Earthquake Archive. Earthquake Engineering Research of Center Middle East Technical University
- Free, M. Rossetto, T, Peiris, N. Taucer, F. Zhao, B. Koo, R. Wang, J. Ma, X. Verrucci, E. (2008), A preliminary field report by EEFIT. The Wenchuan, China Earthquake of 12 May 2008

- Friedman, D. A. Elwood K. J. (2008), Wenchuan Earthquake May 12th, 2008. EERI/GEER Reconnaissance Team Field Report 8/3/08 to 8/11/08.
- Doğangün, A. Ural, A. Livaoğlu. R. (2008), Seismic performance of masonry buildings during recent earthquakes in Turkey. The 14th World Conference on Earthquake Engineering October 12-17, 2008, Beijing, China.
- Dhanasekar M, Haider W. (2007), Explicit finite element analysis of lightly reinforced masonry shear walls. *Computers and Structures* 86 (2008) 15–26.
- Dolce, M. (1997), “La Valutazione della Vulnerabilità per le Analisi di Rischio e gli Scenari di Danno”. *L’Ingegneria Sismica in Italia, Atti VIII Convegno Nazionale ANIDIS, Taormina (in Italian)*.
- EERI (2011), Damage to village masonry houses. <http://www.eqclearinghouse.org/2011-10-23-eastern-turkey/welcome-to-the-eastern-turkey-earthquake-clearinghouse/dsc03835-2/>
- ElGawady, M. (2004), Seismic in-plane behavior of URM walls upgraded with composites. Thèse No 3111 (2004) École Polytechnique Fédérale de Lausanne.
- ElGawady, M. Lestuzzi, P. Badoux, (2005), Performance of masonry under in-plane seismic loading. *TMS Journal*.
- Elvin, A. Uzoegbo, H.C. (2011) Response of a full-scale dry-stack masonry structure subject to experimentally applied earthquake loading. *Journal of the South African Institution of Civil Engineering*.
- Farshchi, D.M. Motavalli, M. Schaumacher, A. Marefet, M.S. (2009), Numerical modelling of in-plane behavior of URM walls and an investigation into aspect ratio, vertical and horizontal post tensioning and head joint as parametric study. *Archives of Civil and Mechanical Engineering of ACME*.

FEMA 273, NEHRP Guidelines for the seismic rehabilitation of buildings. 1997.

Formica, G. Sansalone, V. Casciaro, R. (2002) A mixed solution strategy for the nonlinear analysis of brick masonry walls. *Comput. Methods Appl. Mech. Eng.* 191 (2002) 5847–5876

Ganz, H.R. Thürlimann, B. (1985), Plastic strength of masonry shear walls. Institute Struct Eng, ETH Zurich; 1984 (in German).

Illampas, R. Charmpis, D.C. Ioannou, I. (2014), Laboratory testing and finite element simulation of the structural response of an adobe masonry building under horizontal loading. *Engineering Structures*, 80 (2014) 362-376.

Jagadish, K. S. Raghunath, S. Nanjunda Rao, K. S. (2003), Behaviour of masonry structures during the Bhuj earthquake of January 2001. *Proc. Indian Acad. Sci. (Earth Planet. Sci.)*, 112, No. 3, September 2003, pp. 431-440

Javed, M., Khan A.N., Penna, A., Magenes, G., (2006), Behavior of masonry structures during the Kashmir 2005 earthquake. First European Conference on Earthquake Engineering and Seismology, Geneva Switzerland.

Kaushik, H.B. Rai, D.C. Jain, S.K. (2007), Stress-strain characteristics of clay brick masonry under uniaxial compression. *Journal of Materials in Civil Engineering* © ASCE

Kalali, A. Kabir, M.Z. (2012), Cyclic behavior of perforated masonry walls strengthened with glass fiber reinforced polymers. Department of Civil and Environmental Engineering, Amirkabir University of Technology, P.O. Box. 15875-4413, Tehran, Iran.

Kaplan, H. Bilgin, H. Yilmaz, S. Binici, H. Öztas, A. (2010), Structural damages of L'Aquila (Italy) earthquake. *Natural Hazards Earth System Sciences*, 10, 499–507, 2010.

- Karantoni, F. V. Fardis, M. N. (1992), Computed versus observed seismic response and damage of masonry buildings. *Journal of Structural Engineering*, Vol. 118, No.7, July, 1992. ©ASCE, ISSN 0733-9445/92/0007-1804
- Kawa, M. Pietruszczak, S. Shieh-Beygi, B. (2008), Limit states for brick masonry based on homogenization approach. *International Journal of Solids and Structures* 45 (2008) 998–1016
- Korkmaz, H. H. Korkmaz, S.Z. Donduren, M. S. (2010), Earthquake hazard and damage on traditional rural structures in Turkey. *Natural Hazards Earth System Sciences.*, 10, 605–622, 2010
- Lourenco, P. B. Rots, J.G. Blaauwendraad, J. (1995), Two approaches for the analysis of masonry structures: Micro and macro modelling. *Heron*, vol. 40.
- Lourenco, P. B. Avila, L. Vasconcelos, G. Alves, J. P. Mendes, N. Costa, A. Experimental investigation on the seismic performance of masonry buildings using shaking table testing. *Bull Earthquake Engineering* DOI 10.1007/s10518-012-9410-7.
- Magenes, G. Penna, A. Rota, M. Galasco, A. Senaldi, I. (2012), Shaking table test of a full-scale stone masonry building with stiffened floor and roof diaphragms. 15 WCEE, Lisboa.
- Meguro, K. Uehan, F. Ramancharla, P. K. (2001), Damage to Masonry Structures. *Building Damage Report*.
- Malla, S. (2015), Lessons of 2015 Nepal Earthquake Disaster. Zurich, Switzerland
- Moon, F.L. Yi, T. Leon, R. Kahn, L. (2007), Testing of a Full-Scale Unreinforced Masonry Building Following Seismic Strengthening. *Journal of Structural Engineering* © ASCE.

- Mosalam K, Glascoe L, Bernier J, (2009), Mechanical properties of unreinforced brick masonry, Section 1. Lawrence Livermore National Laboratory: LLNL-TR-417646.
- Nagethi, F. Alemi, F. (2008), Experimental study of seismic behavior of typical Iranian URM brick walls. 14 WCEE Beijing, China
- Osteraas, J. (2006), Post-earthquake building damage assessment. EERI
- Paquette, J. Bruneau, M. (2006), Pseudo-dynamic testing of unreinforced masonry building with flexible diaphragm and comparison with existing procedures. *Construction and Building Materials* 20 (2006) 220–228
- Penna, A. Moradini, P. Rota, M. Manzini, C.F. Porto, F. Magenes, G. (2014), Performance of masonry buildings during the Emilia 2012 earthquake. *Bull Earthquake Eng* (2014) 12:2255–2273 DOI 10.1007/s10518-013-9496-6.
- Petry, S. Beyer K. (2015), Cyclic test data of six URM walls with different masonry conditions. M.EERI Earthquake Engineering and Structural Dynamics Laboratory (EESD) Lausanne, Switzerland.
- Petry, S. Beyer K. (2014), Influence of boundary conditions and size effect on the drift capacity of URM walls. Earthquake Engineering and Structural Dynamics Laboratory (EESD) Lausanne, Switzerland.
- Polimi (2010), New Integrated knowledge-based approaches to the protection of cultural heritage from earthquake-induced risk. NIKER, Università di Padova (Italy) 244123.
- Saloustros, S. Pela, L. Cervera, M. Roca. P. (2017), An enhanced finite element macro-model for the realistic simulation of the localized cracks in masonry structures: A large-scale application. *International Journal of Architectural Heritage*. DOI: 10.1016/j.enfracmech.2015.10.039.

Tarque, N. Crowley, H. Pinho, R. Varum, H. (2012), Displacement based fragility curves for seismic assessment of adobe buildings in Cusco, Peru. Earthquake Spectra [DOI: 10.1193/1.4000001].

TBSC 2018, Turkish Building Seismic Code: Specifications for buildings under earthquake effects. 2019.

Thakur, S. K. (2007), Post Earthquake Quick Damage inspection of buildings in Nepal. Collaborative Research and Development (R&D) Project for Disaster Mitigation in Earthquake Prone Areas in Asia (Sep 27, 2007)

Vasconcelos, G. Lourenço, P. B. (2009), Experimental characterization of stone masonry in shear and compression. Construction and Building Materials 23 (2009) 3337-3345

Wijanto, L.S. (2007), Seismic assessment of unreinforced masonry walls. Department of Civil Engineering University of Canterbury Christchurch, New Zealand.

Zülfükar, C. Kamer, Y. Vuran, E. (2011), 19 Mayıs 2011 Kütahya-Simav depremi. Kandilli Rasathanesi ve Deprem Araştırma Enstitüsü, Boğaziçi University.

APPENDICES

A. Field Observation of Damage on Perforated Masonry Walls Photo Archive

In this appendix, photos from field observation of seismic damage on perforated masonry walls are presented in Table A.1. Categorization details of the photos are explained in Chapter 2.1. 70 different cases have been examined with adequate number of samples from each specified wall type.

Table A.1. *Damaged Perforated Wall Photographs in Real Seismic Events*

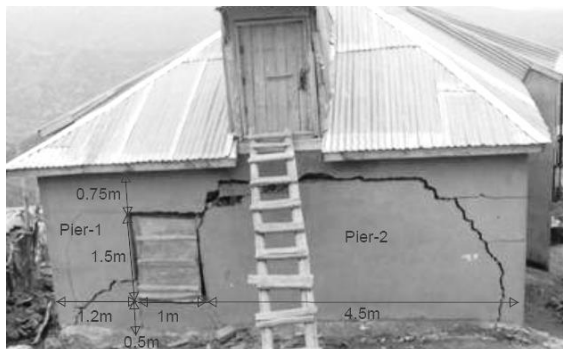
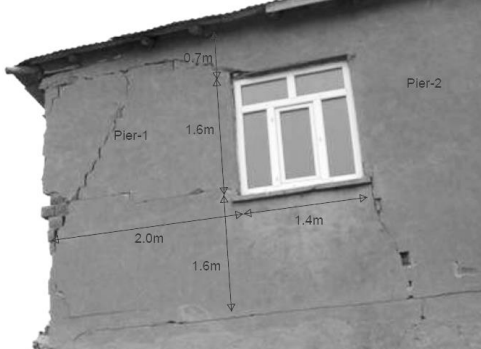
	<ul style="list-style-type: none"> - Wall type: 1 - Wall ID: F2 - Axial stress ratio: Low - Material type: Clay brick - Reference: Ceran (2010)
	<ul style="list-style-type: none"> - Wall type: 1 - Wall ID: F3 - Axial stress ratio: Low - Material type: Clay brick - Reference: Ceran (2010)

Table A.1 (continued)

	<ul style="list-style-type: none"> - Wall type: 1 - Wall ID: F4 - Axial stress ratio: Low (1st floor), medium (ground floor). - Material type: Stone - Reference: METU EERC (1995)
	<ul style="list-style-type: none"> - Wall type: 1 - Wall ID: F5 - Axial stress ratio: Low (2nd floor), medium (1st floor). - Material type: Clay brick - Reference: Penna et al. (2014)

Table A.1 (continued)

	<ul style="list-style-type: none"> - Wall type: 1 - Wall ID: F6 - Axial stress ratio: Medium - Material type: Clay brick - Reference: Cetinkaya (2011)
	<ul style="list-style-type: none"> - Wall type: 1 - Wall ID: F7 - Axial stress ratio: Medium - Material type: AAC - Reference: Jagadish et al. (2003)
	<ul style="list-style-type: none"> - Wall type: 1 - Wall ID: F8 - Axial stress ratio: Medium - Material type: Clay - Reference: Building Change (2015)

Table A.1 (continued)

	<ul style="list-style-type: none"> - Wall type: 1 - Wall ID: F9 - Axial stress ratio: Low - Material type: Stone - Reference: Thakur (2007)
	<ul style="list-style-type: none"> - Wall type: 1 - Wall ID: F10 - Axial stress ratio: Low - Material type: Hollow clay - Reference: EERI (2011)
	<ul style="list-style-type: none"> - Wall type: 1 - Wall ID: F11 - Axial stress ratio: Low - Material type: Clay - Reference: METU EERC (1995)

Table A.1 (continued)

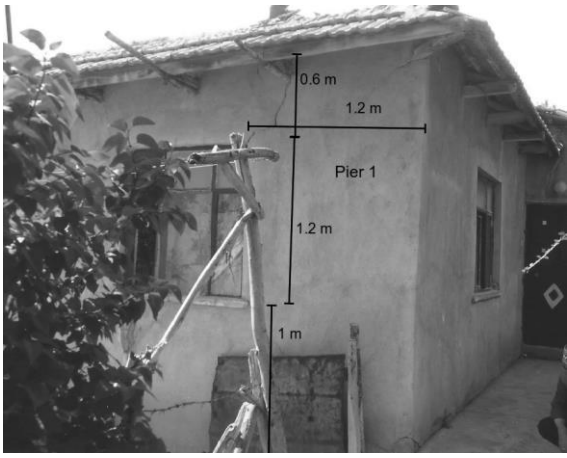
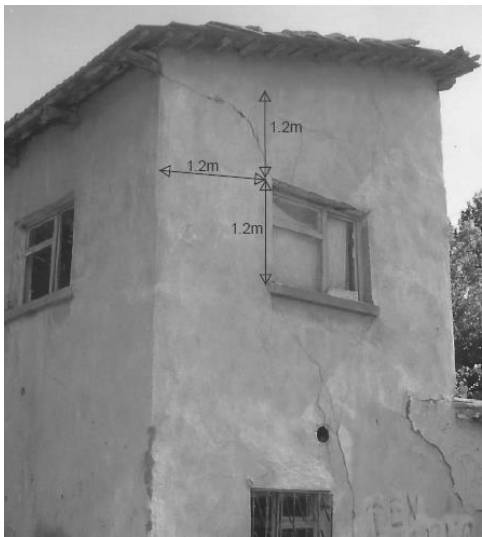
 <p>0.6 m 1.2 m Pier 1 1.2 m 1 m</p>	<ul style="list-style-type: none"> - Wall type: 1 - Wall ID: F12 - Axial stress ratio: Low - Material type: Clay - Reference: METU EERC (1995)
 <p>1.2 m 1.2 m 1.2 m</p>	<ul style="list-style-type: none"> - Wall type: 1 - Wall ID: F13 - Axial stress ratio: Low - Material type: Adobe - Reference: METU EERC (1995)
 <p>1.2 m 1.4 m 1.4 m</p>	<ul style="list-style-type: none"> - Wall type: 1 - Wall ID: F14 - Axial stress ratio: Low - Material type: Clay - Reference: METU EERC (1995).

Table A.1 (continued)

<p>0.2m 0.9m 1.35m 0.8m 2m Pier 2 Pier 1</p>	<ul style="list-style-type: none"> - Wall type: 2 - Wall ID: F16 - Axial stress ratio: N/A - Material type: Clay - Reference: Dogangun et al. (2008)
<p>1m 0.75m 2.9m 2.3m Pier -1</p>	<ul style="list-style-type: none"> - Wall type: 2 - Wall ID: F17 - Axial stress ratio: Low - Material type: Clay - Reference: Building Change (2015)
<p>1.3m 1.2m 2.1m 1.5m 2.1m Pier -1a Pier -1b</p>	<ul style="list-style-type: none"> - Wall type: 2 - Wall ID: F18 - Axial stress ratio: Low - Material type: Clay Brick - Reference: Tarque et al. (2012)

Table A.1 (continued)

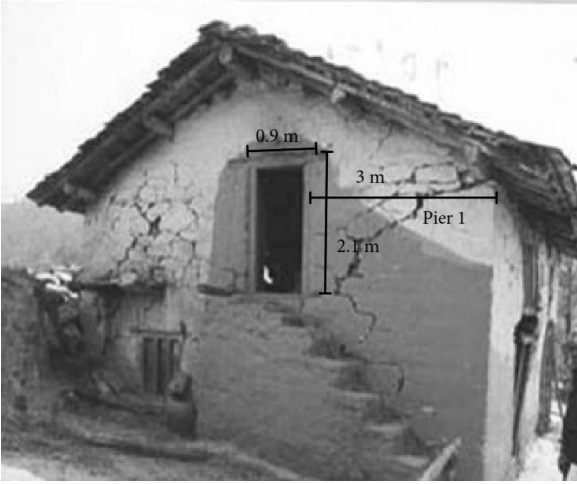
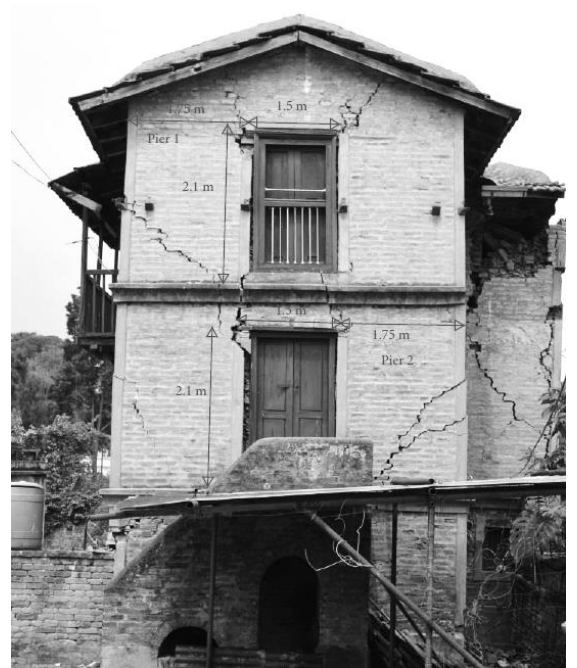
	<ul style="list-style-type: none">- Wall type: 2- Wall ID: F19- Axial stress ratio: Low- Material type: Adobe- Reference: Thakur (2007)
	<ul style="list-style-type: none">- Wall type: 2- Wall ID: F20- Axial stress ratio: Low- Material type: Clay- Reference: Malla (2015)

Table A.1 (continued)

	<ul style="list-style-type: none"> - Wall type: 2 - Wall ID: F21 - Axial stress ratio: Low - Material type: Clay - Reference: METU EERC (1995)
	<ul style="list-style-type: none"> - Wall type: 3 - Wall ID: F22 - Axial stress ratio: Low - Material type: Clay - Reference: METU EERC (1995)
	<ul style="list-style-type: none"> - Wall type: 3 - Wall ID: F24 - Axial stress ratio: High - Material type: Clay - Reference: Elgawady (2004).
	<ul style="list-style-type: none"> - Wall type: 3 - Wall ID: F25 - Axial stress ratio: Low - Material type: Adobe Reference: Auroville Earth Institute (2017)

Table A.1 (continued)

	<ul style="list-style-type: none"> - Wall type: 3 - Wall ID: F26 - Axial stress ratio: Low - Material type: Stone - Reference: Bothara et al. (2011)
	<ul style="list-style-type: none"> - Wall type: 3 - Wall ID: F27 - Axial stress ratio: Low - Material type: Concrete masonry - Reference: METU EERC (1995) -
	<ul style="list-style-type: none"> - Wall type: 3 - Wall ID: F28 - Axial stress ratio: Medium - Material type: Clay - Reference: METU EERC (1995)
	<ul style="list-style-type: none"> - Wall type: 3 - Wall ID: F29 - Axial stress ratio: Low - Material type: Clay - Reference: METU EERC (1995)

Table A.1 (continued)

	<ul style="list-style-type: none"> - Wall type: 3 - Wall ID: F30 - Axial stress ratio: Low - Material type: Clay - Reference: METU EERC (1995)
	<ul style="list-style-type: none"> - Wall type: 3 - Wall ID: F31 - Axial stress ratio: Low - Material type: Clay - Reference: METU EERC (1995)
	<ul style="list-style-type: none"> - Wall type: 4 - Wall ID: F33 - Axial stress ratio: Low - Material type: Clay - Reference: Auroville Earth Institute (2017)

Table A.1 (continued)

	<ul style="list-style-type: none">- Wall type: 4- Wall ID: F34- Axial stress ratio: Medium- Material type: Clay- Reference: Zulfukar et al. (2011)
	<ul style="list-style-type: none">- Wall type: 4- Wall ID: F35- Axial stress ratio: Medium- Material type: Clay- Reference: Meguro et al. (2001)

Table A.1 (continued)

	<ul style="list-style-type: none"> - Wall type: 4 - Wall ID: F36 - Axial stress ratio: Low - Material type: Clay - Reference: Celep et al. (2011)
	<ul style="list-style-type: none"> - Wall type: 4 - Wall ID: F37 - Axial stress ratio: Low - Material type: Clay - Reference: Celep et al. (2011)
	<ul style="list-style-type: none"> - Wall type: 4 - Wall ID: F38 - Axial stress ratio: Low - Material type: Clay - Reference: Polimi (2010)

Table A.1 (continued)

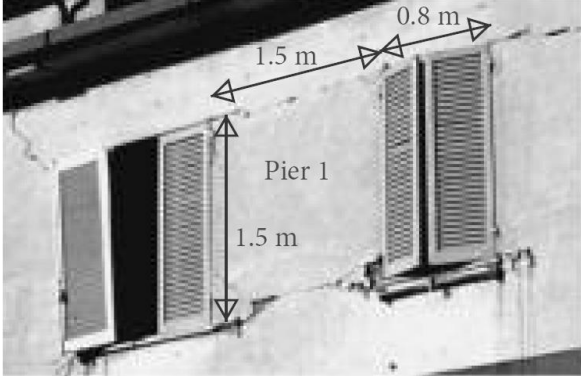
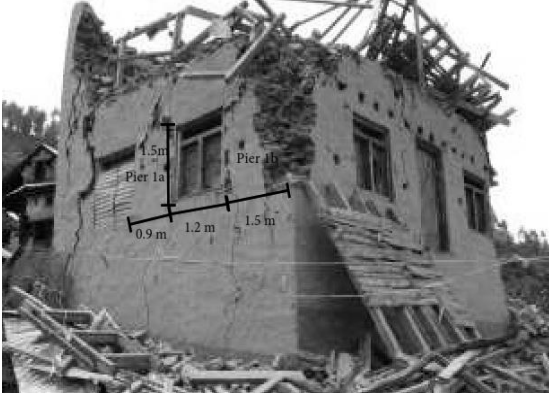
	<ul style="list-style-type: none"> - Wall type: 4 - Wall ID: F39 - Axial stress ratio: Low - Material type: Clay - Reference: Polimi (2010)
	<ul style="list-style-type: none"> - Wall Type: 4 - Wall ID: F40 - Axial stress ratio: Low - Material type: Adobe - Reference: Auroville Earth Institute (2017)
	<ul style="list-style-type: none"> - Wall type: 4 - Wall ID: F41 - Axial stress ratio: Low - Material type: Clay - Reference: Dogangun et al. (2008)

Table A.1 (continued)

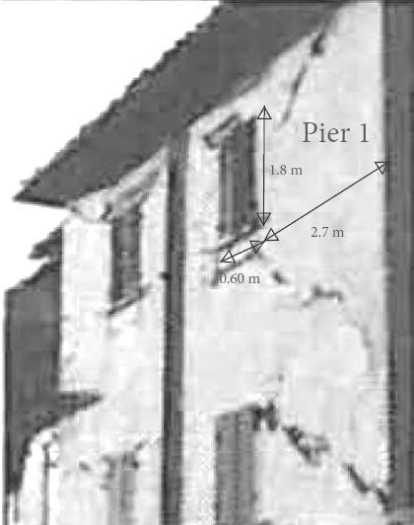
	<ul style="list-style-type: none"> - Wall type: 4 - Wall ID: F42 - Axial stress ratio: Low - Material type: Clay - Reference: Binda et al. (2005)
	<ul style="list-style-type: none"> - Wall type: 4 - Wall ID: F43 - Axial stress ratio: High - Material type: Clay - Reference: Thakur (2007)
	<ul style="list-style-type: none"> - Wall type: 4 - Wall ID: F44 - Axial stress ratio: Medium - Material type: Solid clay - Reference: Beatie et al. (2007)

Table A.1 (continued)

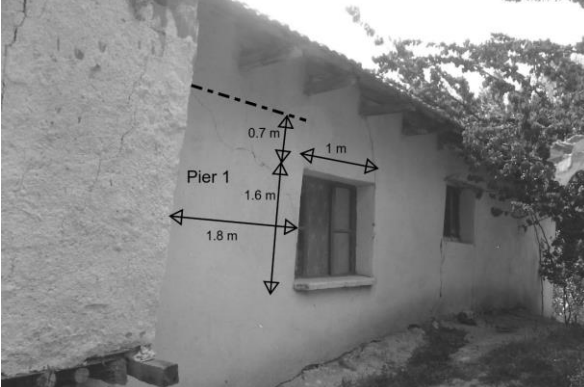
	<ul style="list-style-type: none"> - Wall type: 4 - Wall ID: F45 - Axial stress ratio: Medium - Material type: Clay - Reference: Malla (2015)
	<ul style="list-style-type: none"> - Wall type: 4 - Wall ID: F46 - Axial stress ratio: Low - Material type: Clay - Reference: METU EERC (1995)
	<ul style="list-style-type: none"> - Wall type: 4 - Wall ID: F47 - Axial stress ratio: Low - Material type: Clay - Reference: METU EERC (1995)

Table A.1 (continued)

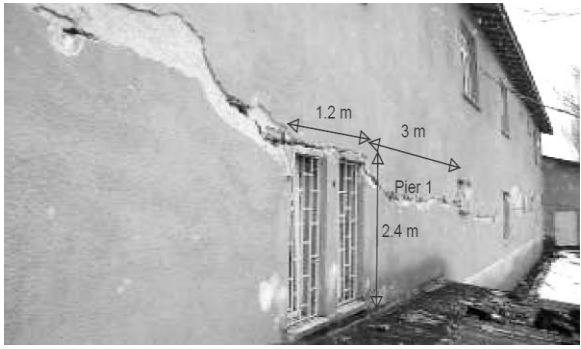
	<ul style="list-style-type: none"> - Wall type: 4 - Wall ID: F48 - Axial stress ratio: Low - Material type: Adobe - Reference: METU EERC (1995)
	<ul style="list-style-type: none"> - Wall type: 5 - Wall ID: F50 - Axial stress ratio: Medium - Material type: Clay - Reference: Korkmaz et al. (2010)
	<ul style="list-style-type: none"> - Wall type: 5 - Wall ID: F51 - Axial stress ratio: Low - Material type: Clay - Reference: Javed et al. (2006)

Table A.1 (continued)

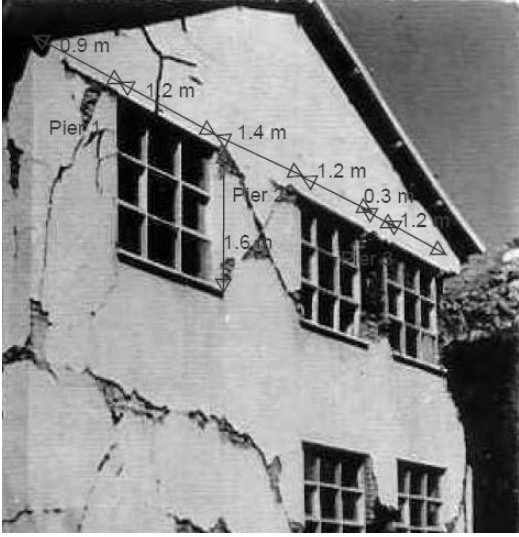
	<ul style="list-style-type: none"> - Wall type: 5 - Wall ID: F52 - Axial stress ratio: Low - Material type: Stone - Reference: Elgawady (2004)
	<ul style="list-style-type: none"> - Wall type: 5 - Wall ID: F53 - Axial stress ratio: Low - Material type: Clay - Reference: Bayulke (2011)
	<ul style="list-style-type: none"> - Wall type: 5 - Wall ID: F54 - Axial stress ratio: Low - Material type: Clay - Reference: Zulfukar (2011)

Table A.1 (continued)

	<ul style="list-style-type: none"> - Wall type: 5 - Wall ID: F55 - Axial stress ratio: Low - Material type: Stone - Reference: Kaplan et al. (2010)
	<ul style="list-style-type: none"> - Wall type: 5 - Wall ID: F56 - Axial stress ratio: Low - Material type: Clay - Reference: Karantoni et al. (1992)

Table A.1 (continued)

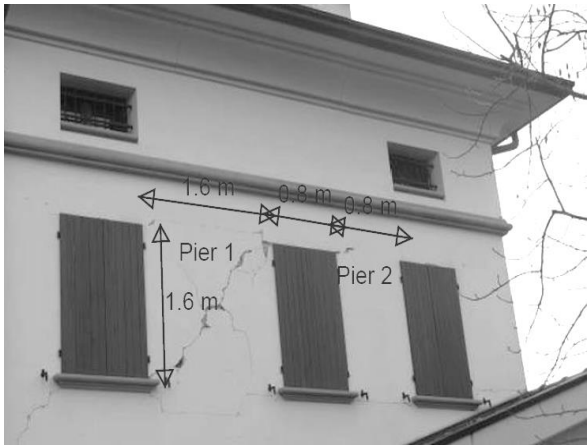
	<ul style="list-style-type: none"> - Wall type : 5 - Wall ID: F57 - Axial stress ratio: Low - Material type: Clay - Reference: Penna et al. (2014) -
	<ul style="list-style-type: none"> - Wall type: 5 - Wall ID: F58 - Axial stress ratio: Low - Material type: Stone - Reference: Cetinkaya (2011) -
	<ul style="list-style-type: none"> - Wall type: 5 - Wall ID: F59 - Axial stress ratio: Medium - Material type: Clay - Reference: Korkmaz et al. (2010)

Table A.1 (continued)

	<ul style="list-style-type: none"> - Wall type : 5 - Wall ID: F60 - Axial stress ratio: Low - Material type: Clay <p>Reference: Polimi (2010)</p>
	<ul style="list-style-type: none"> - Wall type: 5 - Wall ID: F61 - Axial stress ratio: Low - Material type: Clay <p>Reference: Dizhur et al. (2011)</p>
	<ul style="list-style-type: none"> - Wall type: 5 - Wall ID: F62 - Axial stress ratio: Medium (ground floor), low (1st floor) - Material type: Clay <p>Reference: Friedman et al. (2008)</p>

Table A.1 (continued)

	<ul style="list-style-type: none"> - Wall type: 5 - Wall ID: F63 - Axial stress ratio: Medium (ground floor), low (1st floor) - Material type: Clay - Reference: Friedman et al. (2008)
	<ul style="list-style-type: none"> - Wall type: 5 - Wall ID: F64 - Axial stress ratio: High (1st floor) - Material type: Clay - Reference: Free et al. (2008)
	<ul style="list-style-type: none"> - Wall type: 5 - Wall ID: F65 - Axial stress ratio: Low - Material type: Adobe - Reference: METU EERC (1995)

Table A.1 (continued)

	<ul style="list-style-type: none"> - Wall type: 5 - Wall ID: F66 - Axial stress ratio: Low - Material type: Clay - Reference: METU EERC (1995)
	<ul style="list-style-type: none"> - Wall type: 6 - Wall ID: F67 - Axial stress ratio: High (1st story) and Low (2nd story) - Material type: Clay - Reference: Penna et al. (2014)
	<ul style="list-style-type: none"> - Wall type: 6 - Wall ID: F69 - Axial stress ratio: Low - Material type: Clay - Reference: Dogangun et al. (2008)

Table A.1 (continued)



- Wall type: 6
- Wall ID: F70
- Axial stress ratio: Medium
- Material type: Clay
- Reference: Zulfukar et al. (2011)

B. Experimental Observation of Damage on Perforated Masonry Walls Photo Archive

In this appendix, photos from experimental observation of damage on perforated masonry walls are presented in Table B.1. Categorization details of the photos are explained in Chapter 2.4. There are 14 different cases including all wall types except wall type 5.

Table B.1. *Damaged Perforated Wall Photographs in Experimental Studies*

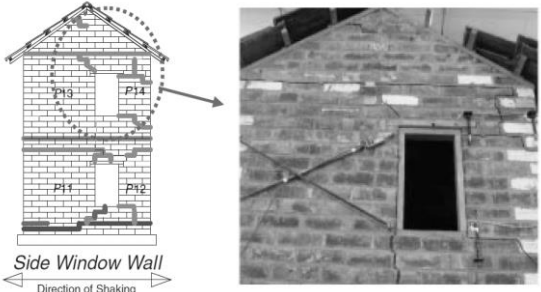
	<ul style="list-style-type: none"> - Wall type: 1 - Wall ID: E7 - Axial stress ratio: Low - Material type: Hollow clay brick - Damage Pattern: Diagonal tension crack - Reference: Bothara et al. (2010)
	<ul style="list-style-type: none"> - Wall type: 1 - Wall ID: E8 - Axial stress ratio: Low - Material type: Adobe brick - Damage Pattern: Diagonal tension crack - Reference: Blondet et al. (2006)

Table B.1 (continued)

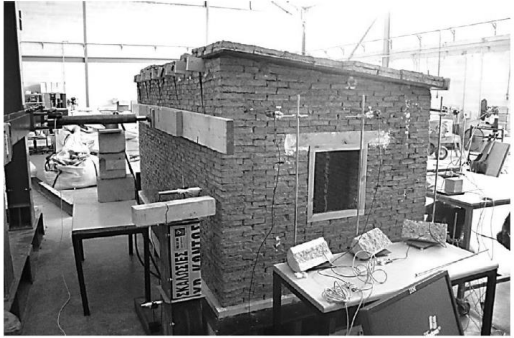
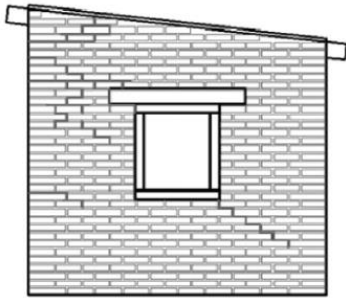
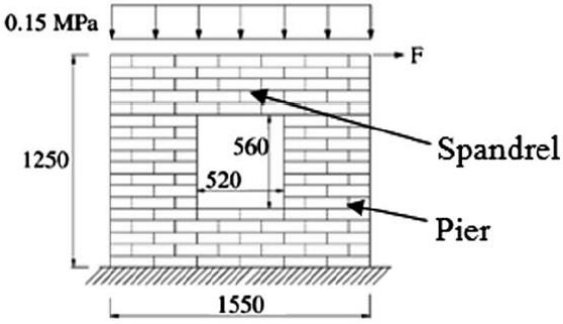
 	<ul style="list-style-type: none"> - Wall type: 1 - Wall ID: E9 - Axial stress ratio: Low - Material type: Adobe brick - Damage Pattern: Diagonal tension crack - Reference: Illampas et al. (2014)
	<ul style="list-style-type: none"> - Wall type: 1 - Wall ID: E10 - Axial stress ratio: Low - Material type: Clay brick - Damage Pattern: Diagonal tension crack - Reference: Akhaveissy (2013)

Table B.1 (continued)

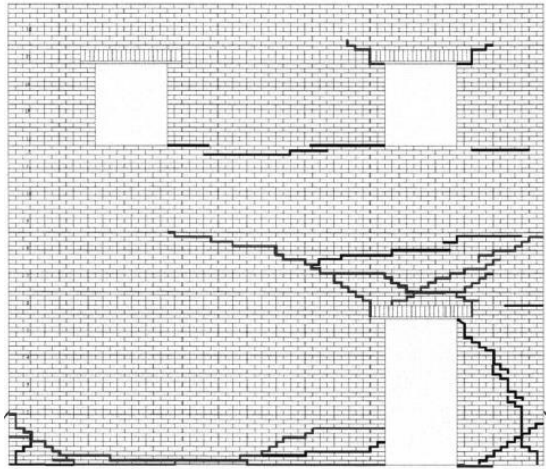
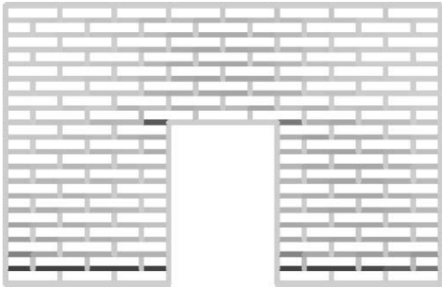
	<ul style="list-style-type: none"> - Wall type: 2 - Wall ID: E11 - Axial stress ratio: Medium - Material type: Solid clay brick - Damage Pattern: Sliding shear damage is observed at left pier ($\lambda < 1.0$). Flexural and diagonal tension cracks are observed at the pier ($\lambda > 2.0$). - Reference: Moon et al. (2005)
 <p style="text-align: center;">Fig. 24. Final damage map.</p>	<ul style="list-style-type: none"> - Wall type: 2 - Wall ID: E12 - Axial stress ratio: Low - Material type: Clay brick - Damage Pattern: Sliding shear damage is observed at piers ($\lambda < 1.0$). - Reference: Akhaveissy (2013)
	<ul style="list-style-type: none"> - Wall type: 3 - Wall ID: E13 - Axial stress ratio: Medium - Material type: Clay brick - Damage Pattern: Diagonal tension cracks are observed at middle and right piers. Flexural cracks dominate the left pier ($\lambda \gg 2.0$) - Reference: Benedetti et al. (1998)

Table B.1 (continued)

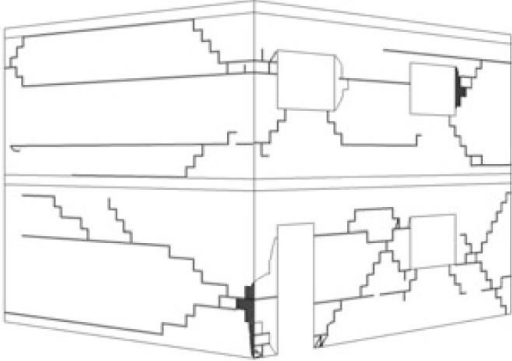
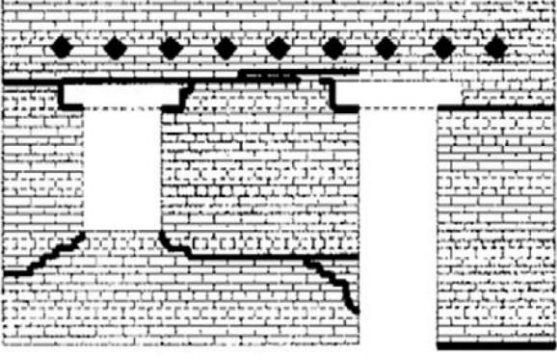
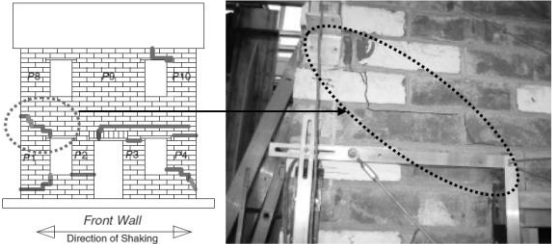
	<ul style="list-style-type: none"> - Wall type: 3 - Wall ID: E14 - Axial stress ratio: Medium - Material type: Concrete brick - Damage Pattern: Diagonal tension cracks and Flexural damage are observed at middle and right piers. Flexural damage dominates the left pier ($\lambda \gg 2.0$) - Reference: Lourenco et al. (2012)
	<ul style="list-style-type: none"> - Wall type: 3 - Wall ID: E14 - Axial stress ratio: Low - Material type: Clay brick - Failure mode: Diagonal tension cracks are observed at middle and left piers. Sliding shear damage dominates the right pier ($\lambda \gg 2.0$) - Reference: Akhaveissy (2013)
	<ul style="list-style-type: none"> - Wall type: 3 - Wall ID: E15 - Axial stress ratio: Low - Material type: Clay brick - Damage Pattern: Diagonal tension cracks are observed - Reference: Ali et al. (2007)

Table B.1 (continued)

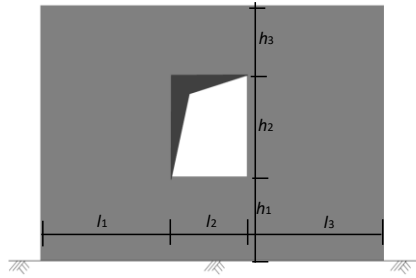
	<ul style="list-style-type: none"> - Wall type: 3,4 - Wall ID: E16 - Axial stress ratio: Medium, low - Material type: Clay brick - Damage Pattern: Diagonal tension cracks dominate the behavior - Reference: Benedetti et al. (1996)
	<ul style="list-style-type: none"> - Wall type: 3,4 - Wall ID: E17 - Axial stress ratio: Medium, low - Material type: Stone brick - Damage Pattern: Diagonal tension cracking is the dominant behavior mode at all piers. - Reference: Benedetti et al. (1996)
	<ul style="list-style-type: none"> - Wall type: 6 - Wall ID: E18 - Axial stress ratio: Low - Material type: Hollow clay brick - Damage Pattern: Diagonal tension cracks are observed - Reference: Bothara et al. (2010)

C. Ultimate Limit State Calculation Details

In Figure C.1 to Figure C.6, detailed ultimate lateral strength calculations according to FEMA 273 (1997), TBSC (2018) and Akhaveissy (2013) are presented for each wall ID E1 ~ E6. Calculations are based on the equations that are presented in Section 3.4.

A.

MASONRY WALL TYPE-1 LIMIT STRENGTH CALCULATIONS



Geometric Properties

l1	710 mm
l2	520 mm
l3	710 mm
h1	490 mm
h2	470 mm
h3	470 mm
thickness	50 mm

Loading Properties

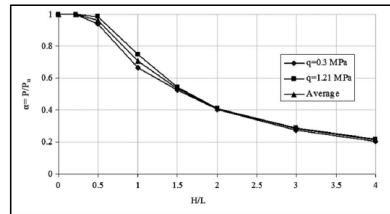
Vert	0.425 Mpa
Hor	10.5 kN

Masonry location **Single Story**

Mechanical Properties

Cohesion of mortar (C)	0.12 Mpa
internal friction of mortar (φ)	40 °
Compressive Strength (fc)	3.89 Mpa
Tensile Strength(ft)	0.35 Mpa

Limit Strength Calculation-1 (According to A.H. Akhaveissy)



Pier 1 (h/l)	1.16	-->	α_1	0.53
Pier 2 (h/l)	1.16	-->	α_2	0.53

Formulas	Pier - 1	Pier-2
$\tau_U = C + \sigma_0 \tan(\varphi)$	0.477 Mpa	0.477 Mpa
$\theta = 0.5 \times \tan^{-1} \left(\frac{2\tau_U}{\sigma_0} \right)$	33.0 °	33.0 °
$x_{min} = \min \left\{ \begin{array}{l} L \times \tan(\theta) \\ (1 - \tan(\theta)) \times h \end{array} \right.$	461 mm 290 mm	461 mm 290 mm
$P_U = \tau_U \times L \times t + F_t \times t \times x_{min}$	22 kN	22 kN
$P = 0.88\alpha P_U$	10 kN	10 kN
$V_{des.} = (k_i/k_t) * V_{Hor}$	5 kN	5 kN

B. MASONRY WALL TYPE-1 LIMIT STRENGTH CALCULATIONS

Limit Strength Calculation-2 (FEMA 273)

Formulas	Pier - 1	Pier-2
$v_{me} = \frac{0.75}{1.5}(C + f_a \tan \phi)$	0.24 Mpa	0.24 Mpa
A_n	35500 mm ²	35500 mm ²
$P_{CE} = f_a A_n$	15 kN	15 kN
$V_{bjs} = A_n \times v_{me}$	8 kN	8 kN
$V_r = 0.9 \alpha P_{CE} \left(\frac{L}{h_{eff}} \right)$	6 kN	6 kN
$V_{dt} = v_{me} A_n \beta \sqrt{\left(1 + \frac{f_a}{v_{me}} \right)}$	12 kN	12 kN
$V_{tc} = \alpha P_{CE} \left(\frac{L}{h_{eff}} \right) \left(1 - \frac{f_a}{0.7 \times f'_{me}} \right)$	5 kN	5 kN
$V_{des.} = (k_i/k_t) * V_{Hor}$	5 kN	5 kN

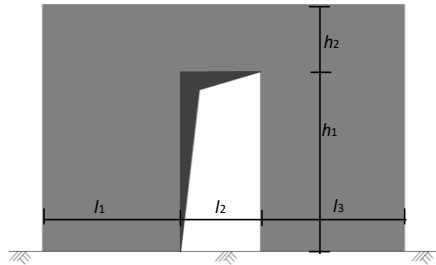
Limit Strength Calculation-3 (TBSC 2018)

Formulas	Pier - 1	Pier-2
$f_{vk} = f_{vko} + 0.4\sigma$	0.52 Mpa	0.52 Mpa
$V_{des.} = (k_i/k_t) * V_{Hor}$	5 kN	5 kN
$M_d = (P_d * h_i)$	4 kNm	4 kNm
$e_{cc} = (M_d / (P_{CE} + selfweight))$	0.28 m	0.28 m
l_{comp}	233 mm	233 mm
A_n	11643 mm ²	11643 mm ²
$V_{cr} = (A_n) * f_{vk}$	6 kN	6 kN

Figure C.1. Wall Type-1 Limit Strength Calculations

A.

MASONRY WALL TYPE-2 LIMIT STRENGTH CALCULATIONS



Masonry location Intermediate Story

Geometric Properties

l1	780 mm
l2	520 mm
l3	780 mm
h1	770 mm
h2	550 mm
thickness	120 mm

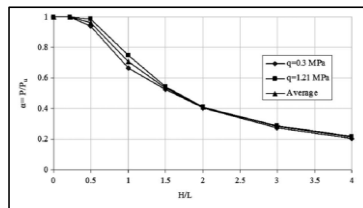
Loading Properties

Vert	0.15 Mpa
Hor	11.5 kN

Mechanical Properties

Cohesion of mortar (C)	0.12 Mpa
internal friction of mortar (φ)	30°
Compressive Strength (fc)	3.33 Mpa
Tensile Strength(ft)	0.40 Mpa

Limit Strength Calculation-1 (According to A.H. Akhveissy)



Pier 1 (h/l)	1.24	-->	α_1	0.50
Pier 2 (h/l)	1.24	-->	α_2	0.50

Formulas	Pier - 1	Pier-2
$\tau_U = C + \sigma_0 \tan(\varphi)$	0.207 Mpa	0.207 Mpa
$\theta = 0.5 \times \tan^{-1} \left(\frac{2\tau_U}{\sigma_0} \right)$	35.0°	35.0°
$x_{\min} = \min \left\{ \begin{array}{l} L \times \tan(\theta) \\ (1 - \tan(\theta)) \times h \end{array} \right.$	547 mm 289 mm	547 mm 289 mm
$P_U = \tau_U \times L \times t + F_t \times t \times x_{\min}$	33 kN	33 kN
$P = 0.88\alpha P_U$	15 kN	15 kN
$V_{des.} = (k_i/k_t) * V_{Hor}$	6 kN	5.75 kN

B.

MASONRY WALL TYPE-2 LIMIT STRENGTH CALCULATIONS**Limit Strength Calculation-2 (FEMA 273)**

Formulas	Pier - 1	Pier-2
$v_{me} = \frac{0.75}{1.5}(C + f_a \tan \phi)$	0.10 Mpa	0.10 Mpa
A_n	93600 mm ²	93600 mm ²
$P_{CE} = f_a A_n$	14 kN	14 kN
$V_{bjs} = A_n \times v_{me}$	10 kN	10 kN
$V_r = 0.9\alpha P_{CE} \left(\frac{L}{h_{eff}} \right)$	10 kN	10 kN
$V_{dt} = v_{me} A_n \beta \sqrt{\left(1 + \frac{f_a}{v_{me}} \right)}$	12 kN	12 kN
$V_{tc} = \alpha P_{CE} \left(\frac{L}{h_{eff}} \right) \left(1 - \frac{f_a}{0.7 \times f'_{me}} \right)$	11 kN	11 kN
$V_{des.} = (k_i/k_t) * V_{Hor}$	6 kN	5.75 kN

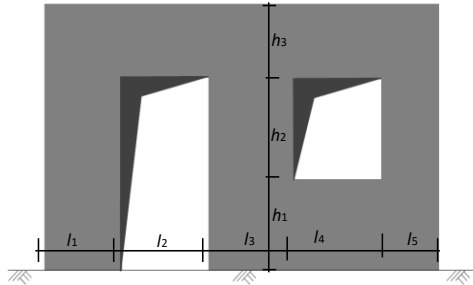
Limit Strength Calculation-3 (TBSC 2018)

Formulas	Pier - 1	Pier-2
$f_{vk} = f_{vko} + 0.4\sigma$	0.46 Mpa	0.46 Mpa
$V_{des.} = (k_i/k_t) * V_{Hor}$	6 kN	5.75 kN
$M_d = (P_d * h_i)$	6 kNm	6 kNm
$e_{cc} = (M_d / (P_{CE} + selfweight))$	0.35 m	0.35 m
l_{comp}	107 mm	107 mm
A_n	12890 mm ²	12890 mm ²

Figure C.2. Wall Type-2 Limit Strength Calculations

A.

MASONRY WALL TYPE-3 LIMIT STRENGTH CALCULATIONS



Masonry location **Single Story**

Geometric Properties

l1	880 mm
l2	610 mm
l3	1410 mm
l4	610 mm
l5	580 mm
h1	890 mm
h2	950 mm
h3	630 mm
thickness	190 mm

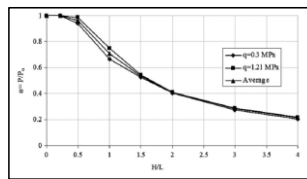
Mechanical Properties

Cohesion of mortar (C)	0.12 Mpa
internal friction of mortar (φ)	15 °
Masonry Compressive Strength (f_c)	12.78 Mpa
Tensile Strength(f_t)	0.18 Mpa

Loading Properties

Vert	0.0335 Mpa
Hor	9 kN

Limit Strength Calculation-1 (According to A.H. Akhaveissy)



Pier 1 (h/l)	2.34	-->	α_1	0.07
Pier 2 (h/l)	0.92	-->	α_2	0.46
Pier 3 (h/l)	2.14	-->	α_3	0.11

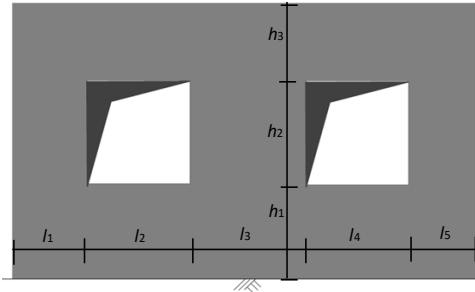
Formulas	Pier - 1	Pier-2	Pier-3
$\tau_U = C + \sigma_0 \tan(\varphi)$	0.129 Mpa	0.129 Mpa	0.129 Mpa
$\theta = 0.5 \times \tan^{-1} \left(\frac{2\tau_U}{\sigma_0} \right)$	41.3 °	41.3 °	41.3 °
$x_{min} = \min \left\{ \begin{array}{l} L \times \tan(\theta) \\ (1 - \tan(\theta)) \times h \end{array} \right.$	773 mm 250 mm	1239 mm 158 mm	510 mm 151 mm
$P_U = \tau_U \times L \times t + F_t \times t \times x_{min}$	30 kN	40 kN	19 kN
$P = 0.88\alpha P_U$	2 kN	16 kN	2 kN
$V_{des.} = (k_i/k_t) * V_{Hor}$	1 kN	7 kN	1 kN

B. MASONRY WALL TYPE-3 LIMIT STRENGTH CALCULATIONS			
Limit Strength Calculation-2 (FEMA 273)			
Formulas	Pier - 1	Pier-2	Pier-3
$v_{me} = \frac{0.75}{1.5}(C + f_a \tan \phi)$	0.06 Mpa	0.06 Mpa	0.06 Mpa
A_n	167200 mm ²	267900 mm ²	110200 mm ²
$P_{CE} = f_a A_n$	6 kN	9 kN	4 kN
$V_{bjs} = A_n \times v_{me}$	11 kN	17 kN	7 kN
$V_r = 0.9 \alpha P_{CE} \left(\frac{L}{h_{eff}} \right)$	1 kN	4 kN	1 kN
$V_{dt} = v_{me} A_n \beta \sqrt{\left(1 + \frac{f_a}{v_{me}} \right)}$	6 kN	23 kN	4 kN
$V_{tc} = \alpha P_{CE} \left(\frac{L}{h_{eff}} \right) \left(1 - \frac{f_a}{0.7 \times f'_{me}} \right)$	1 kN	5 kN	1 kN
$V_{des.} = (k_i / k_t) * V_{Hor}$	1 kN	7 kN	1 kN
Limit Strength Calculation-3 (TBSC 2018)			
Formulas	Pier - 1	Pier-2	Pier-3
$f_{vk} = f_{vko} + 0.4\sigma$	0.19 Mpa	0.19 Mpa	0.19 Mpa
$V_{des.} = (k_i / k_t) * V_{Hor}$	1 kN	7 kN	1 kN
$M_d = (P_d * h_i)$	2 kNm	10 kNm	1 kNm
$e_{cc} = (M_d / (P_{CE} + selfweight))$	0.13 m	0.62 m	0.19 m
l_{comp}	880 mm	244 mm	295 mm
A_n	167200 mm ²	46267 mm ²	55991 mm ²
$V_{cr} = (A_n) * f_{vk}$	32 kN	9 kN	11 kN

Figure C.3. Wall Type-3 Limit Strength Calculations

A.

MASONRY WALL TYPE-4 LIMIT STRENGTH CALCULATIONS



Masonry location **Single Story**

Geometric Properties

l1	450 mm
l2	600 mm
l3	650 mm
l4	600 mm
l5	450 mm
h1	450 mm
h2	700 mm
h3	0 mm
thickness	245 mm

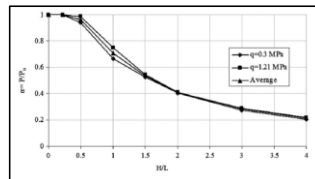
Mechanical Properties

Cohesion of mortar (C)	0.25 Mpa
internal friction of mortar (ϕ)	30 °
Compressive Strength (fc)	2.79 Mpa
Tensile Strength(ft)	0.18 Mpa

Loading Properties

Vert	0.212 Mpa
Hor	22.5 kN

Limit Strength Calculation-1 (According to A.H. Akhveissy)



Pier 1 (h/l)	1.81	-->	α_1	0.47
Pier 2 (h/l)	1.08	-->	α_2	0.69
Pier 3 (h/l)	1.56	-->	α_3	0.54

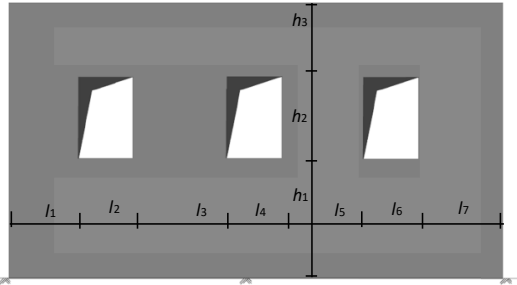
Formulas	Pier - 1	Pier-2	Pier-3
$\tau_U = C + \sigma_0 \tan(\phi)$	0.372 Mpa	0.372 Mpa	0.372 Mpa
$\theta = 0.5 \times \tan^{-1} \left(\frac{2\tau_U}{\sigma_0} \right)$	37.1 °	37.1 °	37.1 °
$x_{min} = \min \left\{ \begin{array}{l} L \times \tan(\theta) \\ (1 - \tan(\theta)) \times h \end{array} \right.$	340 mm 199 mm	491 mm 171 mm	340 mm 171 mm
$P_U = \tau_U \times L \times t + F_t \times t \times x_{min}$	50 kN	67 kN	49 kN
$P = 0.88\alpha P_U$	21 kN	41 kN	23 kN
$V_{des.} = (k_i/k_t) * V_{Hor}$	5.9 kN	9.8 kN	6.8 kN

B. MASONRY WALL TYPE-4 LIMIT STRENGTH CALCULATIONS			
Limit Strength Calculation-2 (FEMA 273)			
Formulas	Pier - 1	Pier-2	Pier-3
$v_{me} = \frac{0.75}{1.5}(C + f_a \tan \phi)$	0.19 Mpa	0.19 Mpa	0.19 Mpa
A_n	110250 mm ²	159250 mm ²	110250 mm ²
$P_{CE} = f_a A_n$	23 kN	34 kN	23 kN
$V_{bjs} = A_n \times v_{me}$	21 kN	30 kN	21 kN
$V_r = 0.9 \alpha P_{CE} \left(\frac{L}{h_{eff}} \right)$	6 kN	14 kN	7 kN
$V_{dt} = v_{me} A_n \beta \sqrt{\left(1 + \frac{f_a}{v_{me}} \right)}$	17 kN	40 kN	19 kN
$V_{ic} = \alpha P_{CE} \left(\frac{L}{h_{eff}} \right) \left(1 - \frac{f_a}{0.7 \times f'_{me}} \right)$	6 kN	14 kN	7 kN
$V_{des.} = (k_i/k_t) * V_{Hor}$	4 kN	13 kN	6 kN
Limit Strength Calculation-3 (TBSC 2018)			
Formulas	Pier - 1	Pier-2	Pier-3
$f_{vk} = f_{vko} + 0.4\sigma$	0.26 Mpa	0.26 Mpa	0.26 Mpa
$V_{des.} = (k_i/k_t) * V_{Hor}$	4 kN	13 kN	6 kN
$M_d = (P_d * h_i)$	3 kNm	9 kNm	4 kNm
$e_{cc} = (M_d / (P_{CE} + selfweight))$	0.12 m	0.26 m	0.16 m
l_{comp}	308 mm	198 mm	207 mm
A_n	75577 mm ²	48622 mm ²	50748 mm ²
$V_{cr} = (A_n) * f_{vk}$	20 kN	13 kN	13 kN

Figure C.4. Wall Type-4 Limit Strength Calculations

A.

MASONRY WALL TYPE-5 LIMIT STRENGTH CALCULATIONS



Masonry location **Top Story**

Geometric Properties

l1	1240 mm
l2	1050 mm
l3	1030 mm
l4	880 mm
l5	1030 mm
l6	1050 mm
l7	1240 mm
h1	1070 mm
h2	1200 mm
h3	1110 mm
thickness	305 mm

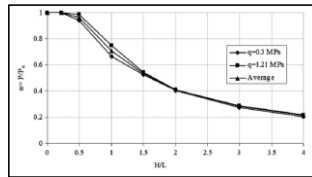
Mechanical Properties

Cohesion of mortar (C)	0.25 Mpa
internal friction of mortar (ϕ)	30 °
Compressive Strength (fc)	2.68 Mpa
Tensile Strength(ft)	0.13 Mpa

Loading Properties

Vert	0.016 Mpa
Hor	15 kN

Limit Strength Calculation-1 (According to A.H. Akhaveissy)



Pier 1 (h/l)	1.47	-->	α_1	0.48
Pier 2 (h/l)	1.17	-->	α_2	0.58
Pier 3 (h/l)	1.17	-->	α_3	0.58
Pier 4 (h/l)	1.73	-->	α_4	0.41

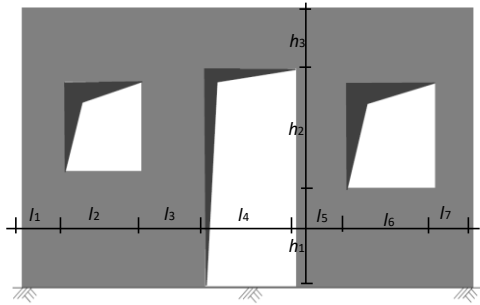
Formulas	Pier- 1	Pier-2	Pier-3	Pier-4	Units
$\tau_U = C + \sigma_0 \tan(\phi)$	0.259	0.259	0.259	0.259	Mpa
$\theta = 0.5 \times \tan^{-1} \left(\frac{2\tau_U}{\sigma_0} \right)$	44.1	44.1	44.1	44.1	°
$x_{min} = \min \left\{ \begin{array}{l} L \times \tan(\theta) \\ (1 - \tan(\theta)) \times h \end{array} \right.$	1202 55	999 36	999 36	1202 55	mm mm
$P_U = \tau_U \times L \times t + F_i \times t \times x_{min}$	100	83	83	100	kN
$P = 0.88\alpha P_U$	43	42	42	36	kN
$V_{des.} = (k_i/k_t) * V_{Hor}$	2.7	4.8	4.8	2.7	kN

B. MASONRY WALL TYPE-5 LIMIT STRENGTH CALCULATIONS					
Limit Strength Calculation-2 (FEMA 273)					
Formulas	Pier - 1	Pier-2	Pier-3	Pier-4	Units
$v_{me} = \frac{0.75}{1.5}(C + f_a \tan \phi)$	0.13	0.13	0.13	0.13	Mpa
A_n	378200	314150	314150	378200	mm ²
$P_{CE} = f_a A_n$	6	5	5	6	kN
$V_{bjs} = A_n \times v_{me}$	49	41	41	49	kN
$V_r = 0.9 \alpha P_{CE} \left(\frac{L}{h_{eff}} \right)$	2	2	2	2	kN
$V_{dt} = v_{me} A_n \beta \sqrt{\left(1 + \frac{f_a}{v_{me}} \right)}$	35	37	37	30	kN
$V_{tc} = \alpha P_{CE} \left(\frac{L}{h_{eff}} \right) \left(1 - \frac{f_a}{0.7 \times f'_{me}} \right)$	2	2	2	2	kN
$V_{des.} = (k_i/k_t) * V_{Hor}$	3	5	5	3	kN
Limit Strength Calculation-3 (TBSC 2018)					
Formulas	Pier - 1	Pier-2	Pier-3	Pier-4	Units
$f_{vk} = f_{vko} + 0.4\sigma$	0.14	0.14	0.14	0.14	Mpa
$V_{des.} = (k_i/k_t) * V_{Hor}$	3	5	5	3	kN
$M_d = (P_d * h_i)$	5	6	6	5	kNm
$e_{cc} = (M_d / (P_{CE} + selfweight))$	0.27	0.48	0.48	0.27	m
l_{comp}	1048	95	95	1048	mm
A_n	319777	28847	28847	319777	mm ²
$V_{cr} = (A_n) * f_{vk}$	44	4	4	44	kN

Figure C.5. Wall Type-5 Limit Strength Calculations

A.

MASONRY WALL TYPE-6 LIMIT STRENGTH CALCULATIONS



Masonry location **Top Story**

Geometric Properties

l1	470 mm
l2	370 mm
l3	400 mm
l4	620 mm
l5	400 mm
l6	370 mm
l7	470 mm
h1	1090 mm
h2	930 mm
h3	680 mm
thickness	205 mm

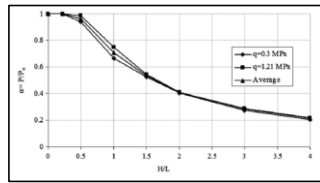
Mechanical Properties

Cohesion of mortar (C)	0.25 Mpa
internal friction of mortar (φ)	40°
Masonry Compressive Strength (fc)	7.68 Mpa
Tensile Strength(ft)	0.18 Mpa

Loading Properties

Vert	0.034 Mpa
Hor	3 kN

Limit Strength Calculation-1 (According to A.H. Akhaveissy)



Pier 1 (h/l)	2.48	-->	α_1	0.40
Pier 2 (h/l)	2.58	-->	α_2	0.38
Pier 3 (h/l)	2.58	-->	α_3	0.38
Pier 4 (h/l)	3.15	-->	α_4	0.31

Formulas	Pier - 1	Pier-2	Pier-3	Pier-4	Units
$\tau_U = C + \sigma_0 \tan(\varphi)$	0.279	0.279	0.279	0.279	Mpa
$\theta = 0.5 \times \tan^{-1} \left(\frac{2\tau_U}{\sigma_0} \right)$	43.3	43.3	43.3	43.3	°
$x_{min} = \min \left\{ \begin{array}{l} L \times \tan(\theta) \\ (1 - \tan(\theta)) \times h \end{array} \right.$	442 69	376 61	376 61	442 69	mm mm
$P_U = \tau_U \times L \times t + F_t \times t \times x_{min}$	29	25	25	29	kN
$P = 0.88\alpha P_U$	10	8	8	8	kN
$V_{des.} = (k_i/k_t) * V_{Hor}$	0.8	0.7	0.7	0.8	kN

B. MASONRY WALL TYPE-6 LIMIT STRENGTH CALCULATIONS					
Limit Strength Calculation-2 (FEMA 273)					
Formulas	Pier - 1	Pier-2	Pier-3	Pier-4	Units
$v_{me} = \frac{0.75}{1.5}(C + f_a \tan \phi)$	0.14	0.14	0.14	0.14	Mpa
A_n	96350	82000	82000	96350	mm ²
$P_{CE} = f_a A_n$	3	3	3	3	kN
$V_{bjs} = A_n \times v_{me}$	13	11	11	13	kN
$V_r = 0.9 \alpha P_{CE} \left(\frac{L}{h_{eff}} \right)$	0.6	0.5	0.5	0.5	kN
$V_{dt} = v_{me} A_n \beta \sqrt{\left(1 + \frac{f_a}{v_{me}} \right)}$	6	5	5	5	kN
$V_{tc} = \alpha P_{CE} \left(\frac{L}{h_{eff}} \right) \left(1 - \frac{f_a}{0.7 \times f'_{me}} \right)$	0.7	0.5	0.5	0.5	kN
$V_{des.} = (k_i/k_t) * V_{Hor}$	0.8	0.7	0.7	0.8	kN
Limit Strength Calculation-3 (TBSC 2018)					
Formulas	Pier - 1	Pier-2	Pier-3	Pier-4	Units
$f_{vk} = f_{vko} + 0.4\sigma$	0.20	0.20	0.20	0.20	Mpa
$V_{des.} = (k_i/k_t) * V_{Hor}$	1	1	1	1	kN
$M_d = (P_d * h_i)$	1	1	1	1	kNm
$e_{cc} = (M_d / (P_{CE} + selfweight))$	0.17	0.17	0.17	0.17	m
l_{comp}	184	91	91	184	mm
A_n	37680	18583	18583	37680	mm ²
$V_{cr} = (A_n) * f_{vk}$	7	4	4	7	kN

Figure C.6. Wall Type-6 Limit Strength Calculations

D. Classification of the Field Observation Table

In the Appendix D, a classification Table D.1 is prepared based on the damage photographs of perforated URM walls presented in Section 2.2 and Appendix A. In the classification table material type, material quality, axial stress level, aspect ratios, damage descriptions and, failure mode of walls are given.

Table D.1. Classification Table for Site Post EQ Damage Observations

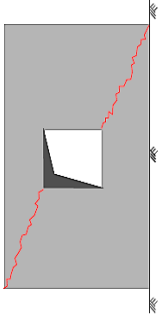
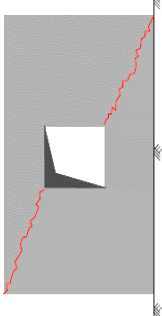
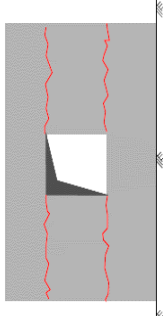
Wall ID	Wall Type	Material Type	Material Quality	Axial stress grade	Panel Aspect Ratio	Damaged Panel in Pier No.	Damage Description / Crack Location	Failure Mode	Damage Sketch
F1	1	Clay Brick	Low	Low	0.76	1	Cracks started from corner of the openings and propagated towards wall edge.	Diagonal Tension	
F2	1	Clay Brick	Low	Low	0.42	1	Cracks started from corner of the openings and propagated towards wall edge.	Diagonal Tension	
F2	1	Clay Brick	Low	Low	0.61	2	Sliding Cracks started from corner of the openings and propagated towards wall edge.	Sliding Shear	

Table D.1 (continued)

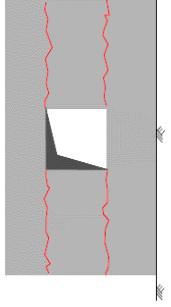
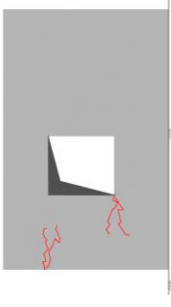
F3	1	Clay Brick	Low	Low	0.8	1	Sliding Cracks started from corner of the openings and propagated towards wall edge.	Sliding Shear	
F4	1	Stone	Moderate	Medium	2	1	Severe flexural failure is observed at pier.	Flexural (Toe crushing)	
F4	1	Adobe	Low	Low	2	2	Cracks started from corner of the openings and propagated towards wall edge. Additionally, Flexural failure is observed at pier.	Hybrid Failure (Diagonal Tension + Flexural (Toe crushing))	

Table D.1 (continued)

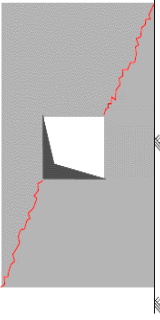
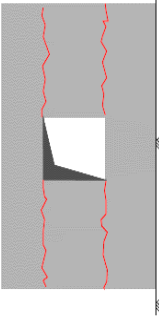
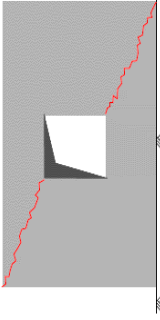
F5	1	Clay Brick	Moderate	Medium	1	1	Cracks starts from corner of the openings propagated through wall edges	Diagonal Tension	
F5	1	Clay Brick	Moderate	Low	1	2	Sliding Cracks started from corner of the openings and propagated towards wall edge.	Sliding Shear	
F6	1	Clay Brick	Moderate	Medium	1.14	1	Cracks started from corner of the openings and propagated towards wall edge.	Diagonal Tension	

Table D.1 (continued)

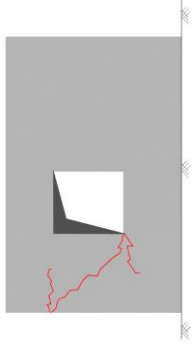
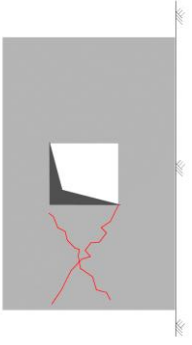
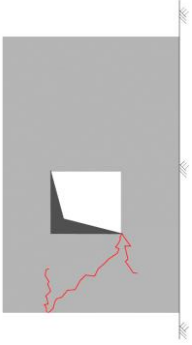
F7	1	AAC	Moderate	Medium	2.00	1	Cracks started from corner of the openings and propagated towards wall edge. Additionally, Flexural failure is observed at pier.	Hybrid Failure (Diagonal Tension + Flexural (Toe crushing))	
F7	1	AAC	Moderate	Medium	1.2	2	Cracks started from corner of the openings and propagated towards wall edge.	Diagonal Tension	
F7	1	AAC	Moderate	Medium	2.40	3	Cracks started from corner of the openings and propagated towards wall edge. Additionally, Flexural failure is observed at pier.	Hybrid Failure (Diagonal Tension + Flexural (Toe crushing))	

Table D.1 (continued)

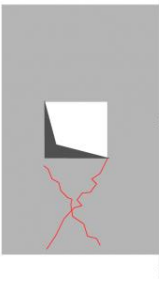
F8	1	Clay Brick	Low	Medium	0.75	1	Cracks started from corner of the openings and propagated towards wall edge.	Diagonal Tension	
F9	1	Stone	Moderate	Low	1.4	1	Cracks started from corner of the openings and propagated towards wall edge.	Diagonal Tension	
F10	1	Clay Brick	Low	Low	2.42	1	Cracks started from corner of the openings and propagated towards wall edge. Additionally, Flexural failure is observed at pier.	Hybrid Failure (Diagonal Tension + Flexural (Toe crushing))	

Table D.1 (continued)

F11	1	Clay Brick	Moderate	Low	0.44	1	Cracks started from corner of the openings and propagated towards wall edge.	Diagonal Tension	
F12	1	Clay Brick	Moderate	Low	0.50	1	Cracks started from corner of the openings and propagated towards wall edge.	Diagonal Tension	
F13	1	Clay Brick	Moderate	Low	1.00	1	Cracks started from corner of the openings and propagated towards wall edge.	Diagonal Tension	

Table D.1 (continued)

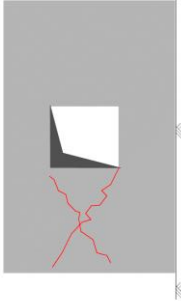
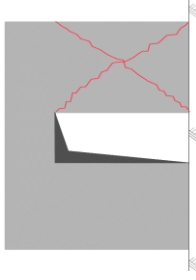
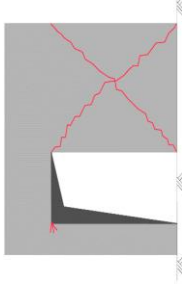
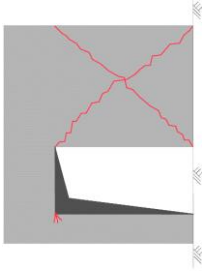
F14	1	Clay Brick	Low	Low	1.00	1	Cracks started from corner of the openings and propagated towards wall edge.	Diagonal Tension	
F15	2	Clay Brick	Moderate	Medium	1.14	1	Cracks started from corner of the openings and propagated towards wall edge.	Diagonal Tension	
F16	2	Clay Brick	Moderate	Medium	1.48	1	Cracks started from corner of the openings and propagated towards wall edge.	Diagonal Tension	
F16	2	Clay Brick	Moderate	Medium	10.00	2	Severe flexural failure is observed at pier.	Flexural (Toe crushing)	

Table D.1 (continued)

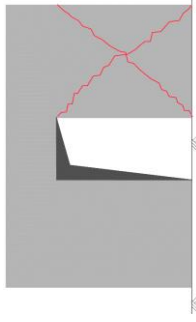
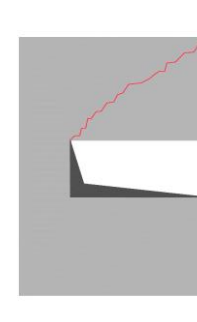
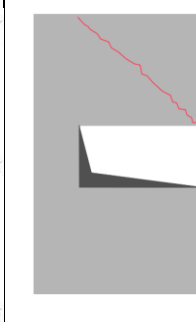
F17	2	Stone	Low	High	0.79	1	Cracks started from corner of the openings and propagated towards wall edge.	Diagonal Tension	
F18	2	Clay Brick	Low	Low	1.40	1	Cracks started from corner of the openings and propagated towards wall edge.	Diagonal Tension	
F18	2	Clay Brick	Low	Low	1.00	2	Cracks started from corner of the openings and propagated towards wall edge.	Diagonal Tension	
F19	2	Adobe	Low	Low	0.7	1	Cracks started from corner of the openings and propagated towards wall edge.	Diagonal Tension	

Table D.1 (continued)

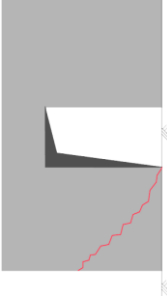
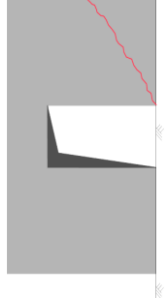
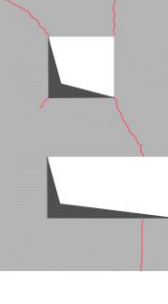
F20	2	Clay Brick	Low	Low	1.2	1	Cracks started from corner of the openings and propagated towards wall edge.	Diagonal Tension	
F20	2	Clay Brick	Low	Medium	1.2	2	Cracks started from corner of the openings and propagated towards wall edge.	Diagonal Tension	
F21	2	Clay Brick	Low	Low	0.9	1	Cracks started from corner of the openings and propagated towards wall edge.	Diagonal Tension	
F22	3	Clay Brick	Low	Low	1.00	1	Sliding Cracks started from corner of the openings and propagated towards wall edge.	Sliding Shear	

Table D.1 (continued)

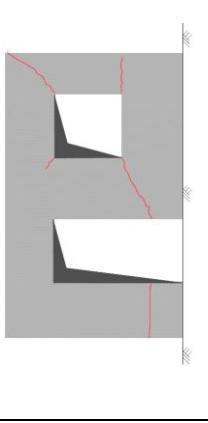
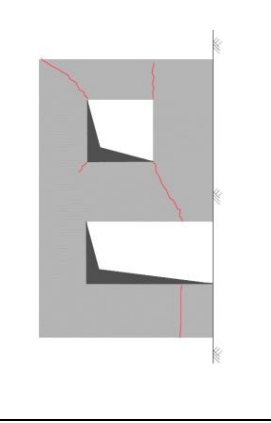
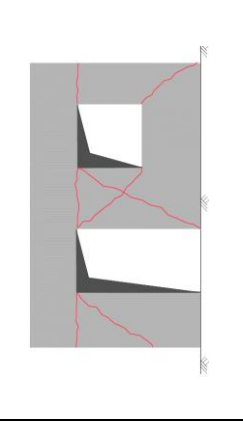
F22	3	Clay Brick	Low	Low	1.17	2a	Cracks started from corner of the openings and propagated towards adjacent opening corner.	Diagonal Tension	
F22	3	Clay Brick	Low	Low	0.58	2b	Sliding Cracks started from corner of the openings and propagated towards adjacent opening corner. Additionally, Diagonal tension is observed at pier.	Hybrid Failure (Diagonal Tension + Sliding Shear)	
F23	3	Clay Brick	Low	Low	1.50	1	Sliding Cracks started from corner of the openings and propagated towards wall edge. Additionally, Diagonal tension is observed at pier.	Hybrid Failure (Diagonal Tension + Sliding Shear)	

Table D.1 (continued)

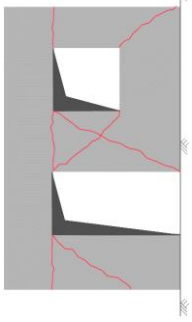
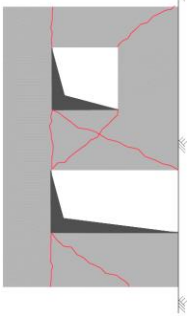
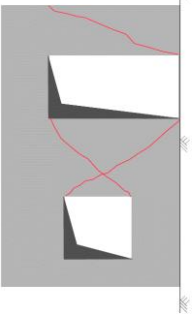
F23	3	Clay Brick	Low	Low	1.42	2	Sliding Cracks started from corner of the openings and propagated towards adjacent opening corner. Additionally, Diagonal tension is observed at pier.	Hybrid Failure (Diagonal Tension + Sliding Shear)	
F23	3	Clay Brick	Low	Low	2.60	3	Cracks started from corner of the openings and propagated towards wall edge. Additionally, Flexural failure is observed at pier.	Hybrid Failure (Diagonal Tension + Flexural (Toe crushing))	
F24	3	Clay Brick	Moderate	High	0.57	1	Cracks started from corner of the openings and propagated towards adjacent opening corner.	Diagonal Tension	

Table D.1 (continued)

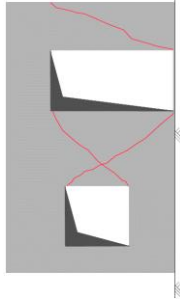
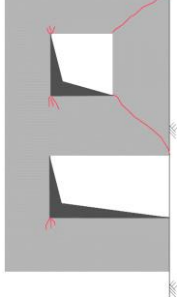
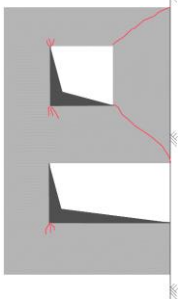
F24	3	Clay Brick	Moderate	High	1.00	2	Cracks started from corner of the openings and propagated towards wall edge.	Diagonal Tension	
F25	3	Adobe	Low	Low	2.5	1	Flexural failure is observed at pier.	Flexural (Toe crushing)	
F25	3	Adobe	Low	Low	2.5	2	Cracks started from corner of the openings and propagated towards adjacent opening corner. Additionally, Flexural failure is observed at pier.	Hybrid Failure (Diagonal Tension + Flexural (Toe crushing))	

Table D.1 (continued)

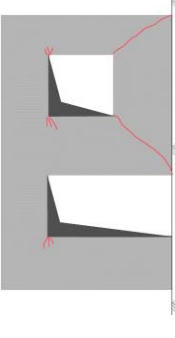
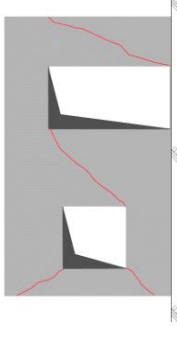
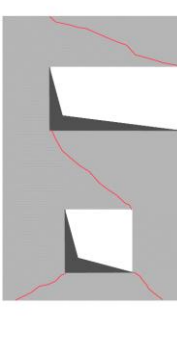
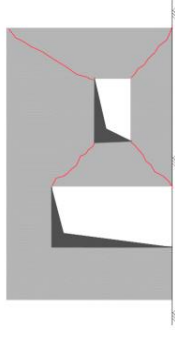
F25	3	Adobe	Low	Low	1.1	3	Cracks started from corner of the openings and propagated towards wall edge.	Diagonal Tension	
F26	3	Clay Brick	Low	Low	0.88	1	Cracks started from corner of the openings and propagated towards wall edge.	Diagonal Tension	
F26	3	Clay Brick	Low	Low	1.33	2	Cracks started from corner of the openings and propagated towards adjacent opening corner.	Diagonal Tension	
F27	3	Clay Brick	Low	Low	1.25	1	Cracks started from corner of the openings and propagated towards adjacent opening corner.	Diagonal Tension	

Table D.1 (continued)

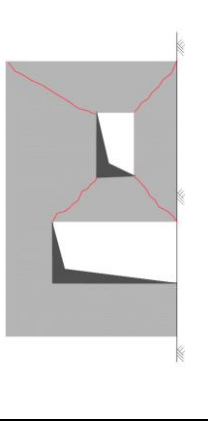
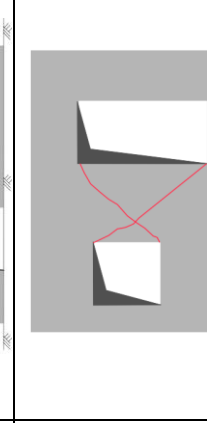
F27	3	Clay Brick	Low	Low	0.70	2	Cracks started from corner of the openings and propagated towards wall edge.	Diagonal Tension	
F28	3	Clay Brick	Low	Low	0.32	1	Cracks started from corner of the openings and propagated towards adjacent opening corner.	Diagonal Tension	
F29	3	Clay Brick	Low	Low	1.00	1	Cracks started from corner of the openings and propagated towards wall edge.	Diagonal Tension	
F30	3	Clay Brick	Low	Low	0.60	1	Cracks started from corner of the openings and propagated towards adjacent opening corner.	Diagonal Tension	

Table D.1 (continued)

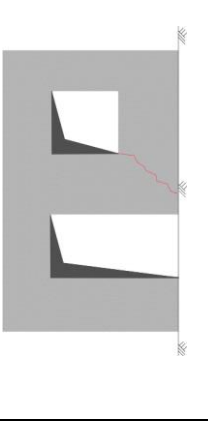
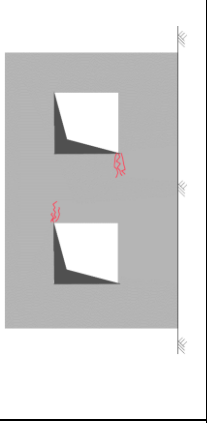
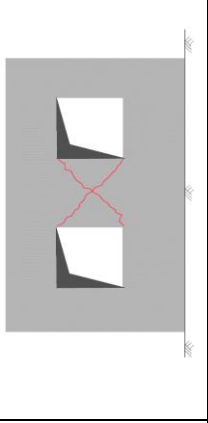
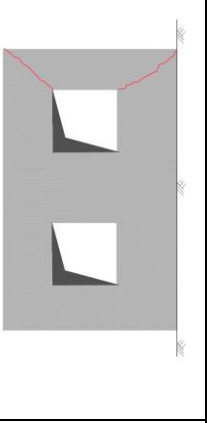
F31	3	Clay Brick	Low	Low	0.43	1	Cracks started from corner of the openings and propagated towards adjacent opening corner.	Diagonal Tension	
F32	4	Stone	Low	Low	1.88	1	Flexural failure is observed at pier.	Flexural (Toe crushing)	
F32	4	Stone	Low	Low	1.00	2	Cracks started from corner of the openings and propagated towards adjacent opening corner.	Diagonal Tension	
F32	4	Stone	Low	Low	0.70	3	Cracks started from corner of the openings and propagated towards wall edge.	Diagonal Tension	

Table D.1 (continued)

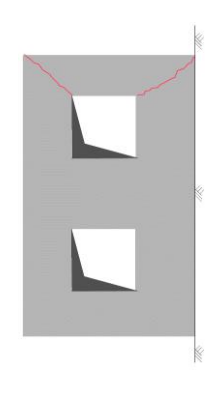
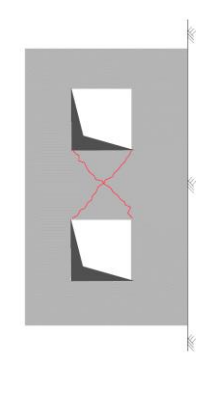
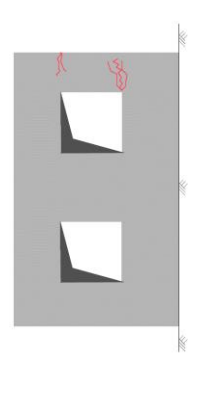
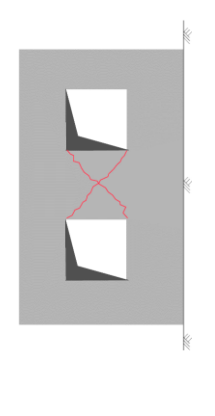
F33	4	Stone	Low	Low	1.20	1	Cracks started from corner of the openings and propagated towards wall edge.	Diagonal Tension	
F34	4	Clay Brick	Moderate	Medium	1.5	1	Cracks started from corner of the openings and propagated towards adjacent opening corner.	Diagonal Tension	
F34	4	Clay Brick	Moderate	Medium	3	2	Flexural failure is observed at pier.	Flexural (Toe crushing)	
F35	4	Clay Brick	Moderate	Medium	1.11	1	Cracks started from corner of the openings and propagated towards adjacent opening corner.	Diagonal Tension	

Table D.1 (continued)

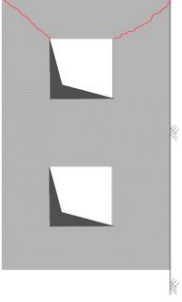
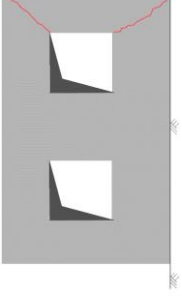
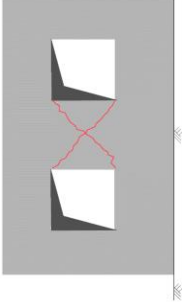
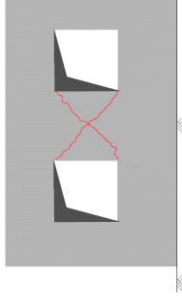
F36	4	Clay Brick	Low	Low	1.00	1a	Cracks started from corner of the openings and propagated towards wall edge.	Diagonal Tension	
F36	4	Clay Brick	Low	Low	0.75	1b	Cracks started from corner of the openings and propagated towards wall edge.	Diagonal Tension	
F37	4	Clay Brick	Moderate	Low	0.75	1	Cracks started from corner of the openings and propagated towards adjacent opening corner.	Diagonal Tension	
F38	4	Clay Brick	Low	Low	0.45	1	Cracks started from corner of the openings and propagated towards adjacent opening corner.	Diagonal Tension	

Table D.1 (continued)

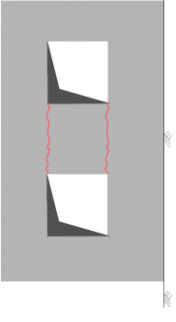
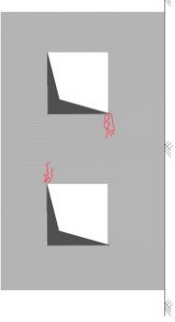
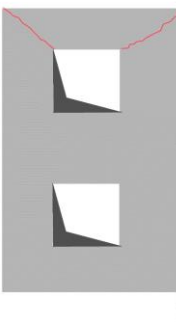
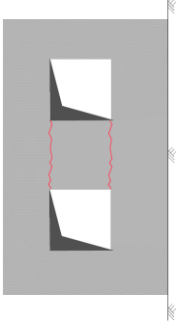
F39	4	Clay Brick	Moderate	Low	1.00	1	Sliding cracks started from corner of the openings and propagated towards adjacent opening corner.	Sliding Shear	
F40	4	Adobe	Low	Low	1.67	1a	Flexural failure is observed at pier.	Flexural (Toe crushing)	
F40	4	Adobe	Low	Low	1.00	1b	Cracks started from corner of the openings and propagated towards wall edge.	Diagonal Tension	
F41	4	Clay Brick	Low	Low	4.00	1a	Flexural failure is observed at pier.	Flexural (Toe crushing)	

Table D.1 (continued)

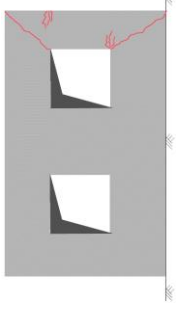
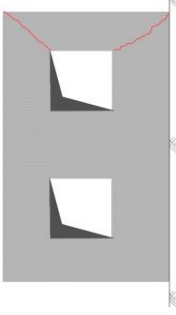
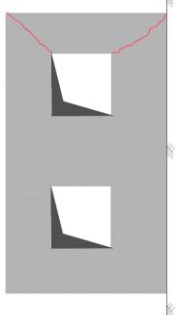
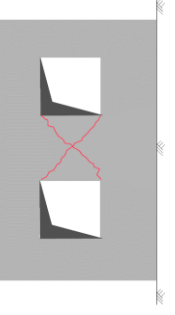
F41	4	Clay Brick	Low	Low	1.71	1b	Cracks started from corner of the openings and propagated towards wall edge.	Diagonal Tension	
F42	4	Clay Brick	Low	Low	0.67	1	Cracks started from corner of the openings and propagated towards wall edge.	Diagonal Tension	
F43	4	Clay Brick	Moderate	High	0.91	1a	Cracks started from corner of the openings and propagated towards adjacent opening corner.	Diagonal Tension	
F43	4	Clay Brick	Moderate	High	1.00	1b	Cracks started from corner of the openings and propagated towards wall edge.	Diagonal Tension	

Table D.1 (continued)

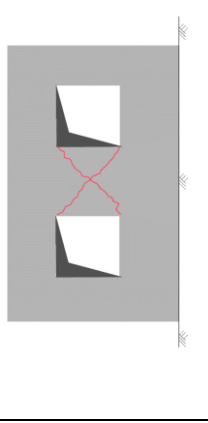
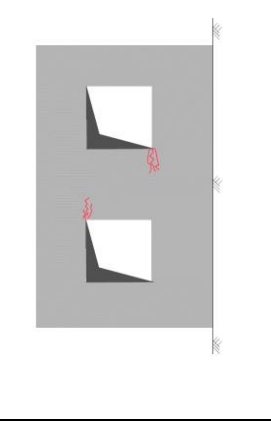
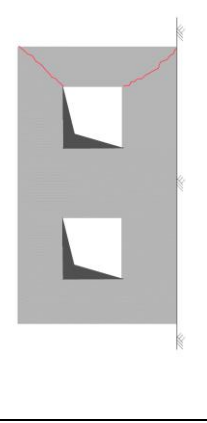
F44	4	Clay Brick	Moderate	Medium	0.67	1	Cracks started from corner of the openings and propagated towards adjacent opening corner.	Diagonal Tension	
F45	4	Clay Brick	Moderate	Medium	1.25	1	Cracks started from corner of the openings and propagated towards adjacent opening corner. Additionally, Flexural failure is observed at pier.	Hybrid Failure (Diagonal Tension + Flexural (Toe crushing))	
F46	4	Clay Brick	Low	Low	0.39	1	Cracks started from corner of the openings and propagated towards wall edge.	Diagonal Tension	

Table D.1 (continued)

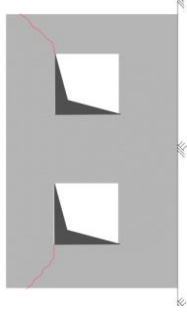
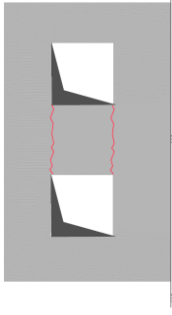
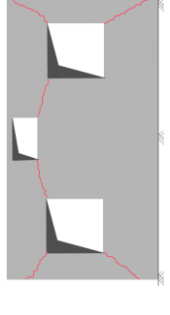
F47	4	Clay Brick	Low	Low	Low	0.54	1	Cracks started from corner of the openings and propagated towards wall edge.	Diagonal Tension	
F48	4	Adobe	Low	Low	Low	0.62	1	Cracks started from corner of the openings and propagated towards wall edge.	Diagonal Tension	
F48	4	Adobe	Low	Low	Low	0.80	2	Cracks started from corner of the openings and propagated towards adjacent opening corner.	Sliding Shear	
F49	5	Clay Brick	Low	Low	Low	1.20	1a	Cracks started from corner of the openings and propagated towards wall edge.	Diagonal Tension	

Table D.1 (continued)

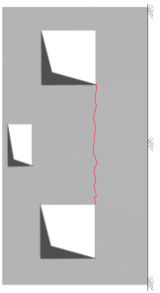
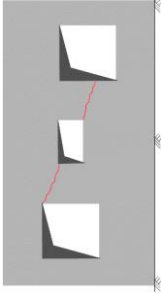
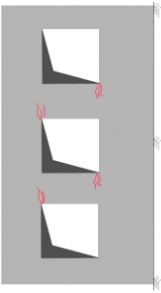
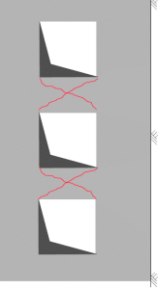
F49	5	Clay Brick	Low	Low	1.80	1b	Cracks started from corner of the openings and propagated towards adjacent opening corner.	Sliding Shear	
F50	5	Clay Brick	Moderate	Medium	0.80	1	Cracks started from corner of the openings and propagated towards adjacent opening corner.	Diagonal Tension	
F51	5	Clay Brick	Low	Low	2	1	Flexural failure is observed at pier.	Flexural (Toe crushing)	
F52	5	Stone	Low	Low	1.1	1	Cracks started from corner of the openings and propagated towards adjacent opening corner.	Diagonal Tension	

Table D.1 (continued)

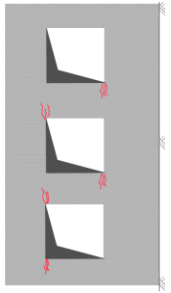
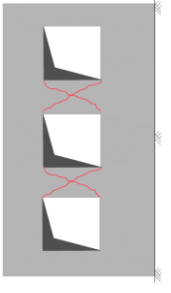
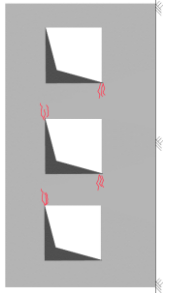
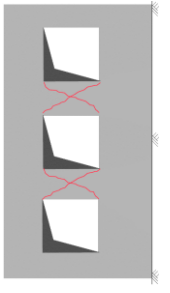
F53	5	Clay Brick	Low	Low	1.78	1	Flexural failure is observed at pier.	Flexural (Toe crushing)	
F53	5	Clay Brick	Low	Low	1.14	2	Cracks started from corner of the openings and propagated towards adjacent opening corner.	Diagonal Tension	
F53	5	Clay Brick	Low	Low	5.33	3	Severe flexural failure is observed at pier.	Flexural (Toe crushing)	
F54	5	Clay Brick	Moderate	Low	0.54	1	Cracks started from corner of the openings and propagated towards adjacent opening corner.	Diagonal Tension	

Table D.1 (continued)

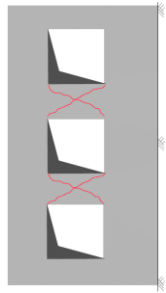
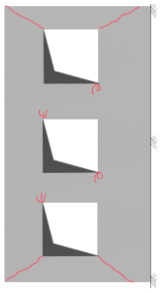
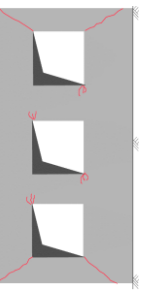
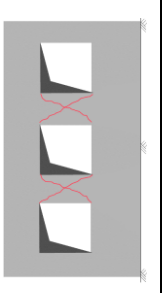
F54	5	Clay Brick	Moderate	Low	0.88	2	Cracks started from corner of the openings and propagated towards adjacent opening corner.	Diagonal Tension	
F55	5	Stone	Low	Low	1.25	1	Cracks started from corner of the openings and propagated towards wall edge.	Diagonal Tension	
F55	5	Stone	Low	Low	4.00	2	Flexural failure is observed at pier.	Flexural (Toe crushing)	
F56	5	Stone	Low	Low	1.33	1	Cracks started from corner of the openings and propagated towards adjacent opening corner.	Diagonal Tension	

Table D.1 (continued)

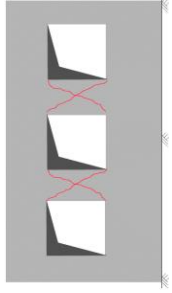
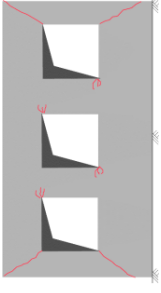
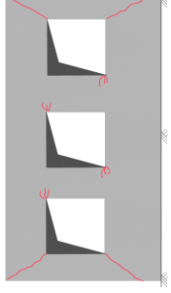
F57	5	Clay Brick	Moderate	Low	1.00	1	Cracks started from corner of the openings and propagated towards adjacent opening corner.	Diagonal Tension	
F57	5	Clay Brick	Moderate	Low	2.00	2	Flexural failure is observed at pier.	Flexural (Toe crushing)	
F58	5	Stone	Low	Low	1.00	1	Cracks started from corner of the openings and propagated towards adjacent opening corner.	Diagonal Tension	

Table D.1 (continued)

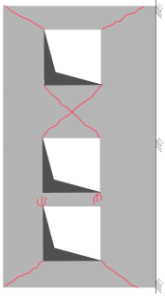
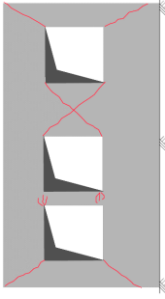
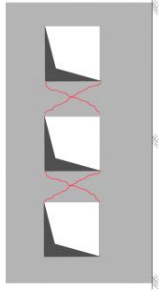
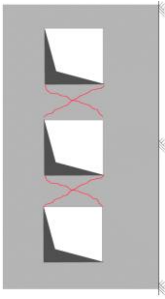
F59	5	Clay Brick	Low	Medium	3.00	1	Flexural failure is observed at pier.	Flexural (Toe crushing)	
F59	5	Clay Brick	Low	Medium	0.75	2	Cracks started from corner of the openings and propagated towards adjacent opening corner.	Diagonal Tension	
F60	5	Clay Brick	Low	Low	0.75	1	Cracks started from corner of the openings and propagated towards wall edge.	Diagonal Tension	
F60	5	Clay Brick	Low	Low	0.69	2	Cracks started from corner of the openings and propagated towards adjacent opening corner.	Diagonal Tension	

Table D.1 (continued)

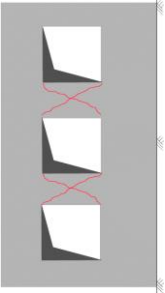
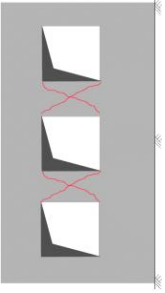
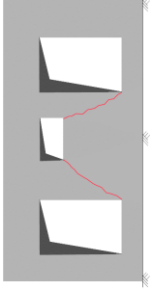
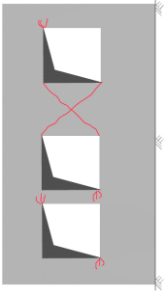
F60	5	Clay Brick	Low	Low	1.00	3	Cracks started from corner of the openings and propagated towards adjacent opening corner.	Diagonal Tension	
F60	5	Clay Brick	Low	Low	0.75	4	Cracks started from corner of the openings and propagated towards adjacent opening corner.	Diagonal Tension	
F61	5	Clay Brick	Moderate	Low	1.60	1	Cracks started from corner of the openings and propagated towards adjacent opening corner.	Diagonal Tension	
F62	5	Clay Brick	Low	Medium	2.00	1	Flexural failure is observed at pier.	Flexural (Toe crushing)	

Table D.1 (continued)

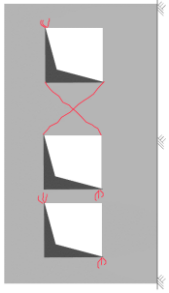
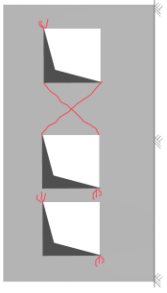
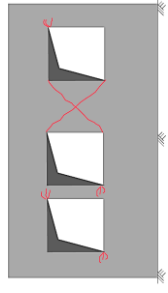
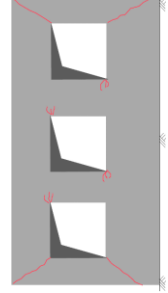
F62	5	Clay Brick	Low	Medium	1.00	2	More severe cracks started from corner of the openings and propagated towards adjacent opening corner.	Diagonal Tension	
F62	5	Clay Brick	Low	Low	1.20	3	Cracks started from corner of the openings and propagated towards adjacent opening corner.	Diagonal Tension	
F62	5	Clay Brick	Low	Low	1.00	4	Cracks started from corner of the openings and propagated towards adjacent opening corner.	Diagonal Tension	
F63	5	Clay Brick	Moderate	Medium	2.13	1	Flexural failure is observed at pier.	Flexural (Toe crushing)	

Table D.1 (continued)

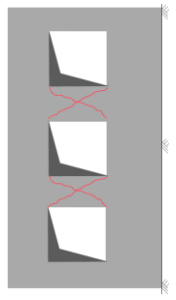
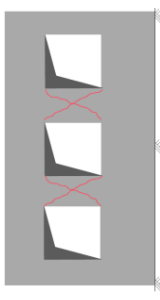
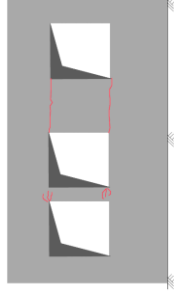
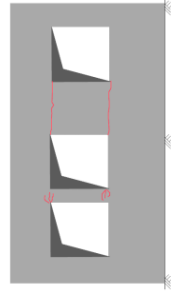
F64	5	Clay Brick	Moderate	High	0.89	1	More severe cracks started from corner of the openings and propagated towards adjacent opening corner.	Diagonal Tension	
F64	5	Clay Brick	Moderate	Medium	0.89	2	Cracks started from corner of the openings and propagated towards adjacent opening corner.	Diagonal Tension	
F64	5	Clay Brick	Moderate	Low	0.89	3	Sliding cracks started from corner of the openings and propagated towards adjacent opening corner.	Sliding Shear	
F64	5	Clay Brick	Moderate	Low	0.89	4	Sliding cracks started from corner of the openings and propagated towards adjacent opening corner.	Sliding Shear	

Table D.1 (continued)

F65	5	Clay Brick	Moderate	Medium	1.25	1	Sliding cracks started from corner of the openings and propagated towards adjacent opening corner.	Sliding Shear	
F65	5	Clay Brick	Low	Low	0.67	2	Cracks started from corner of the openings and propagated towards wall edge.	Diagonal Tension	
F66	5	Clay Brick	Low	Low	0.63	1	Cracks started from corner of the openings and propagated towards wall edge.	Diagonal Tension	
F67	5	Clay Brick	High	Low	0.36	1	Cracks started from corner of the openings and propagated towards wall edge.	Diagonal Tension	

Table D.1 (continued)

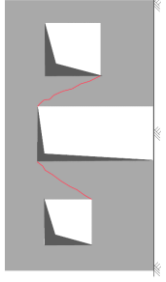
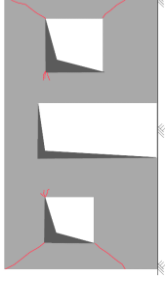
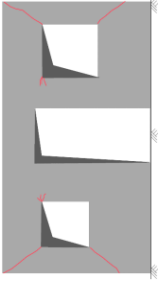
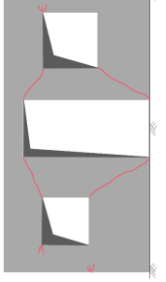
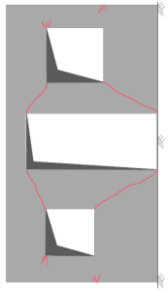
F67	6	Clay Brick	High	High	0.83	2	Cracks started from corner of the openings and propagated towards adjacent opening corner.	Diagonal Tension	
F68	6	Clay Brick	Low	Low	0.83	1	Cracks started from corner of the openings and propagated towards wall edge.	Diagonal Tension	
F68	6	Clay Brick	Low	Low	3.88	2	Flexural failure is observed at pier.	Flexural (Toe crushing)	
F69	6	Clay Brick	Low	Low	1.75	1	Flexural failure is observed at pier.	Flexural (Toe crushing)	

Table D.1 (continued)

F69	6	Clay Brick	Low	Low	1.17	2	Cracks started from corner of the openings propagated towards adjacent opening corner.	Diagonal Tension	
F70	6	Clay Brick	Low	High	1.3	1	Cracks started from corner of the openings and propagated towards adjacent opening corner.	Diagonal Tension	